UNIVERSITÉ DU QUÉBEC À MONTRÉAL

SIMULATIONS OF TROPICAL CYCLONES AND AFRICAN EASTERLY WAVES IN HIGH- AND LOW-RESOLUTION CLIMATE MODELS

THESIS

SUBMITTED IN PARTIAL FULFILLMENT OF THE REQUIREMENTS

FOR THE DEGREE OF

PH.D. IN ENVIRONMENTAL SCIENCES

BY

LOUIS-PHILIPPE CARON

APRIL 2011

UNIVERSITÉ DU QUÉBEC À MONTRÉAL

SIMULATION DES CYCLONES TROPICAUX ET DES ONDES D'EST AFRICAINES AVEC DES MODÈLES DE CLIMAT À HAUTE ET BASSE RÉSOLUTION

THÈSE

PRÉSENTÉE

COMME EXIGENCE PARTIELLE

DU DOCTORAT EN SCIENCES DE L'ENVIRONNEMENT

PAR

LOUIS-PHILIPPE CARON

AVRIL 2011

REMERCIEMENTS

First and foremost, I would like to thank my supervisor, Colin Jones, who agreed to take me under his wing, despite my complete ignorance of atmospheric sciences, let alone hurricanes, when I started at UQAM five years ago. Despite sometimes very difficult conditions and an extremely constraining schedule, he was never too busy to offer help, advice and guidance. This thesis is in great part due to his vast knowledge of climate sciences and his unique insights. His support throughout the years has contributed to making these last five years some of the best years of my life. I am forever indebted to him.

This thesis would also not have been possible without the invaluable help of Katja Winger, who showed me everything I know about the GEM model and RPN data and who always found the time to address my problems, regardless of how busy she was. The CRCMD network and all the UQAM graduate students are lucky to be able to count on such a resourceful individual.

I would also like to thank all the members of my supervising committee, Bernard Dugas, René Laprise and Gilbert Brunet, whose helpful advice and timely conversations have guided me and allowed me to finish this thesis in a reasonable amount of time.

As well, I would like to thank all the supporting staff who made my life here at UQAM so much easier. They are Nadjet, Abderrahim, Frédérik and Georges who kept the various computers I had to use under control, as well as Delphine, Adélina and Lucie Brodeur, who helped me navigate the giant maze of UQAM bureaucracy relatively unscathed.

I cannot forget to thank all the people with whom I've crossed paths here at

UQAM and Ouranos over the years. Danahé, my only companion during the lectures, Marko, JP, Alejandro, Philippe, Elena, Camille, Gwen, Mariane, Caroline, Guillaume, Marco, Marie-France, Dominique, Simon, Fred, Travis and Biner. A very special thank you to Patrick, with whom I developped a special friendship over the years and who was always willing to share his knowledge of the program and his passion for atmospheric science with me. You all contributed, in your own way, to making my time at UQAM and Ouranos most enjoyable. I hope we stay in touch.

Finally, but certainly not least, my warmest thank you to my family. First, to my wife, Katherine, who moved to Montreal to support me in this adventure and will now follow me to Europe. Not only are you always very understanding of my often chaotic and busy situation, but you put your proofreading skills at my disposal when I needed them. Thank you to my mother, Elizabeth, who was always there to help when times were more difficult, and to my sister and father who always support me, no matter what.

Thanks to you all.

TABLE DES MATIÈRES

LISTE DES FIGURES

LISTE DES TABLEAUX

LISTE DES ABRÉVIATIONS, SIGLES ET ACRONYMES

AEW	African Easterly Wave
AGCM	Atmospheric Global Climate Model
ASO	August-September-October
CGCM	Coupled Global Climate Model
CPW	Central Pacific Warming
CSGP	Convective Seasonal Genesis Parameter
CYGP	Convective Yearly Genesis Parameter
ECMWF	European Centre for Medium-Range Weather Forecasts
ENSO	El Niño Southern Oscillation
EPC	Eastern Pacific Cooling
EPW	Eastern Pacific Warming
ERA-40	ECMWF 40-year re-analysis data
GCM	Global Climate Model
GEM	Global Environmental Multiscale model
GHG	Greenhouse Gas
GIEC	Groupe d'experts Intergouvernemental sur l'Évolution du Climat
GPCP	Global Precipitation Climatology Project
GPI	Genesis Potential Index
GVAR	Global, VAriable Resolution
HURDAT	HURricane DATabase
IPCC	Intergovernmental Panel on Climate Change
IWV	Integrated Water Vapor
JAS	July-August-September
JASO	July-August-September-October
JFM	January-February-March
JJASON	June-July-August-September-October-November
JTWC	Joint Typhoon Warning Center
LAM	Limited Area Model
LBC	Lateral Boundary Condition
MCG	Modèle de Circulation Générale
MDR	Main Development Region
MJO	Madden - Julian Oscillation
MPI	Maximum Potential Intensity
MRC	Modèle Régional de Climat
MRCC	Modèle Régional de Climat Canadien
MSLP	Mean Sea Level Pressure
NH	Northern Hemisphere

NHC	National Hurricane Center
PDI	Power Dissipation Index
RCM	Regional Climate Model
SGP	Seasonal Genesis Parameter
SH	Southern Hemisphere
SOI	Southern Oscillation Index
SST	Sea Surface Temperature
TC	Tropical Cyclones
TCLV	Tropical Cyclone-Like Vortex
YGP	Yearly Genesis Parameter

RÉSUMÉ

Cette thèse se penche sur différents aspects des cyclones tropicaux tels que simulés par des modèles de circulation générale (MCG) et un modèle régional de climat (MRC), le modèle régional de climat canadien (MRCC5). D'abord, nous évaluons la capacité d'un ensemble de MCG, utilisé dans le cadre du 4e rapport du GIEC (Groupe d'experts Intergouvernemental sur l'Évolution du Climat), à capturer les principales zones de cyclogénèse au travers d'indices dérivés à partir des champs atmosphériques favorables à la formation des cyclones tropicaux. En comparant les événements de cyclogénèse observés avec les deux indices calculés à partir de réanalyses et d'un ensemble de MCG, nous vérifions que les indices arrivent à relativement bien représenter la distribution actuelle des cyclones tropicaux, autant dans les modèles que les réanalyses. En comparant des simulations couvrant la période 2080-2100 avec la période présente, l'indice jugé plus stable projette une légère augmentation du nombres des tempêtes dans le Pacifique Ouest.

Le deuxième partie de la thèse est consacrée à évaluer la capacité du MRCC5 à reproduire la climatologie des cyclones tropicaux observée durant la période 1979-2006. Plus précisément, nous évaluons l'impact d'une augmentation de la résolution sur les caractéristiques physiques des cyclones ainsi que sur leur distribution géographique, de même que l'impact des conditions aux frontières, de la technique de « downscaling » dynamique utilisée et de la taille du domaine sur les cyclones simulés. Une telle évaluation est une étape cruciale à toute étude d'impact des changements climatiques sur les ouragans. La distribution des cyclones est consistante avec la distribution d'un indice de cyclogénèse, ce qui permet de mieux comprendre les changements observés dans les différentes simulations. Aussi, nous évaluons la capacité du modèle à reproduire la variabilité interannuelle observée durant cette période, et plus particulièrement l'impact de l'oscillation australe d'El Niño (El Niño Southern Oscillation ou ENSO) sur la cyclogénèse. Finalement, nous étudions les ondes d'Est africaines, systèmes précurseurs des ouragans dans l'Atlantique, tel que simulées par le MRCC5 de même que leur relation avec les cyclones tropicaux de l'Atlantique. Règle générale, le MRCC5 arrive à reproduire de façon réaliste l'activité observée durant la période 1979-2006.

Mots-clés :
cyclones tropicaux, indices de cyclogénèse, ondes d'Est africaines, modèle régional de climat, modèle de circulation générale

ABSTRACT

This thesis evaluates different aspects of tropical cyclones as simulated by Global Climate Models (GCMs) and the Canadian Regional Climate Model (CRCM). First, we investigate the ability of a GCM ensemble to capture the main areas of cyclogenesis through cyclogenesis indices derived from large-scale fields known to impact tropical cyclone formation. By comparing observed cyclogenesis events with the two indices calculated from reanalysis and the ensemble mean, we show that the indices capture current tropical cyclone distribution relatively well, both in reanalysis and in the GCM ensemble. By further comparing the current period with the 2080-2100 period simulated by the GCMs, the index deemed the most robust for application to climate change shows a slight increase in the number of storms in the West Pacific.

The second part of the thesis evaluates the ability of the CRCM to simulate observed Atlantic tropical cyclone activity during the 1979-2006 period. More precisely, we evaluate the impact of increasing resolution on tropical cyclone physical characteristics as well as their geographical distribution. We also investigate the impact of lateral boundary conditions, the downscaling technique and the size of the domain on simulated tropical cyclones. Such an evaluation is a crucial step in evaluating the potential impact of climate change on hurricane activity. The geographical distribution of simulated tropical cyclones is consistent with the distribution of a genesis index, which helps understanding the observed changes in the various simulations. Furthermore, we evaluate the ability of the model at capturing the observed interannual variability over the given period as well as the impact of the El Niño Southern Oscillation (ENSO) on Atlantic cyclogenesis. Finally, we investigate African easterly waves, which are precursor systems to many of the strongest storms in the Atlantic, as simulated by the CRCM, as well as their relationship to simulated tropical cyclones. Overall, the CRCM does a relatively good job of capturing the observed activity over the 1979-2006 period.

Key words :
tropical cyclones, cyclogenesis index, african easterly waves, regional climate model, global climate model

INTRODUCTION

Contexte

Les cyclones tropicaux, aussi appelés ouragans, typhons ou tempêtes cycloniques selon le bassin où ils se forment, sont les phénomènes naturels les plus dévastateurs, tant sur le plan économique qu'humain (Landsea, 2000). La destruction causée par l'ouragan Katrina, qui a touché la Nouvelle-Orléans en 2005, frappe l'imagination : plus de 125$ milliards ($ de 2005 ; Munich Re., 2006) de dommage, surpassant facilement le précédent record établi par Andrew en 1992 de 26$ milliards (Blake, 2005).

Cependant, les pertes de vie associées à ces deux tempêtes demeurent relativement modestes si on les compare avec des tempêtes ayant frappé des populations plus démunies qui tendent à être mal préparées pour ce genre de catastrophes. Par exemple, des cyclones ayant touché terre au Bangladesh en 1970 et 1991 ont fait 300,000 et 138,000 morts respectivement (Holland, 1993 ; Wilson, 1994). Plus récemment, le cyclone Nargis, au printemps 2008, a frappé le Myanmar et aurait fait, selon les estimés les plus conservateurs, au-delà de 130,000 morts (Webster, 2008).

Les cyclones tropicaux se forment seulement au-dessus des océans dont la température de surface dépasse les $26.5°C$. Les océans dont la température à la surface est supérieure à $26.5°C$ peuvent soutenir la convection profonde, mécanisme par lequel la vapeur d'eau en surface est transportée jusqu'au sommet de la troposphère où elle se condense et libère la chaleur latente nécessaire au maintien et à l'intensification du cyclone. Une augmentation des températures des océans, liée à une augmentation des gaz à effet de serre (GES) dans l'atmosphère, est prévue pour les décennies à venir et risque d'avoir un impact sur le développement de ces tempêtes. Par contre, la nature exacte des changements est difficile à prédire puisque les cyclones dépendent de plusieurs autres facteurs pour leur formation et intensification, facteurs dont on ignore encore comment ils seront affectés avec une augmentation des GES. Déjà dans l'Atlantique, le bassin pour lequel les observations sont les plus fiables, on détecte une augmentation de l'intensité des cy-

clones les plus violents (Elsner et al., 2008), de même qu'une augmentation de la durée de la saison des ouragans (Kossin, 2008).

Les modèles atmosphériques arrivant à bien reproduire le climat observé, il est naturel de vouloir les utiliser pour étudier l'impact du réchauffement climatique sur les cyclones. Par contre, de par leur faible résolution, les modèles de circulation générale (MCG) ont de la difficulté à produire des cyclones que l'on pourrait qualifier de réalistes, produisant plutôt des systèmes qui, s'ils partagent quelques caractéristiques physiques avec les cyclones, sont néanmoins trop étendus et trop faibles. En fait, les MCG ayant une résolution de 100 km et plus grossière ne produisent pas de cyclones tropicaux au sens strict du terme. Cependant, certaines techniques ont été développées pour contourner cet obstacle. La première étude de cette thèse aborde d'ailleurs cette question. Par contre, les modèles régionaux de climat (MRC), avec une résolution de quelques dizaines de km, arrivent à représenter les cyclones tropicaux de façon beaucoup plus réaliste et parviennent même à reproduire la variabilité observée au cours des dernières décennies dans l'Atlantique (Knutson et al., 2007). Dans la deuxième partie de cette étude, nous tenterons donc d'évaluer dans quelle mesure le modèle régional de climat canadien (MRCC5) arrive à reproduire la climatologie observée au cours des dernières décennies dans l'Atlantique en termes de cyclones tropicaux, de même que l'impact de la configuration choisie sur cette capacité. Cette validation est une première étape essentielle qui permettra d'évaluer dans quelle mesure le MRCC5 est adéquat pour effectuer des projections climatiques d'ouragans dans l'Atlantique.

Présentation des différentes sections de la thèse

Le corps de cette thèse est composé de trois chapitres, chacun représentant un article publié ou soumis pour publication dans un journal scientifique. Le premier chapitre, intitulé « Analysing present, past and future tropical cyclone activity as inferred from an ensemble of coupled global climate models » et publié dans Tellus en 2008 est une analyse des conditions favorables à la cyclogénèse dans un ensemble de modèles de circulation générale sur une période de deux cents ans. Comme mentionné ci-haut, les MCG, avec à leur relativement faible résolution ($100 - 200$ km), ont de la difficulté à produire des cyclones tropicaux. En fait, ils produisent des systèmes semblables aux cyclones tropicaux dans les régions où ceux-ci sont généralement observés, mais ces systèmes tendent à être beaucoup plus vastes que les cyclones observés et aussi de beaucoup plus faible

intensité. La plupart des études faites à l'aide de GCM sur ces tempêtes doivent réduire la limite théorique à partir de laquelle un système dépressionnaire peut être qualifié de tempête tropicale (ou tempête cyclonique ou cyclone tropical, dépendamment de la région), faute de quoi aucune tempête n'est détectée. Cependant, même en variant cette limite, plusieurs MCG n'arrivent pas à produire une activité semblable à celle observée.

Les indices de cyclogénèse offrent une alternative par laquelle on peut étudier les cyclones tropicaux dans les MCG. Dérivés à partir des champs atmosphériques qui ont un impact sur la formation des cyclones, ceux-ci offrent une relation statistique entre ces mêmes champs et le nombre de cyclones tropicaux observés. Cette technique permet d'évaluer la capacité d'un modèle à reproduire correctement les zones les plus propices à la cyclogénèse et d'induire le nombre de tempêtes qui *pourraient* se former dans un bassin donné si la résolution du modèle le lui permettait. De même, en admettant que les conditions propices à la formation des cyclones demeurent constantes dans le temps, ces indices offrent une alternative par laquelle étudier les changements d'activité simulés par les MCG sur des périodes de plusieurs dizaines, voire plusieurs centaines d'années.

Ce premier article utilise donc cette approche pour évaluer la capacité d'un ensemble de simulations de MCG, préparées dans le cadre du 4e rapport du GIEC, à reproduire la cyclogénèse observée au cours du XXe siècle. Pour ce faire, deux indices différents sont utilisés et les résultats sont comparés aux observations, de même qu'aux indices de cyclogénèse obtenus, lorsque la méthode est appliquée à des données de réanalyse, dans ce cas, ERA40. Une modification à l'un des indices est suggérée afin de réduire la sensibilité de celui-ci à l'un des paramètres. Finalement, cet article évalue la projection faite par cet ensemble pour la période du XXIe siècle.

Le deuxième article, intitulé « Impact of resolution and downscaling technique in simulating recent Atlantic tropical cyclone activity » a été publié dans *Climate Dynamics* en 2010. En utilisant le modèle régional de climat canadien (MRCC5), nous évaluons l'impact d'une augmentation de la résolution d'un modèle, d'une résolution typique des MCG utilisés dans l'article précédent, soit 1° et 2°, à une plus haute résolution typique des modèles régionaux, i.e. 0.3°. Cette étude se penche sur l'impact du changement de résolution sur les champs atmosphériques favorables au développement des cyclones tropicaux, à l'aide d'un indice de cyclogénèse, ainsi que sur les cyclones tropicaux eux-mêmes.

Pour ce faire, un programme a été développé en FORTRAN qui permet de naviguer les sorties de modèles du MRCC5 et de détecter les cyclones tropicaux lorsque certaines conditions, typiques de ces tempêtes, sont satisfaites.

Ensuite, on met à profit la flexibilité du MRCC5 pour comparer l'impact de deux techniques différentes de downscaling dynamique, soit en mode global à résolution variable, et en mode à aire limitée à résolution fixe. Dans le deuxième cas, on étudie aussi l'impact des conditions aux frontières (MCG vs réanalyses) sur les cyclones tropicaux. Pour ce faire, on y évalue la capacité du modèle à reproduire la distribution géographique des cyclones, leur intensité, variabilité intra-saisonnière et inter-annuelle, de même que l'impact d'ENSO sur ceux-ci.

Finalement, le troisième article, intitulé « Understanding and simulating the link between African Easterly Waves and Atlantic Tropical Cyclones using a Regional Climate Model : The role of domain size and lateral boundary conditions. », poursuit dans la lignée du précédent et s'intéresse au lien qui existe entre les ondes d'Est africaines et les cyclones tropicaux de l'Atlantique tel que simulés par le MRCC5. La majorité des ouragans de forte intensité (catégories 3-5) qui se forment dans l'Atlantique proviennent d'ondes d'Est africaines (Landsea, 1993). Ces ondes se propagent d'Est en Ouest au-dessus de la région du Sahel entre les mois de mai et novembre et plusieurs d'entre elles, au contact des eaux chaudes de l'Atlantique, s'intensifient pour former les tempêtes tropicales et ouragans que l'on observe durant l'été boréal au-dessus de l'Atlantique. Dans cet article, nous nous intéressons donc à l'impact de simuler à haute résolution le climat en amont des cyclones, soit la partie Nord de l'Afrique, sur ceux-ci.

Pour ce faire, nous utilisons différentes conditions aux frontières sur un domaine couvrant d'abord seulement l'Atlantique. Les différentes conditions aux frontières proviennent de réanalyses et de simulations de MCG effectuées à différentes résolutions. Nous comparons ensuite avec des simulations faites avec les mêmes conditions frontières et des domaines où 1) la frontière Est du domaine est repoussée au méridien de Greenwhich et 2) la frontière Est du domaine est placée complètement à l'est de l'Afrique. Nous évaluons l'impact de ces différentes configurations sur les statistiques annuelles des cyclones produits, leur distribution géographique et tentons de cerner le rôle des ondes d'Est africaines dans ces différentes simulations.

Coût informatique

Quelques mots sur les ressources informatiques qui ont été nécessaires pour produire cette étude. Au total, 17 simulations de 28 ans (donc 476 saisons d'ouragans), à différentes résolutions et de configurations différentes, ont été réalisées. Cela représente plus de 15 Toctets de données. Cela s'est avéré nécessaire pour plusieurs raisons :

1. relativement peu de cyclones se forment dans une saison donnée.
2. les cyclones étant des phénomènes stochastiques, une étude d'ensemble est préférable à une seule simulation. Cela est particulièrement vrai lors de l'analyse de la variabilité interannuelle et de l'impact d'ENSO sur les cyclones.
3. l'étude de l'impact des conditions aux frontières et de la zone couverte par la grille nous forcent à répéter les 28 ans de simulation en changeant seulement un paramètre (pilote, format de la grille, ...)

Dans certains cas, il aurait été souhaitable d'augmenter à plus d'une simulation les 28 années simulées dans une certaine configuration et, dans d'autres cas, d'augmenter davantage la taille de l'ensemble. Par contre, des ressources informatiques limitées nous ont forcé à faire des choix et cette étude a été faite à l'intérieur de ces contraintes.

CHAPITRE I

ANALYSING PRESENT, PAST AND FUTURE TROPICAL CYCLONE ACTIVITY AS INFERRED FROM AN ENSEMBLE OF COUPLED GLOBAL CLIMATE MODELS

Abstract

Using the Yearly Genesis Parameter (YGP) and the Convective-YGP (CYGP), the main large-scale climatic fields controlling tropical cyclone formation are analysed and used to infer the number of tropical cyclones in a given basin using ERA40 reanalyses for the period 1983-2002. Both indices show a reasonable global number and spatial distribution of implied tropical cyclones compared to observations.

Using the same approach, we evaluate tropical cyclone activity in the last 20 year period of the 20th century in an ensemble of nine Coupled Global Climate Model simulations submitted to the IPCC AR4. We extend this analysis backwards in time, through the 20th century, and find the ensemble derived CYGP suggests no trend in inferred TC numbers while the YGP, after applying a correction to compensate for its oversensitivity to sea surface temperature, suggests a small upward trend. Both indices give a fair geographical distribution of cyclogenesis. Finally, we assess future tropical cyclone trends using 3 emission scenarios. Using the CYGP, which appears the most robust index for application to climate change, a small increase is predicted in the North-Western Pacific in the A1B and A2 scenarios.

1.1 Introduction

The active 2005 hurricane season likely contributed to the growing awareness of the general population and policy makers towards climate change and its possible conse-

quences. Ironically, no consensus exists within the scientific community regarding the variety of possible changes in tropical cyclone (TC) activity (e.g. length of TC season, geographical distribution of TCs, maximum TC intensity, etc) that might ensue in response to increasing levels of CO_2. The fourth assessment report of the IPCC (Meehl et al., 2007) suggests an increase in mean wind and precipitation intensity of TCs, but whether or not this trend can already be observed, as claimed by Emanuel (2005) and Webster et al. (2005), or if this apparent trend is just a result of decreasing quality of the observed data sets as one goes backwards in time (Klotzbach, 2006) or to varying measurement techniques (Wu et al., 2006) remains an open question. However, when it comes to tropical cyclone frequency, no particular consensus has yet emerged from the various model simulations and whether or not the global frequency of TCs will remain at current levels, increase or decrease in the future remains highly uncertain.

Two techniques have commonly been used to diagnose the number of tropical cyclones in Global Climate Models (GCMs). The first technique consists of locating and tracking what have been coined tropical cyclone-like vortices (TCLVs) (Walsh and Watterson, 1997). GCM resolutions are too coarse to resolve real TCs and instead reproduce systems reminiscent of TCs (known as TCLVs), but with some distinct characteristics. Specifically, simulated TCLVs do not reproduce important features of the tropical cyclone, such as the eye structure. Many studies, using both Global and Regional Climate Models, have relied on this technique to estimate future TC activity by comparing the simulated number, intensity and paths of TCLVs in current and future climate conditions, often with contradictory results (Haarsma et al., 1993; Bengtsson et al., 1996; Sugi et al., 2002; McDonald et al., 2005; Chauvin et al., 2006; Oouchi et al., 2006; Bengtsson et al., 2007b). Latest results using this technique seem to point towards an overall reduction in the number of cyclones, but an increase in the number of intense storms. However, these simulations rely on systems that are reminiscent of TCs but not necessarily representative of them : the structure of the TCLVs cannot be considered genuinely close to reality. The 17 ms^{-1} threshold limit normally used to define the existence of a TC has to be lowered in these simulations in order to detect an adequate number of TCLVs. It then becomes somewhat arbitrary to fix a wind speed criterion for detection of a "TC".[1] Hence, while studies based on this technique might be suggestive of a likely response of TCLVs to increases in GHGs, they are likely to remain not

1. For additional infomations on the arbitrariness of TC detection in CGCMs, see a recent article by Walsh et al. (2007).

entirely convincing until the models used adequately reproduce systems more closely reminiscent of observed TCs.

The second technique used to estimate future TC frequency provides an estimate of tropical storm activity through the use of a genesis parameter, dependent on seasonal mean large-scale fields which are known to play a role in controlling TC genesis (Gray, 1975). Developed empirically, these indices allow a quantification of the influence of large-scale fields on TC activity and reproduce with some accuracy the observed number, seasonal and geographical distribution of TCs for the present climate. This method may be better suited to TC analysis in low-resolution GCMs that might be expected to simulate, with some level of accuracy, the large-scale climate controls on TC activity rather than the TCs themselves. This contention rests on the premises that there exists a deterministic large-scale control on TC activity which remains valid in future climate conditions and, furthermore, that CGCMs accurately simulate both the present-day large-scale tropical climate and future changes in key large-scale quantities in response to increasing levels of GHGs. One major drawback of this approach is that it can only give an estimate of TC numbers and cannot address the issue of changes in TC intensity.

To the authors knowledge, Ryan et al. (1992) were the first to use a genesis index with climate model output to estimate future TC activity in a greenhouse gas enhanced atmosphere. They used the genesis index developed by Gray (1975), the Seasonal Genesis Parameter (SGP) and, through comparing the SGP for simulated present and future climate conditions, derived a large increase in implied TC numbers in both hemispheres. This they deemed to be an overestimate of the probable real future TC trend due to the oversensitivity of the index to ocean surface temperature. This conclusion was shared by Royer et al. (1998) when they applied a similar analysis to a different climate model, which led to the development of a new index, the Convective SGP (CSGP), which retains some of the parameters of the SGP but replaces the ones considered to be unreliable in future climate conditions (the difference between these two indices is discussed in section 1.2). Using this new index, Royer et al. predicted a decrease in the number of TCs in the Southern Hemisphere and a small increase in the Northern Hemisphere, the largest increase being located in the Western-North Pacific (WN Pac). McDonald et al. (2005), using the same index found a more complex pattern of changes, including a region of decreasing activity in the WN Pac. They also found that the pattern of change given by the CYGP was similar to the pattern found by tracking individual

TCs. This last conclusion was shared by Chauvin et al. (2006), when comparing possible TC activity changes over the Northern Atlantic. All of these studies relied on one single coupled GCM (CGCM) or a single atmospheric GCM run with prescribed ocean surface temperatures for present and future climate conditions. Recently, Camargo et al. (2007) analysed the predictive skill of another index, the Genesis Potential Index (GPI), developed by Emanuel and Nolan (2004), for current climate conditions using 5 atmospheric GCMs forced by observed SSTs. The relationship between the GPI and the number of TCs was found to be model and resolution dependent.

In this study, we attempt to estimate the possible change in the number of TCs in future climates by comparing the CSGP and the SGP, to which we have applied a first-order correction, in an ensemble of model simulations prepared for the IPCC fourth assesment report (AR4) and originating from the World Climate Research Programme's (WCRP's) Coupled Model Intercomparison Project, phase 3 (CMIP3). In section 2, we describe both indices, while in section 3 we evaluate these indices by using the ECMWF 40 year reanalysis data (ERA40, Uppala et al., 2005) and comparing the implied number of TCs from the ERA40 SGP and CSGP with the number of observed cyclones for the same period (1983-2002). We also discuss the dangers inherent in using reanalysis data in attempting to detect a trend in the evolution of these indices and implied trends in TC occurence. In section 4, we introduce the models used in this study and compare the simulated present-day SGP and CSGP for the CGCM ensemble to the reanalysis data and observed TC occurences over a similar period. We then look at the CGCM simulated time evolution of the SGP and CSGP for the period 1861-2000 and discuss a possible correction to the SGP. Finally, in section 5, we compare the indices and implied TC numbers for future climate conditions under 3 different CO_2 equivalent emission scenarios.

1.2 Methodology

The SGP is the product of a dynamical potential and a thermal potential, each of which rely on three parameters. Together, these six components summarize the main large-scale dynamical and thermodynamic variables believed to control TC activity on seasonal timescales.

$$\mathrm{SGP} = \underbrace{(|f| \times I_\zeta \times I_{WS})}_{\text{Dynamic potential}} \times \underbrace{(E \times I_\theta \times I_{RH})}_{\text{Thermal potential}}$$

where the dynamical potential is defined such that

- $f = 2\Omega \sin \phi$ is the Coriolis parameter at a given latitude (ϕ is the latitude and Ω the angular velocity of the Earth) in $10^{-5}\ s^{-1}$.
- $I_\zeta = \zeta \frac{f}{|f|} + 5$ with ζ being the relative vorticity at 925 hPa in $10^{-6}\ s^{-1}$ and $|\ |$ denotes an absolute value.
- $I_{WS} = \left(\left|\frac{\delta V}{\delta P}\right| + 3\right)^{-1}$ is the inverse of the vertical shear of the horizontal wind (V) between pressure (P) levels 950 hPa and 200 hPa, in $m\ s^{-1}/750\ hPa$.[2]

The thermal potential is defined as

- $E = \int_0^{60} \rho_w c_w (T - 26)\ dz$ measures the thermal energy of the ocean between the surface and 60 m depth (ρ_w and c_w are the density and specific heat capacity of sea water), in $10^3\ cal\ cm^{-2}$.[3]
- $I_\theta = \left(\frac{\delta \theta_e}{\delta P} + 5\right)$ is the moist static stability defined as the vertical gradient of the equivalent potential temperature θ_e between the surface and 500 hPa, in $K/500\ hPa$.
- $I_{RH} = Max\left(\frac{RH-40}{30}, 1\right)$, where RH is the average relative humidity in percent between 500 hPa and 700 hPa (i.e. a measure of the mid-tropospheric humidity).

If any of the components of the SGP is less than or equal to zero, the SGP is set to zero. The SGP is usually divided between the boreal winter (JFM), spring (AMJ), summer (JAS) and fall (OND) and is found to be a good predictor of the number of cyclones formed in a $5° \times 5°$ latitude-longitude grid for a given 20-year period. The Yearly Genesis Parameter (YGP) is calculated as the sum of the four SGPs and can be used to derive the annual average number of TCs over the same $5° \times 5°$ box for a given 20-year period.

In its original form, Gray (1975) set the threshold for deep convection at $26°C$. However, we will here use a threshold of $26.3°C$ when evaluating the SGP/YGP in current climate conditions. This is done to address a recurrent criticism of the YGP which is its reliance on the constant value of $26°C$ as the threshold for TC formation. It is argued that with increasing temperatures in the tropics, the vertical lapse rate will adjust such

---

2. Due to data availability, we use the 925 hPa level instead of the original 950 hPa for both the vorticity and the wind shear.

3. Because only the SSTs were available for the reanalysis and for some CGCMs simulations, it was assumed that the ocean temperature to depth 60 m was that of the surface temperature. Royer et al. (1998) estimated that this led to an overestimation of the thermal content of the Atlantic by up to 50% and in the Indian and Pacific Ocean by up to 20-30%.

that the warmer atmosphere will experience a shift in atmospheric stability, resulting in an increase in the threshold SST required to support deep convection. To a first order, one might expect the threshold SST for TC development to follow the mean surface warming over the tropical ocean. This implicitly assumes convection acts to maintain a relatively constant vertical lapse rate as the surface warms. Here, we attempt a type of first order correction based on this hypothesis by increasing Gray's original threshold.

Warming trends in the ocean vary greatly between individual basins, as shown by Casey and Cornillon (2001), but choosing different temperature changes for different regions of the globe would be impractical here. Instead, based on Bindoff et al. (2007), we use a mean linear trend of $0.1°C/decade$ for all the tropics, resulting in an increase of $0.3°C$ between the period used in Gray's original work when the YGP was developed (1952-1971) and current conditions (1983-2002 for ERA40 and 1981-2000 for CGCMs). Based on our earlier discussion regarding the atmospheric lapse rate adjustment to SST changes, this leads to an increase in the SST threshold in the YGP from $26°C$ to $26.3°C$. This new value of $26.3°C$ will be used as the new threshold for current climate conditions and will serve as a reference when defining past and future thresholds which will be adjusted around this reference value based on specific (model and observed) SST trends. Henceforth, this tropical SST dependent YGP will be referred to as the *adjusted YGP*.

By comparison, the Convective SGP (CSGP) replaces the thermal potential of the SGP by a convective potential defined as

$$\text{convective potential} = k \times P_c \tag{1.1}$$

where P_C is the seasonal mean convective precipitation, in mm/day computed by a given model. As opposed to Royer et al. (1998), we do not apply an a priori threshold criteria for the convective precipitation. However, if the number of TCs predicted is less than 0.5 per 20 year period, we set the CSGP to 0. The convective potential is also set to 0 over land regions. The CSGPs can also be summed over all seasons to give a CYGP. This index was developed with the goal of predicting future tropical cyclone activity, hence the proportionality constant is determined empirically such that the total, global number of tropical cyclones predicted by the CYGP for a given (present-day) period be the same as that from the YGP. The advantage of this index lies in the fact that the

convective precipitation integrates in an internally consistent manner, with respect to each model, the vertical atmospheric response to changes in SST, atmospheric stability and humidity whereas the SGP does not. It is worth mentionning that two recent studies (McDonald et al., 2005 and Chauvin et al., 2006) have found good agreements between the actual TC activity generated by their GCM and this index. Also, it should be emphasized that this potential is best suited for low-resolution GCMs, since convective precipitation is a model artifact resulting from coarse model resolution and the need to parameterize convection and therefore separately simulate convective and large-scale precipitation. Any significant increase in resolution should ideally see a gradual transfer of simulated convective precipitation into the large-scale component. This technique we believe is applicable to the resolution of present day (IPCC AR4) CGCMs and is likely to remain so until GCMs are running at resolutions significantly better than $\sim 1°$.

We aim to evaluate both indices by comparing the implied number of TCs from each index using ERA40 simulated values for the 20 year period 1983 to 2002. In doing this, we are implicitly assuming that the global reanalysis accurately represents the components of the SGP and CSGP at the $5° \times 5°$ scale. We then compare CGCM simulated TC values for the 20 year period 1981 to 2000 to the observed number of TCs and those derived from the reanalysis. 1983-2002 represents the last 20 year period of data available from the ERA40 reanalysis and was deemed the most accurate with respect to the assimilation of satellite data over the tropical oceans. The 1981-2000 period in the model simulations corresponds to the last 20 year period of the "Climate of the 20th Century" scenario. We deemed these two periods to be sufficiently similar to each be classed as present climate conditions.

Observations were taken from the Joint Typhoon Warning Center (JTWC) best track data set for the Southern Hemisphere, Western North Pacific and Northern Indian Ocean and from the National Hurricane Center (NHC) best track data set for the Northern Atlantic and North-East Pacific (NE Pac) (figure 1.1 shows the different basins). A storm was considered a TC at the location and the time for which the surface sustained winds were first measured to be higher or equal to 17 m/s. Each TC was considered only once, even if it lost its tropical storm status for a short period and regained it later. The exceptions to this rule are the few TCs originating from the Atlantic which weaken to a depression over North/Central America only to revert to TC status once they reach the warm waters of the North-Eastern Pacific.

1.3 Evaluation of the YGP and CYGP using ERA40 Reanalyses

Figure 1.2b and 1.2c compare the YGP and CYGP implied TC activity derived from the ERA40 reanalysis data, to observed numbers for the period 1983-2002 (figure 1.2a). This is done to give an indication of the implied TC numbers we might expect from the YGP and CYGP using the best available large-scale meteorological data. Depending on the quality of the reanalysed large-scale tropical meteorology, this exercise can be considered a partial evaluation of the skill of the YGP and CYGP indices to infer TC statistics. As summarized in table 1.1, the observed global mean number of TCs per year during the 1983-2002 period is 86.1 with an annual standard deviation over the 20 year period of 7.3 cyclones. The ERA40 YGP predicts an average of 75 TCs/year for the same period. Most regions of cyclogenesis are well reproduced by the ERA40 YGP, even if there appears to be an overall overestimate in the Southern Hemisphere (SH) and an underestimate in the Northern Hemisphere (NH). This shift in TC formation from the NH to the SH originates mostly from an underestimate of TC activity in the NE Pac and the Northern Atlantic and an overestimate in the South-West Pacific (SW Pac), as can be seen from table 1.2, which details the observed and analysis derived TC statistics by basin for the 1983-2002 period. There is also unusual activity in the Red Sea and in both Hemispheres TC formation is predicted slightly closer to the Equator than currently observed. It is interesting to note that these results show some striking similarities with that of Bengtsson et al. (2007a) who have tracked individual cyclones in ERA40 reanalysis in the Northern Hemisphere.

In the original study by Gray (1975) discrepancies between observations and YGP predictions were not as pronounced as they are with ERA40 : no TCs were predicted in the Red Sea or on the Equator and TCs in the NE Pac and NW Pac were closer to what was observed. Lowering the SST threshold in the YGP back to the original value used by Gray (1975), i.e. $26°C$, in the evaluation of the YGP with ERA40 increases the mean annual frequency of TCs to 83, closer to current observations, but does not improve the geographical distribution : if the activity in the NW Pac region now approaches current level, the SW Pac region now overestimates TC activity and the NE Pac still does not capture the high density cyclogenesis present in that basin (not shown). Whether these differences between Gray's (1975) original predictions and ERA40's are due to deficiences in the reanalysis data compared to the observational data used by Gray we are unable to evaluate at this time.

For the CYGP, we calculate the constant k of the convective parameter so that the total number of cyclones for the 1983-2002 period is the same for both methods, i.e 75 TCs/year. This leads to a value of $k = 0.1379$, which lies between the respective values found using GCM derived YGP and convective precipitation by Royer et al. (1998) and McDonald et al. (2005), namely 0.145 and 0.1159.

This index gives a distribution comparable to the YGP, but we see a shift in activity between the different basins : TC activity is reduced in the NW Pac and around Northern Australia but is increased in the NE Pac, N Atlantic and Southern Indian Ocean. Interestingly, the CYGP predicts a low level of activity off the coast of Brazil where Hurricane Catarina struck in 2004 (McTaggart-Cowan et al., 2006) and in the Gulf of Guinea close to where a strong tropical depression/weak tropical storm formed in mid-April 1991 (McAdie and Rappaport, 1991). However, most noticeable is the inability of the index to predict TC formation in the NE Pac close to the coast. Similarly in the NW Pacific basin, TC activity is predicted to occur further East in the central Pacifc, leading to unrealistically high activity in that region. Finally, the CYGP removes the unusual activity predicted in the Red Sea, fails to predict TCs in the Arabian Sea and maintains TC activity too close to the Equator. Again, this result shows good agreement with that of Bengtsson et al. (2007a).

Both indices reproduce the seasonality of TC formation with reasonable accuracy (not shown). By comparing individual seasons, it is seen that the unrealistically high TC activity in the SH is mainly due to an overestimate of activity during the JFM season, although both parameters incorrectly predict some low level TC activity in the JAS (winter) season in this hemisphere.

It is tempting to try to detect a trend in TC activity using the ERA40 reanalysis data for the period 1958-2002. However, applying the SGP or CSGP technique to the recent past using ERA40 data, the number of TCs decreases in an unrealistic manner in all basins. Deriving the YGP for the period 1963-1982 from ERA40 data, we find the mean annual number of cyclones predicted drops to 50. Although there is some uncertainty in cyclone archives, such a large decrease in TC formation ($\sim 50\%$) is completely at odds with accepted trends in the global number of TCs over the recent past, which suggest a

relatively constant global TC number over the past 40 years, notwithstanding variations between individual basins (Webster et al., 2005).

The main factor responsible for this sharp reduction appears to be a significant reduction in the integrated water vapor content of the ERA40 atmosphere in the 1963-1982 period relative to the 1983-2002 era, leading to a large reduction in the humidity based parameters in the ERA40 YGP. Bengtsson et al. (2004) showed that this trend in IWV in ERA40 primarly arises from changes in observational coverage, in particular an increase in satellite coverage in the latter period, contributing to a moistening of the ERA40 atmosphere through increased data assimilation, rather than a real IWV trend. We can estimate the impact of such a dry bias on the YGP index by substituting the 1963-1982 relative humidity and specific humidity (used to calculate equivalent potential temperature) values for those of the 1983-2002 period and repeating the YGP calculations for the 1983-2002 period, with the new values and all other parameters unchanged. Doing so reduces the YGP from 75 TCs/year to 59 TCs/year. The remaining difference can be explained by a warming trend present in the lower troposphere in the reanalysis data. Again, according to Bengtsson et al. (2004), a large portion of this warming is caused by increased observational coverage in the latter time period. Substituting the surface temperatures (both atmosphere and ocean) of 1963-1982 into the 1983-2002 period futher reduces the (1983-2002) YGP to 43 TCs/year. The drier and colder atmosphere of the 1963-1982 period is also reflected in the reduction of convective precipitation and in the CYGP : substituting the 1963-1982 ERA40 convective precipitation in the 1983-2002 CYGP reduces the mean annual number of TCs from 75 TCs/year down to 63 TCs/year. We therefore conclude that the majority of any trend in implied TC frequency through the ERA40 period is mainly an artifact of changing observational coverage.

The SGP and CSGP obtained from the ERA40 reanalyses for the 1983-2002 period produce reasonably accurate estimates of the global mean TC activity, as well as the geographical and seasonal distribution lending some credence to the YGP and CYGP indices in evaluating CGCM simulated TC statistics. ERA40 will subsequently be used in conjunction with observations for comparison when the same analysis is performed on an ensemble of Coupled Global Climate Models (CGCMs) for a similar time period.

1.4 Evaluation of the YGP and CYGP in an Ensemble of CGCMs for the Climate of the 20th Century

1.4.1 Seasonal/Yearly Genesis Parameter

Nine CGCMs from the CMIP3 multi-model dataset were chosen to build an ensemble from which to evaluate the SGP and CSGP indices. The models were selected based on van Ulden and Oldenborgh's (2006) analysis of the quality of the simulated 20th century mean sea level pressure (MSLP) variability. Of particular interest was the mean spatial correlation and mean explained spatial variance of the MSLP over the whole globe and over the tropics specifically ($30°N - 30°S$).[4] Where data was available, we were guided by these two criteria, which partially defines the quality of the simulated large-scale atmospheric variability in a given CGCM, in selecting the best performing models.

This pre-selection of ensemble members might indeed underestimate the level of uncertainty in future TC trend, but probably increases the reliabiliy of the results by filtering out CGCMs that do not reproduce adequately the global and tropical large-scale circulation. The CGCMs retained are listed in table 1.3, along with the number of simulations produced for each GHG scenario listed in table 1.4. The YGP/CYGP for a given model is defined as the mean of an ensemble of integrations, for that model, for a given emission scenario or present-day control integration (i.e. only 1 YGP/CYGP value for a given model, for a given emission scenario, contributes to the multi-model ensemble).

We first evaluate the original YGP, with a fixed SST thresold of $26°C$ as suggested by Gray (1975) for the nine models and the ensemble mean YGP for the scenario 20c3m (climate of the 20th century), running from 1861-2000. This period is broken down into seven 20 year periods and the YGPs are calculated for each respective 20 year block. Figure 1.3 gives the mean annual number of TCs per 20 year period for each model and the ensemble mean using the YGP. Besides the mean annual number of cyclones being too low and the large differences between individual GCMs, an upward trend common to all models can be seen. Records of TCs preceeding the 1940s are scarce, but there

4. Also, some CGCMs had to be discarded due to data unavailibility at the time this study was performed.

does not seem to be any strong evidence to support such an upward trend in cyclogenesis over the last 140 years. In fact, these upward trends seem to confirm that at least part of the increase in TC formation detected by Ryan et al. (1992) and Royer et al. (1998) was due to weaknesses in the YGP itself.

To compensate for this trend, we now apply the correction suggested in section 1.2. We first increase the current period (1981-2000) SST threshold required for TC formation to $26.3°C$ and then, for each preceding 20 year period (or subsequent 20 year period in future climate scenario), we average the surface temperature over the tropical oceans ($30°S$-$30°N$) for each model individually and compare it to the average 20 year value of the reference period (1983-2002) for the same model. We then shift the threshold temperature for TC formation by this SST difference and recalculate the YGP for each 20 year period using this new SST threshold. This procedure is done separately for each simulation. The changes in the threshold value between 1861-1880 and 1981-2000 are relatively small for all models and vary between 0.98 $°C$ for CGCM3.1 to $0.27°C$ for ECHAM5. The resulting mean annual TC number using this adjusted YGP per 20 years period is given in figure 1.4. The upward trend over the past century is greatly reduced but is still apparent. To investigate the cause of this trend, table 1.5 presents an estimate, for each season, of the change in the individual parameters of the SGP over the 20th century. This is presented in the form of a ratio 1981-2000 : 1901-1920. The ocean thermal energy term does not contribute to the leftover trend, but the thermal potential is still responsible for it. This might be an indication that at least one other parameter requires some adjustment.

Comparing the geographical distribution of the adjusted YGP for the 1983-2002 period from the ERA40 reanalysis to the ensemble mean of the last 20 year period of the 20c3m simulation, 1981-2000 (figure 1.2d), we see that most main cyclogenesis areas depicted in the reanalysis are also present in the CGCM ensemble, although at a systematically lower intensity. Besides a general decrease in the number of TCs, TC formation in the CGCM ensemble mean is largely absent from the Gulf of Mexico and the Northern Atlantic, which seems primarly due to lower mid-tropospheric humidity in the ensemble compared to ERA40. Also, some unrealistic activity is predicted in the Southern Atlantic and off the coasts of South America. The activity in the Southern Atlantic arises because the mid-tropospheric humidity of the ensemble in that region is too high and passes the threshold of 40% required for TC development, whilst the activity off the

west coast of South America (Eastern Pacific) is due to an excess of ocean thermal energy during the JFM season, possibly due to a lack of stratocumulus clouds leading to a positive bias in surface short wave flux and a positive SST bias. Equally, a failure to accurately simulate ocean upwelling in the Eastern Pacific could lead to a similar positive SST bias. The ensemble YGP also predicts unrealistic TC formation in the Central Pacific. It should be noted that by tracking individual cyclones in ECHAM5, Bengtsson et al. (2007a) also detected TC formation in the latter region.

As in the reanalysis, the CGCM ensemble mean adjusted SGP gives a relatively accurate seasonal distribution of TCs for both JFM and JAS (not shown). Comparing the zonal mean distribution of TCs between the CGCM ensemble, reanalysis and observations (figure 1.5) clearly shows that both the ensemble and the reanalysis underestimate TC formation in the Northern hemisphere during JAS. In contrast, ERA40 overestimates TC formation in the Southern Hemisphere during JFM while the ensemble underestimates it. Comparing both the thermal and dynamical potentials for the period 1983-2002 (figure 1.6) for JFM shows that the $10°S-15°S$ band is where both potentials are larger in ERA40 than the ensemble while the higher level of activity in ERA40 during JAS is caused by a larger thermal potential across the Northern tropics (figure 1.6). Nevertheless, the CGCM ensemble components of the SGP show striking similarity to those in the reanalysis.

Because the index depends on climatological large-scale fields, we might expect that many simulations performed using the same model would return similar indices with a relatively small spread in the predicted number of cyclones. This turns out to be the case, as we can see from table 1.6, where the mean annual number of cyclones predicted by each model for the period 1981-2000 is given along with the standard deviation when the number of simulations was greater than 1. We observe a similar pattern whether we look at individual basins, seasons or different 20 years periods. This suggest that a large number of simulations from one model does not increase greatly the robustness of findings related to the YGP, at least at the basin scale.

In comparison, the large spread of simulated YGP between the individual models is more significant and adding or subtracting a model from the ensemble would have a much greater impact on the index of the ensemble than any of the internal variations

obtained from a single model, as can be seen from the standard deviaton of the YGP for the ensemble (33 TCs/year). Some of this spread can be attributed to differences in predicted ocean surface temperature in the tropics. For the period 1981-2000, as much as $2.3°C$ separates the model with the lowest tropical ocean surface temperature (BCCR2), located at the low end of the YGP spectrum to the warmest model (CSIRO3.5), located at the top end of the YGP spectrum. Also worth mentioning is the relative difference in mid-troposheric humidity over the tropical ocean between the individual models : more than 18% separates the driest model (MIROC) from the wettest model (ECHAM5) in the regions of cyclogenesis. Three out of the five models predicting lower activity than the ensemble mean (MIROC, HadGEM, CGCM3.1) have a mid-tropospheric relative humidity equal to or lower than 44% in the TC genesis regions while GFDL CM2.0, GFDL CM2.1, CSIRO3.5 and ECHAM5 have a mean value equal to or higher than 50%. For comparison, the mean value of mid-tropospheric humidity in ERA40 is 49%. Given that the humidity in the mid-troposphere is close to 40% in the regions of TC formation for the driest CGCMs, small differences in relative humidity translate into large differences in the YGP. In effect, those CGCMs fail to predict TC formation in many areas due to insufficient moisture in the mid-troposphere.

1.4.2 Convective Seasonal/Yearly Genesis Parameter

We now turn our attention to the aternative CSGP/CYGP index. Although it led to an underestimation of TC activity in the NH, we will consider the constant k found using ERA40 as an observational based estimate of k, linking convective precipitation to mid-tropospheric relative humidity, SST and equivalent potential temperature. Therefore, we use this value in deriving the CSGP for each respective model from equation 1.1. This means that we should not expect the annual mean number of cyclones for the individual models to be equal to the values found using the YGP. We evaluate the index for each 20 year period between 1861-2000, the same k value is used throughout the entire period implicitly assuming the relationship between convective precipitation and SST, mid-tropospheric RH and equivalent potential temperature are unchanged with time. The geographic distribution of the CYGP for the 1981-2000 period is given in figure 1.2e and the mean annual number of TCs per 20 year period for 1861-2000 is given in figure 1.7.

Using this index, there appears to be almost no trend in the overall number of cyclones

over the course of the past 140 years (figure 1.7). This seems to support the hypothesis that the index adjusts to match changes in surface temperatures (Royer et al., 1998) and that, if we hope to detect a realistic trends in future TC activity, the CSGP/CYGP seems to be the most appropriate index.

For the 1981-2000 period, the mean annual number of TCs from the CGCM ensemble is 75, the same as estimated with ERA40 (the mean for individual CGCMs is given in table 1.6). However, the geographical distribution is somewhat different from the observations and is more similar to the one obtained from the reanalysis, with too high TC formation in the Central Pacific and Western-South Pacific and some unrealistic activity in the Southern Atlantic and Eastern South Pacific. Also, as in previous cases, TC formation is predicted too close to the Equator and underestimated across the Northern Hemisphere. Figure 1.5b clearly shows this underestimate in the NH in both ensemble and reanalysis. Whether this indicates common errors in simulating/analysing the large-scale tropical climate between the global reanalyses and CGCMs or a more systematic weakness in the YGP/CYGP statistic is beyond the scope of this study. Finally, the patterns of the CSGP for the ensemble also follow closely the patterns of CSGP for the reanalysis (not shown).

Figure 1.8 compares the longitudinal distribution of observed TC formation with that predicted from the YGP and CYGP using the reanalysis and the ensemble mean averaged over the latitude band 35 $N-35$ S. Both show good agreement with observerations, but neither of the indices manage to capture the concentrated location of formation in the East Pacific. This problem is not unique to these indices and also occurs when tracking individual cyclones (McDonald et al., 2005; Yoshimura et al., 2006), although when using this technique, there seems to be a definite improvement with increasing resolution. It is known that a significant fraction of TC development in the NE Pac occurs through an interaction of Atlantic tropical waves and depressions with Central American orography (Zehnder et al., 1998). Vortex stretching on the downwind (western) side of the Central American mountains can locally increase cyclonic vorticity in an evolving tropical disturbance and potentially be the seed for TC genesis in the East Pacific. This type of local dynamical interaction will not be included in the YGP/CYGP indices that only consider larger scale controls on TC development. The NE Pac is the only region where strong interaction between local orography and TC precursors takes place and seems to suggest the YGP and CYGP indices might not be applicable in this region.

Differences in the CYGP index between individual models again far outweight differences obtained from various simulations of the same model, as can be seen from table 1.6. The standard deviation in the mean annual number of TCs is reduced using the CYGP, but is still substantial (25% of the mean annual number of predicted TCs). Except for MIROC, CSIRO3.5 and ECHAM5, all models show an increase in their annual mean number of TCs compared to the YGP, the most dramatic being HadGEM and BCCR2 which increase by a factor $\sim$ 3 and 5, respectively. This wide variety of responses may originate from the different convection schemes used in the models, which may each trigger and support deep convection at different ocean temperatures and/or atmospheric stability or humidity values.

In order to justify the choice of the nine CGCMs that we have used, we performed a similar analysis using a smaller ensemble of three CGCMs, each of which were classified as performing poorly based on the analysis of van Ulden and Oldenborgh (2006). The YGP and CYGP of these three CGCMs (GISSeh, IPSL4, PCM) are displayed in figure 1.9. Both indices suffer from the poorer simulation of large-scale tropical climate variability in these CGCMs : both indices predict a larger number of TCs in the SH than in the NH (see table 1.1) and both extend TC activity into the South Eastern Pacific. The YGP of the second ensemble also fails to predict high level activity in the Western North Pacific while the CYGP predicts more activity in the Southern Atlantic than in the Northern Atlantic. Hence, as should be expected, both parameters simulate a more accurate distribution of implied TCs when using CGCMs with an accurate representation of large-scale atmospheric variability compared to TC statistics derived using less accurate models. We therefore consider it important that a pre-selection of sufficiently accurate GCMs is made based on performance for the present, observed climate, before an analysis of future TC changes is made. This exercise led to the 9 CGCMs used in this study.

1.5 Future Tropical Cyclone Activity

Having established for the nine member CGCM ensemble that the CYGP and adjusted YGP provide reasonable estimates of the annual number of TCs along with a reasonable depiction of the spatial and seasonal distribution of TCs, we now apply these indices to results originating from a variety of future climate scenarios generated by the same

nine CGCMs. In assessing possible future TC activity, we will use three sets of model projections, each based on a different GHG emission scenario for the next 100 years. In the optimistic scenario, SRES B1, equivalent CO_2 concentrations reach 550 *ppm* by the year 2100, in the pessimistic scenario SRES A2, 850 *ppm* and in the intermediate scenario SRES A1B, 720 *ppm* (Nakićenović and Swart, 2000).

We begin by evaluating time series of the mean annual number of cyclones per 20 years for the period 2001-2100 for both indices in the SRES A1B scenario. Results using the adjusted YGP are shown in figure 1.10 and using the CYGP, in figure 1.11. The adjusted YGP shows a somewhat steeper upward trend. From table 1.7, the influence of the thermal energy content is greatly reduced compared to previous studies; instead, a large portion of the increase may be attributed to an increase in the moist static stability term. How much of this trend is artificial due to shortcoming of the index itself is unknown. Based on the analysis of results for the period 1861-2000 we contend the CYGP index provides a more accurate representation of past TC activity and therefore feel this index is the most appropriate one to use when considering future trends in TCs. The CYGP shows a small upward trend in the mean annual number of cyclones per 20 years. The increase between 1981-2000 to 2081-2100 for the ensemble mean is found to be 5 TCs/year, up to an mean annual value of 80 TCs/year. A similar analysis for SRES A2 and SRES B1 gives an increase of 5 TCs/year and 3 TCs/year, respectively. As can be seen in figure 1.11, no global trend common to all CGCMs can be detected since the responses vary between a moderate increase ($> 10\%$) (MIROC, ECHAM5, CSIRO3.5), small increase ($< 10\%$) (HadGEM, MRI, BCCR2), no trend (GFDL CM2.0, GFDL CM2.1) and a slight decrease (CGCM3.1). However, this global trend can be misleading because all CGCMs do predict changes in locations of cyclogenesis, even if they do not predict a global change. For example, HadGEM predicts a large increase in the WN Pac, compensated by a decrease in the SH, the more pronounced decrease being in the South Indian Ocean [5]. Similarly, GFDL CM 2.0 predicts an increase in activity in the WN Pac compensated by a decrease in the SW Pacific.

Figure 1.12 shows the geographical distribution of ensemble mean TC changes between 2081-2100 and 1981-2000 for the three emissions scenarios. The ensemble mean increase

5. For comparison, the study performed by McDonald et al. using HadCM found an increase in the South Indian Ocean and both areas of increased and decreased activity in the WN Pac.

is not uniformly distributed but mostly concentrated in the WN Pac basin and compensated by a small decrease in the SH. For comparison, the difference between the 1981-2000 climate and the 1901-1920 climate is also shown in figure 1.12d. The mean annual change per basin is given in table 1.8[6]. The increase in the WN Pacific is even more pronounced in SRES A2 than in SRES A1B but is relatively weak in SRES B1. In both SRES A1B and SRES A2, there appears to be a reduction in TC formation along the coast of Central America in the NE Pac, accompanied by an increase further off the coast. This pattern is also predicted in Bengtsson et al. (2007b), but given that cyclogenesis is poorly represented by our indices in this basin, this result should be taken with caution. Also, there appears to be a small overall reduction of TC formation in the Southern Hemisphere. However, this reduction is quite weak and it is questionable if, were it to occur, it could be detected relative to natural interannual variability. Very little change is expected in SRES B1 and no new regions of cyclogenesis are apparent in any of the scenarios. For the scenario where most models were used, SRES A1B, most of the increase in the Western North Pacific occurs during JAS (53%), while the second largest increase occurs during OND (31%) (not shown) which would result mostly in a more active typhoon season. No significant increase is predicted in the non-typhoon seasons. The increase in TC formation during the summer season in that region is caused by an increase in both convective and dynamical potentials. More specifically, the vorticity term becomes more conducive to TCs, while the wind shear remains at current level (not shown).

1.6 Conclusion

We have analysed, using ERA40 reanalysis data and what was deemed the more accurate IPCC AR4 models, two parameters believed to accurately represent current TC activity based on large-scale climate controls. Using reanalyses, both the YGP and CYGP manage to capture the major areas of cyclogenesis, although they systematically underestimate TC activity in the NH. By using an ensemble of CGCMs, we see a degradation in the representation of current regions of cyclogenesis and their intensity level, which is caused by the CGCMs failure to adequately simulate large-scale fields used in the evaluation of the indices. By looking at past trends, we deemed the CYGP index to be more robust to changes in climate conditions and have attempted, based on

6. In order to avoid biaises, in the case where no simulation was available for a model for a certain scenario, this model was removed from the ensemble before comparing future and present climate conditions

that parameter, to predict future TC activity. With this approach, very little change between current and future TC activity is expected : in only one basin in two out of three scenarios do we detect a change greater than the observed interannual variability of that particular basin.

The weak positive trend for future climate scenarios found in this study is not unlike that of Stowasser et al. (2007) which predicts a slight increase (although no statistically significant) in the number of TCs in the NW Pac in a $6 \times CO_2$ atmosphere. It does contrast sharply however with other studies based on the comparison of the TCLVS which predict an overall reduction in the number of cyclones in the future. In particular, recent papers by Oouchi et al. (2006) and Bengtsson et al. (2007b) predict a reduction in the number of cyclones in the NW Pacific. However, as mentionned earlier, these TCLVs are not TCs and so, any changes in one cannot be absolutely confidently transfered to changes in the other.

Similarly, investigating future TC activity by looking at the large-scale fields favorable to TC formation carries its own uncertainties. It should be remembered that, while the CYGP gives reasonable results for present climate conditions, this does not guarantee that

1. the index will work well in future climate conditions (as the example of the YGP has shown) and, maybe even more importantly, that
2. current CGCMs correctly simulate future large-scale climate conditions that will occur in the tropics and influence the CYGP implied TC numbers.

It is likely that, until CGCMs significantly increase their resolution to adequately simulate past observed TC statistics, variability, intensity and structure, any possible changes in TC activity in response to a changing climate will remain uncertain at best.

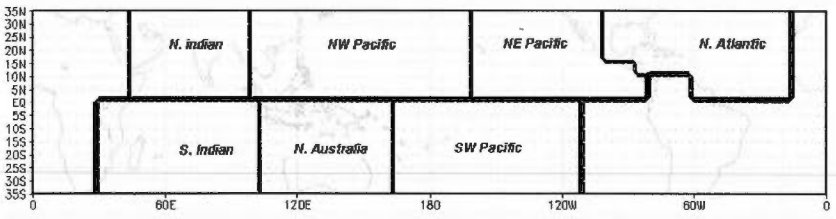

Figure 1.1 Geographical location of the different basins.

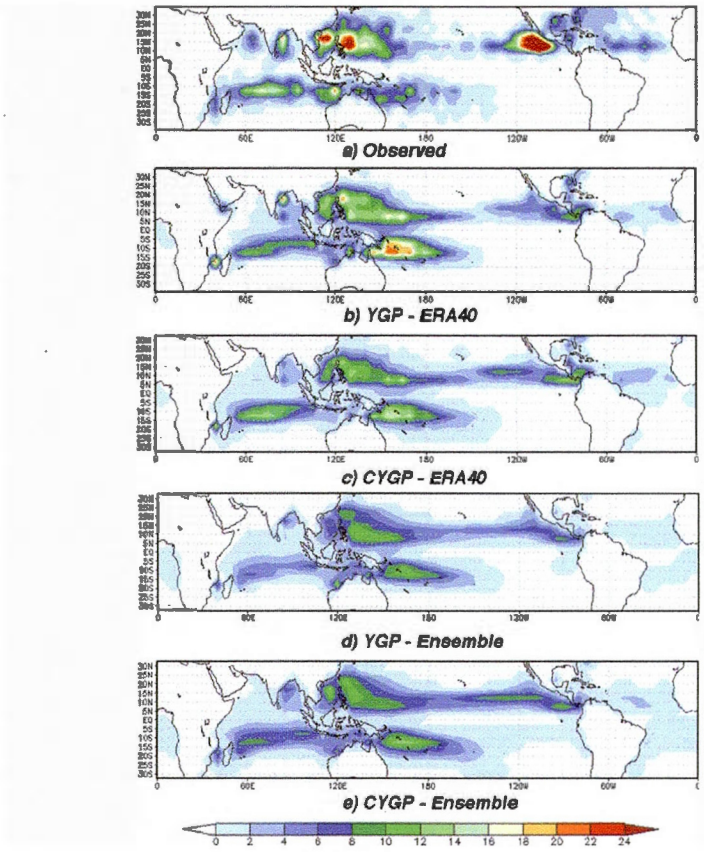

Figure 1.2 Geographical distribution of TCs observed (a) and predicted with the adjusted YGP (b) and CYGP (c) in ERA40 reanalysis data, for the 1983-2002 period. Also, the predicted geographical distribution of TCs using the adjusted YGP (d) and CYGP (e) in an ensemble of 9 CGCMs for the period 1981-2000. The units are TCs per 20 years per 5°latitude-longitude.

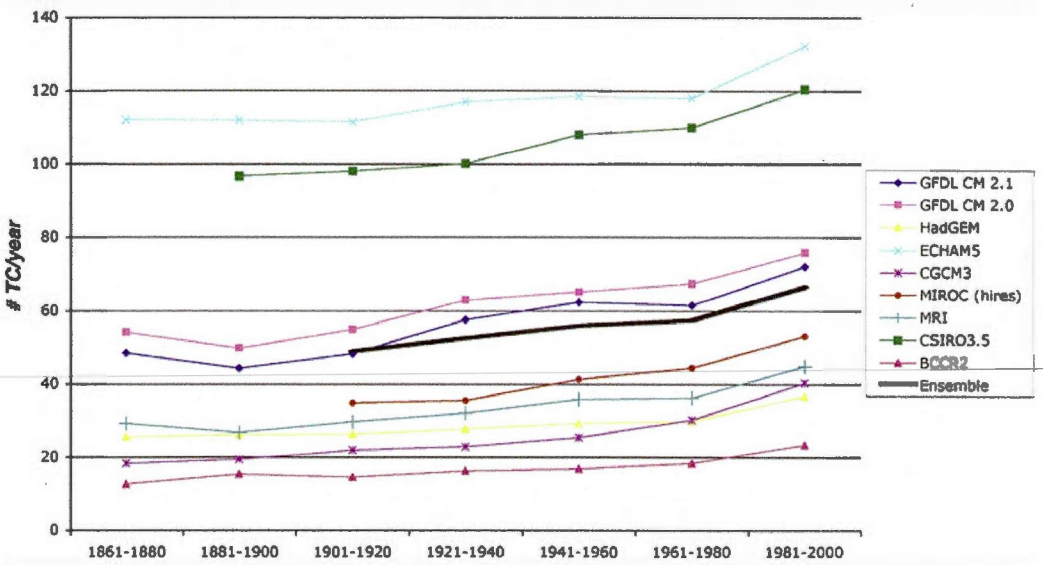

Figure 1.3 Time series of the mean global annual number of TCs based on the original YGP in nine CGCMs for the period 1861-2000 in the 20c3m scenario.

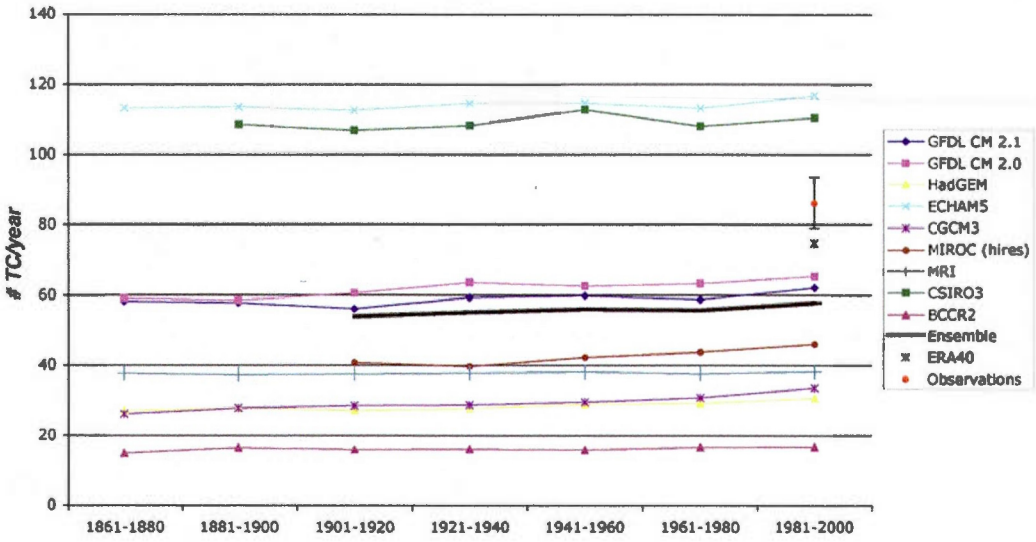

Figure 1.4 Time series of the mean global annual number of TCs based on the adjusted YGP in nine CGCMs for the period 1861-2000 in the 20c3m scenario. Also shown is the mean global annual number of TCs observed and derived from the adjusted YGP using ERA40 reanalysis for the period 1983-2002.

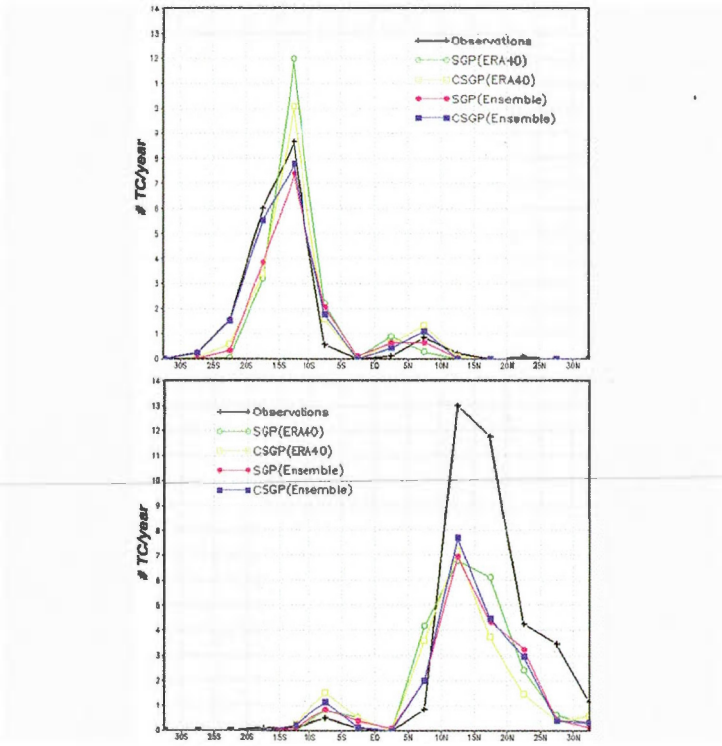

Figure 1.5 Mean annual latitudinal distribution of observed and predicted TCs for JFM (a) and JAS (b). Observations and ERA40 reanalysis cover the period 1983-2002; the ensemble covers the period 1981-2000.

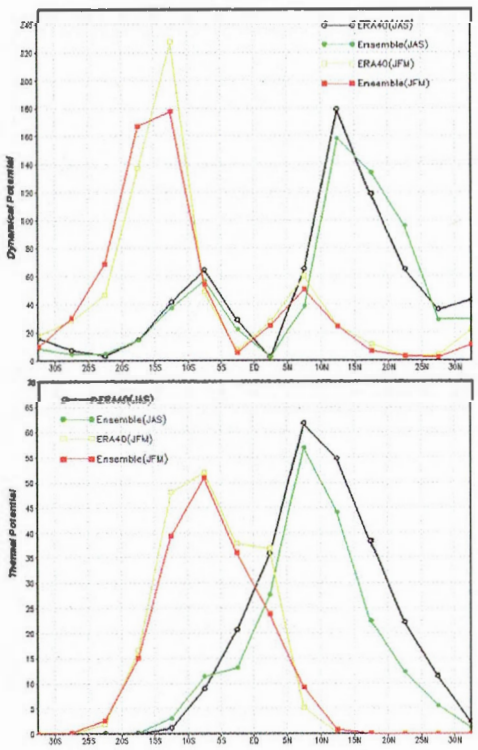

Figure 1.6 Zonal sum of the dynamical (a) and thermal (b) potential for ERA40 (1983-2002) and the ensemble (1981-2000) for JFM and JAS.

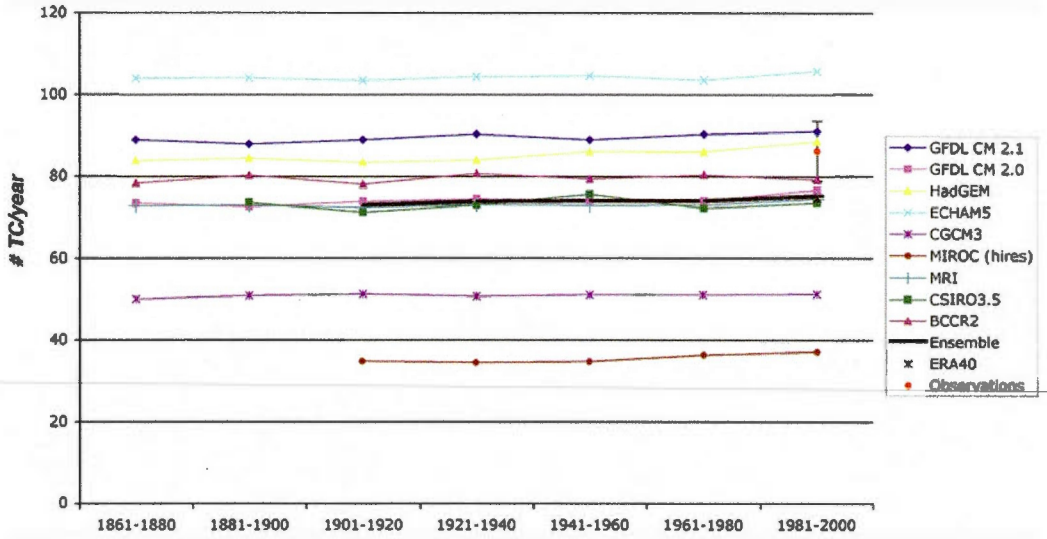

Figure 1.7 Time series of the mean global annual number of TCs based on the CYGP in nine CGCMs for the period 1861-2000 in the 20c3m scenario. Also shown is the mean global annual number of TCs observed and derived from the CYGP using ERA40 reanalysis for the period 1983-2002.

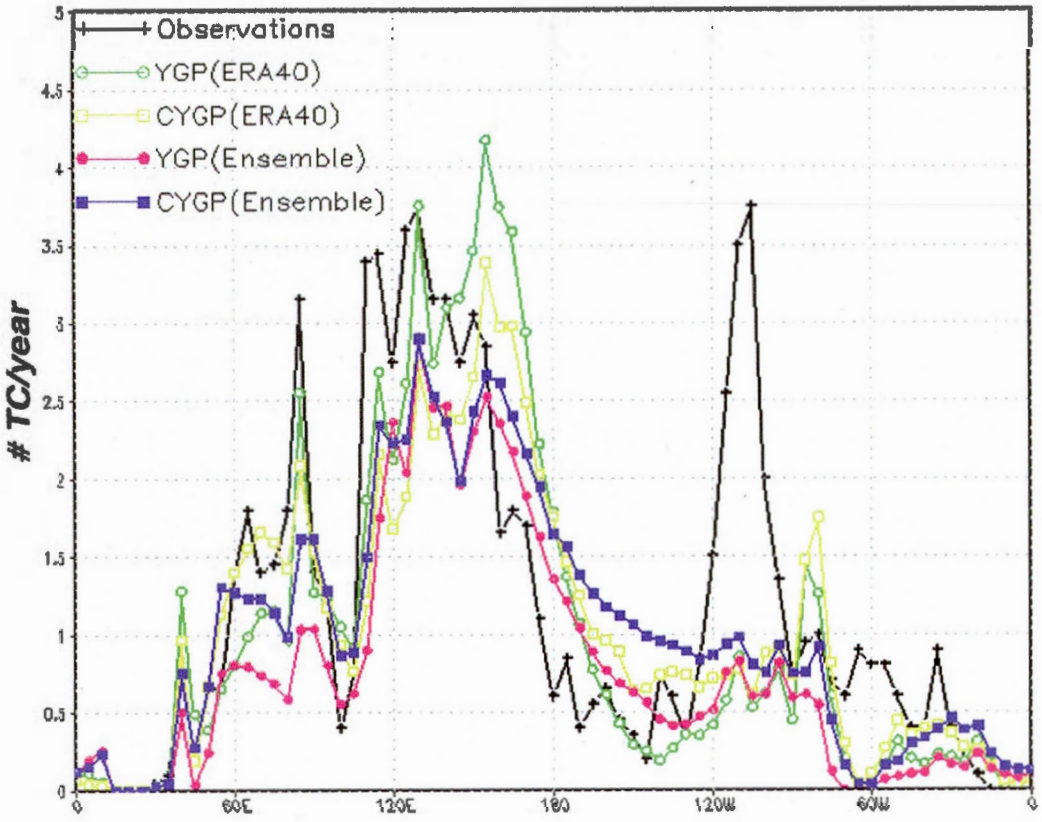

Figure 1.8 Mean annual longitudinal distribution of TC cyclogenesis. Observations and ERA40 reanalysis cover the period 1983-2002 ; the ensemble covers the period 1981-2000.

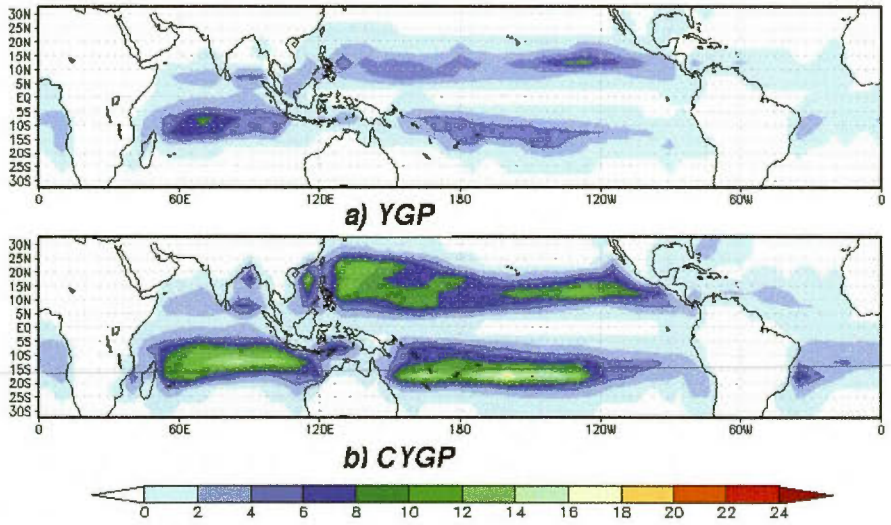

Figure 1.9 Predicted geographical distribution of TCs using the adjusted YGP (a) and CYGP (b) in the second CGCMs ensemble for the period 1981-2000. The units are TCs per 20 years per 5°latitude-longitude.

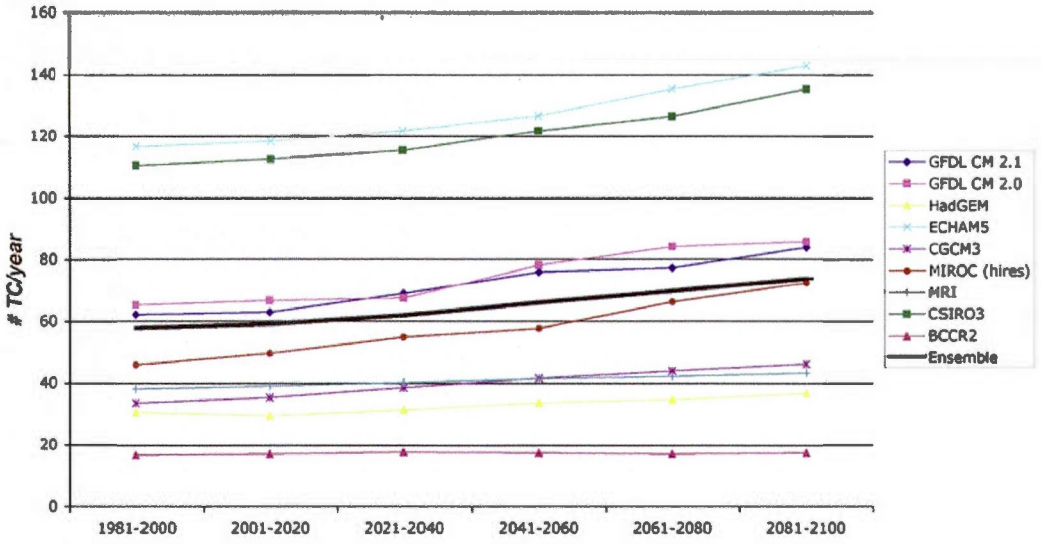

Figure 1.10 Time series of the mean global annual number of TCs based on the adjusted YGP in nine CGCMs for the period 1981-2100 in the SRES A1B scenario.

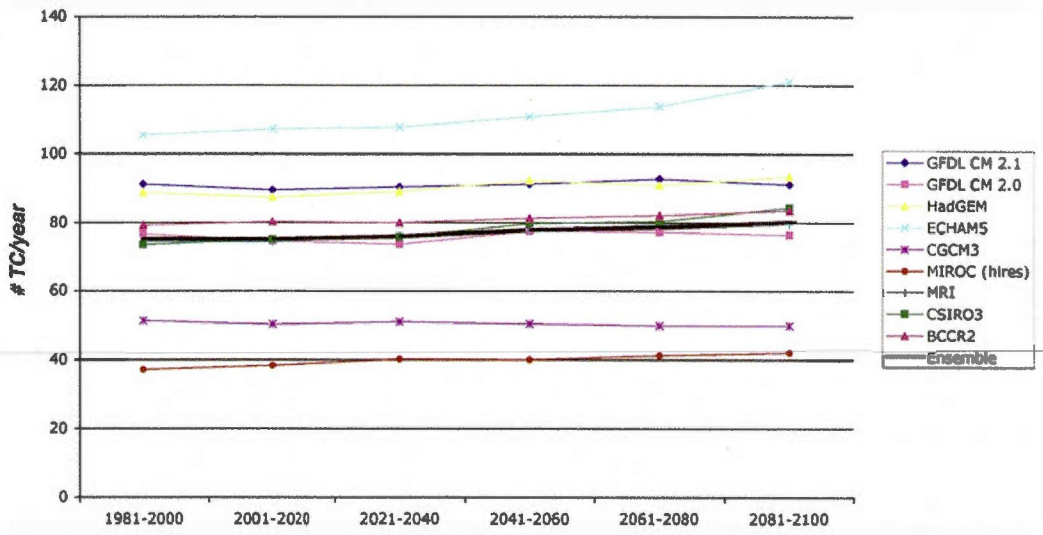

Figure 1.11 Time series of the mean global annual number of TCs based on the CYGP in nine CGCMs for the period 1981-2100 in the SRES A1B scenario.

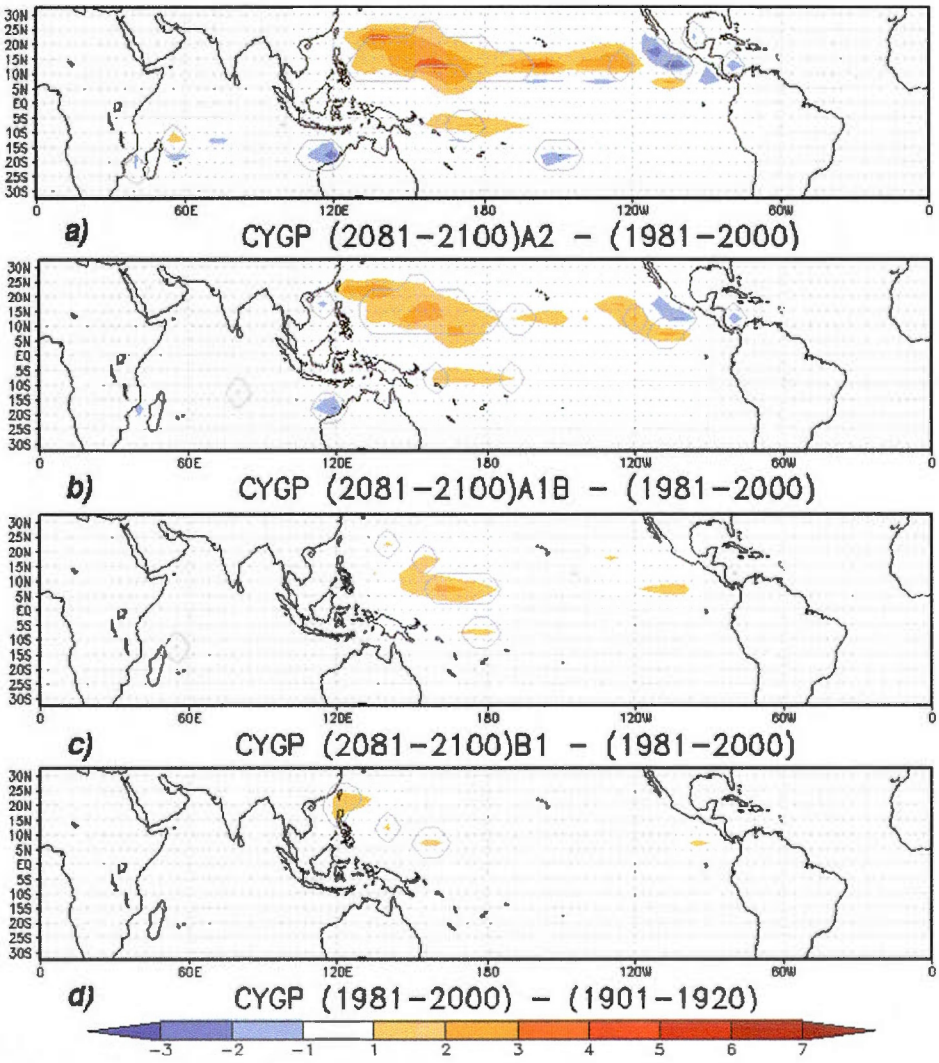

Figure 1.12 Geographical change in TCs frequency between the 2081-2100 period in SRES A2 (a), SRES A1B (b), SRES B1 (c) and the 1981-2000 period using the CYGP. For comparison, the difference between the 1981-2000 period and 1901-1920 period using the same index is also shown (d). The gray lines show the areas where a change is predicted by more than 75% of the CGCMs.

Tableau 1.1 Mean annual global number of TCs detected and predicted at end of the 20th century and percentage of TCs occurring in the northern and Southern Hemisphere. The figure following the ± sign gives the standard deviation of the observed annual value over the 20 year period.

	mean number of TC/year	%NH / %SH
Observations (1983-2002)	86.1± 7.3	69.1/30.9
ERA40 YGP (1983-2002)	75	57/43
ERA40 CYGP (1983-2002)	75	56/44
First Ensemble YGP (1981-2000)	58	58/42
First Ensemble CYGP (1981-2000)	75	55/45
Second Ensemble YGP (1981-2000)	43	47/53
Second Ensemble CYGP (1981-2000)	102	45/55

Tableau 1.2 Mean annual number of TCs per basin at the end of the 20th century. The figure following the ± sign gives the standard deviation of the observed annual values over the 20 year period.

	N Ind	NW Pac	NE Pac	N Atl	S Ind	N Aus	SW Pac
Observations (1983-2002)	4.8 ± 2.2	27.9 ± 4.0	16.5 ± 4.2	10.2 ± 3.7	11.9 ± 2.5	9.0 ± 3.0	5.8 ± 3.6
ERA40 YGP (1983-2002)	3.1	26.5	6.4	3.8	9.5	12.1	9.6
ERA40 CYGP (1983-2002)	2.2	21.7	9.2	6.3	12.8	8.6	8.9
Ensemble YGP (1981-2000)	1.9	20.6	8.1	1.4	6.7	8.2	7.4
Ensemble CYGP (1981-2000)	3.1	22.5	11.2	2.7	11.2	9.1	10.3

Tableau 1.3 CGCMs included in this study; first and second ensemble.

CMIP3 I.D.	Short name	Country	Atmospheric Resolution	Reference
BCCR-BCM2.0	BCCR2	Norway	$T63, L31$	Furevik et al. (2003)
CGCM3.1 (T63)	CGCM3.1	Canada	$T63, L31$	Flato (2005)
CSIRO-Mk3.5	CSIRO3.5	Australia	$T63, L18$	Gordon et al. (2002)
ECHAM5/MPI-OM	ECHAM5	Germany	$T63, L31$	Jungclaus et al. (2006)
GFDL-CM2.0	GFDL2.0	USA	$2.5° \times 2.5°, L24$	Delworth et al. (2006)
GFDL-CM2.1	GFDL2.1	USA	$2.5° \times 2.5°, L24$	Delworth et al. (2006)
MIROC3.2 (hires)	MIROC	Japan	$T106, L56$	K-1 model developers (2004)
MRI-CGCM2.3.2	MRI	Japan	$T42, L30$	Yukimoto and Noda (2002)
UKMO-HadGEM1	HadGEM	UK	$1.875° \times 1.25°, L38$	Johns et al. (2004)
GISS-EH	Gisseh	USA	$5° \times 4°, L24$	Schmidt et al. (2006)
IPSL-CM4	IPSL4	France	$2.5° \times 3.75°, L19$	Marti et al. (2005)
PCM	PCM	USA	$T42, L18$	Washington et al. (2000)

Tableau 1.4 Total number of simulations used for each scenarios.

Model name	Scenario 20c3m (Climate of the 20th Century)	Scenario B1 550 ppm stabilisation	Scenario A1B 720 ppm stabilisation	Scenario A2 850 ppm stabilisation
BCCR2	1	1	1	1
CGCM3.1	1	1	1	0
CSIRO3.5	1	1	1	1
ECHAM5	3	2	2	2
GFDL-CM2.0	3	1	1	1
GFDL-CM2.1	3	1	1	1
MIROC	1	1	1	0
MRI	3	2	3	2
HadGEM	2	0	1	1
Total	18	10	12	9

Tableau 1.5 Seasonal ratio of 1981-2000 to 1901-1920 for the parameters and potentials of the adjusted YGP.

	I_{RH}	I_θ	E	Thermal potential	I_ζ	I_{WS}	Dynamical Potential
JFM	1.04	1.04	0.97	1.05	1.01	1.01	1.01
AMJ	1.03	1.05	0.96	1.02	1.00	1.01	1.00
JAS	1.01	1.05	0.98	1.03	1.08	1.02	1.03
OND	1.01	1.05	0.99	1.04	1.00	1.02	1.00

Tableau 1.6 Comparison of the mean annual number of cyclones between the CGCMs and the ensemble using the YGP and CYGP for the period 1981-2000. The figure following the $\pm$ sign for individual CGCMs gives the standard deviation across the available simulations made with that specific CGCMs while the figure following the $\pm$ sign for the ensemble gives the standard deviation across all the different CGCMs. If no $\pm$ sign is present, no ensemble was available for that particular CGCM.

Model name	adjusted YGP	CYGP
BCCR2	16.7	79.0
CGCM3.1	33.4	51.1
CSIRO3.5	110.4	73.5
ECHAM5	116.5 ± 5.8	105.5 ± 0.6
GFDL-CM2.0	65.0 ± 2.6	76.6 ± 0.6
GFDL-CM2.1	61.9 ± 1.7	90.9 ± 0.8
MIROC	45.8	37.0
MRI	38.0 ± 0.3	74.4 ± 0.6
HadGEM	30.4 ± 0.8	88.5 ± 0.7
Ensemble	58 ± 33	75 ± 19

Tableau 1.7 Seasonal ratio of 2081-2100 (SRES A1B) to 1981-2000 for the parameters and potentials of the adjusted YGP.

	I_{RH}	I_θ	E	Thermal Potential	I_ζ	I_{WS}	Dynamical Potential
JFM	1.08	1.23	0.88	1.21	1.00	1.04	1.00
AMJ	1.02	1.26	0.90	1.14	0.93	0.99	0.93
JAS	1.05	1.28	1.01	1.48	1.00	1.03	1.02
OND	1.13	1.26	0.91	1.41	1.03	1.04	1.02

Tableau 1.8 Percentage changes per basin in the mean annual frequency of TCs between future scenarios (2081-2100) and the 1981-2000 period using the CYGP index. For comparison, the changes over the period 1901-1920 to 1981-2000 are also shown. In bold are the changes larger than the observed annual standard deviation over the 20 year period (1983-2002).

	Observed number of TCs	Change in SRES A2	Change in SRES A1B	Change in SRES B1	Change in 20c3m
N Indian	$4.8 \pm 46\%$	16%	10%	6%	−1%
WN Pacific	$27.9 \pm 14\%$	**22%**	**16%**	10%	7%
EN Pacific	$16.5 \pm 25\%$	6%	10%	4%	1%
N Atlantic	$10.2 \pm 36\%$	−24%	−11%	−4%	−4%
S Indian	$11.9 \pm 21\%$	−4%	−1%	1%	3%
N Australia	$9.0 \pm 33\%$	−4%	−3%	−1%	−1%
WS Pacific	$5.8 \pm 62\%$	5%	3%	4%	4%

CHAPITRE II

IMPACT OF RESOLUTION AND DOWNSCALING TECHNIQUE IN SIMULATING RECENT ATLANTIC TROPICAL CYLONE ACTIVITY

Abstract

Using the Global Environmental Multiscale (GEM) model, we investigate the impact of increasing model resolution from 2° to 0.3° on Atlantic tropical cyclone activity. There is a clear improvement in the realism of Atlantic storms with increased resolution, in part, linked to a better representation of African Easterly Waves. The geographical distribution of a Genesis Potential Index, composed of large-scales fields known to impact cyclone formation, coincides closely in the model with areas of high cyclogenesis. The geographical distribution of this index also improves with resolution.

We then compare two techniques for achieving local high resolution over the tropical Atlantic : a limited-area model driven at the boundaries by the Global 2° GEM simulation and a Global Variable resolution model (GVAR). The limited-area domain and high-resolution part of the GVAR model coincide geographically, allowing a direct comparison between these two downscaling options. These integrations are further compared with a set of limited-area simulations employing the same domain and resolution, but driven at the boundaries by reanalysis.

The limited-area model driven by reanalysis produces the most realistic Atlantic tropical cyclone variability. The GVAR simulation is clearly more accurate than the limited-area version driven by GEM-Global. Degradation in the simulated interannual variability is partly linked to the models failure to accurately reproduce the impact of atmospheric teleconnections from the Equatorial Pacific and Sahel on Atlantic cyclogenesis.

Through the use of a smaller limited-area grid, driven by GEM-Global 2°, we show that an accurate representation of African Easterly Waves is crucial for simulating Atlantic

tropical cyclone variability.

2.1 Introduction

Satellite data gathered during the last ~25 years suggest an increase in the intensity of the strongest tropical cyclones (TCs) in some basins (Elsner et al., 2008), but only the Atlantic shows a reliable increase in the Power Dissipation Index (PDI; a measure of the cube of the storm maximum wind speed over the lifetime of the storm) (Emmanuel, 2005) in the recent past (Kossin et al., 2007). The reasons behind this recent upswing in Atlantic hurricane activity are still debated. The increase has been linked to rising Atlantic sea surface temperatures (SSTs; Emmanuel, 2005), which itself has been linked to anthropogenic climate change (Mann and Emanuel, 2006; Trenberth and Shea, 2006), natural multidecadal cycles in ocean circulation (Goldenberg et al., 2001) and, most recently, to aerosol effects (Evan et al., 2009). Regardless of the cause(s) behind the increase in SSTs, if Atlantic tropical cyclone activity is indeed primarily modulated by SST, it is reasonable to expect atmospheric global climate models (AGCMs) driven with prescribed SSTs to be capable of reproducing some of the observed trends with some level of skill. This would seem to be a prerequisite to provide confidence in estimates of future tropical cyclone activity from coupled ocean-atmosphere climate models.

It has long been recognized that Global Climate Models (GCMs) are capable of producing systems reminiscent of tropical cyclones (Manabe et al., 1970). Coined Tropical Cyclone-Like Vortices (TCLVs; Walsh and Watterson, 1997), these systems share similar characteristics to their observed counterparts, such as a warm core structure and cyclogenesis/formation location. Also, if originally the TCLVs tended to be much weaker, while significantly larger than real storms (Haarsma et al., 1993; Bengtsson et al., 1996), mostly a consequence of GCMs' low resolution, recent studies at high resolution ($20 - 100\ kms$) significantly improve the realism of these storms (Oouchi et al., 2006). Nevertheless, even at these high resolution, storm intensity as measured by maximum 10 m wind speed is still quite weak compared to observations. The implicit assumption in these studies is that issues regarding tropical cyclone intensity vs cyclogenesis and cyclone frequency/geographical distribution are decoupled and can be studied separately. As an example, this would allow the possibility to study interannual variability of TCs even though individual storm intensity was not simulated properly. Recent studies

performed in the tens of kms of resolution appear to support this hypothesis. Using a limited-area model (LAM) at $\sim 18\ km$ driven at the boundaries by NCEP analysis (and using spectral nudging to constrain the LAM-simulated large scale flow), Knutson et al. (2007) managed to reproduce the interannual hurricane variability over the Atlantic for a 26-year period (1980-2005) quite realistically, with a timeseries correlation between observed and simulated annual hurricane numbers of 0.86. For the same time period, Zhao et al. (2009), using a GCM four member ensemble in the 40-60 km range, also managed to recreate past Atlantic hurricane activity (correlation index of 0.83), but with a weaker upward trend than observed for recent years. Finally, Larow et al. (2008), using an AGCM at $\sim 0.94°$ resolution managed to capture a fairly realistic (timeseries correlation index of 0.78 for Atlantic tropical storms) activity, although for a somewhat shorter time period (1986-2005).

Variability in the observed TC activity can be captured by models because storm activity is 1) dependent on the underlying SST and induced changes in atmospheric large-scale fields and 2) these large-scale features are generally reproduced reasonably well in AGCMs. That cyclogenesis depends on large-scale fields is in fact the premise behind the use of seasonal genesis indices, like the Genesis Potential Index (GPI ; Emanuel and Nolan, 2004), Seasonal Genesis Parameter (SGP ; Gray, 1975) and Convective Seasonal Genesis Parameter (CSGP ; Royer et al., 1998) that have been used to study TC variability in low-resolution GCMs (Caron and Jones, 2008 ; Vecchi and Soden, 2007). Assuming the controls on cyclogenesis remain valid in future climate conditions, these indices are also an indirect way by which one can estimate future tropical cyclone activity.

It is worth pointing out that in the three aforementioned high-resolution studies, the ensemble mean always gave a better correlation than did individual simulations, highlighting the stochastic nature of cyclogenesis, even for very similar large-scale conditions, and thus the benefit of an ensemble approach (this appears to be true of low-resolution simulations as well Camargo et al. (2005)). Ideally, in investigating past TC activity, one would perform multiple global, high-resolution simulations. Unfortunately, this is not presently feasible, except on the most powerful supercomputers. Even then, such runs tend to be so computationally expensive that they cannot be performed multiples times, thus prohibiting a potentially beneficial ensemble analysis (Oouchi et al., 2006). An alternative to running a global model is the use of a Regional Climate Model (RCM), wherein only the region of interest is integrated at high-resolution, considerably redu-

cing the necessary computer power. This technique allows to maximize local resolution and to increase the number of simulations at the cost of global high resolution coverage. Lateral and surface boundary conditions are supplied to the RCM from an integration of a low-resolution GCM or reanalysis over the same time period. This approach has been used successfully in a number of studies (Knutson et al., 2007; Walsh et al., 2004)

Another technique to increase resolution over a limited area is the use of a variable resolution GCM, referred to hereafter as GVAR. In this case, resolution is increased over an area of interest while the rest of the globe is run at a lower resolution (Courtier and Geleyn, 1988; Fox-Rabinovitz et al., 2001). This second approach to high-resolution climate modelling is computationally more expensive to run than the typical GCM-RCM approach since the timestep for the entire global simulation is set by time step requirements of the inner, high resolution region. On the other hand, the approach offers the desirable feature of a mutually (2-way) interacting flow at the boundary between the finer (inner region of interest) and coarser resolution area (the surrounding outer region). This may be of particular importance with regard to problems treating the advection of weather systems (such as TCs) in and out of the RCM domain. To our knowledge, Chauvin et al. (2006) are the only ones who have applied this technique to study long-term tropical cyclone activity.

In this study, we use both the GCM-RCM and the GVAR approach to investigate the benefits of increased resolution, local to the tropical Atlantic, for simulating TC variability. We compare the two approaches in the same modelling system and contrast each to a range of fixed-resolution GCM simulations for the same time period. We further discuss the importance of accurate lateral boundary conditions for TC simulation.

In section 2.2, we give a description of the model used and of the experimental set-up. In section 2.3 we describe the tracking algorithm used to assess TC activity, while in section 2.4 we look directly at the impact of increasing resolution on TC activity. In sections 2.5 and 2.6, the simulated climatology and interannual variability of Atlantic TCs is evaluated using a range of high resolution simulations. An emphasis is placed on understanding and evaluating the large-scale controls on TC activity resulting from variability in the El Niño-Southern Oscillation (ENSO) in the tropical Pacific and variability in African Sahel rainfall. Concluding remarks are in section 2.7.

2.2 Model Description and Experiment Configuration

2.2.1 A brief description of GEM

The Global Environmental Multiscale (GEM) model is a fully non-hydrostatic model, employing a semi-implicit, semi-Lagrangian dynamical core on an Arakawa staggered C-grid. The model uses a hybrid-terrain-following vertical coordinate (Simmons and Burridge, 1981) with 60 levels (top at 2 hPa) in global-variable resolution mode and 53 levels (top at 10 hPa) in limited-area mode (see below). GEM uses the Kain-Fritsch scheme (Kain and Fritsch, 1990) for deep convective processes, the Kuo transient scheme for shallow convection (Kuo, 1965; Bélair et al., 2005), the Sundqvist scheme (Sundqvist et al., 1989) for large-scale condensation and the correlated-K scheme for solar and terrestrial radiation (Li and Barker, 2005). Subgrid-scale orographic gravity-wave drag is due to McFarlane (1987) and low-level orographic blocking to Zadra et al. (2003). Land surface processes are represented by the ISBA scheme (Bélair et al., 2003). Finally, sub-grid scale turbulent fluxes are calculated using an implicit vertical diffusion scheme with prognostic turbulent kinetic energy and a mixing length based on Bougeault and Lacarrère (1989) (Bélair et et al., 1999). The interested reader is referred to Zadra et al. (2008) and Côté et al. (1998) for more details.

2.2.2 Model Configuration

GEM offers a great deal of flexibility for configuring the horizontal meshing. It can be run in limited or global area extent. In the case of global coverage, the horizontal resolution may be uniform or variable. For this experiment, we take full advantage of this flexibility by integrating the model in a number of different configurations : (i) a 2° and 1°global, uniform resolution grid (GEM-Global), analogous in resolution to present-day GCMs used in climate change modelling and climate change prediction (figure 2.1a); (ii) a Global Variable Resolution (GVAR) grid, where the area of high resolution (0.3°) extends from the Eastern Pacific to the Arabian Sea and between $\sim 5°S$ and $\sim 45°N$ while the remaining part of the Globe is covered at 2° resolution (figure 2.1b); (iii) a Limited-Area (LAM) domain also at 0.3° resolution covering the same area as the high resolution region of the GVAR simulation (figure 2.1c); (iv) and a smaller, 0.3° fixed resolution grid covering only the tropical and sub-tropical Atlantic (figure 2.1d).

In GEM-LAM the prognostic variables at the lateral boundary are updated every 6 hours with a linear interpolation in time using the one-way nesting technique of Davies (1976). The lateral boundary conditions (LBCs) for the large grids are (i) output from the GEM-Global 2° integration (hereafter referred to as LAM-GEM), and (ii) European Centre for Medium-Range Weather Forecasts (ECMWF) Reanalysis data (ERA-40 ; Uppala et al., 2005) (hereafter referred to as LAM-ERA). Since ERA-40 does not extend beyond August 2002, we use the ECMWF operational analyses for the 2002-2006 period. In contrast to the study of Knutson et al. (2007), no large-scale spectral nudging has been performed in this study.

Comparing simulations performed using different LBCs (reanalysis vs GEM output) will highlight the importance of accurately simulated processes, external to the tropical Atlantic, influencing simulated TC activity through the lateral boundaries. Comparing grids i) and ii) above will highlight the benefit of increasing local resolution in simulating TC activity while comparing ii) and iii) will allow comparison of the two downscaling techniques available to increase resolution over a given area. Finally, comparing iii) and iv) will yield information on the importance of employing high resolution to also simulate African Easterly Waves (AEWs), which often act as precursor systems for downstream cyclogenesis (Landsea et al., 1998).

All integrations have been performed using observed SSTs and sea-ice fraction derived from the Atmopsheric Model Intercomparison Project v2 (AMIP2 ; Gleckler et al. 1996), applied in the model on a daily basis from linearly interpolated monthly mean data. Global integrations for both uniform and variable grids were started on September 1st, 1978, and ended on December 1st, 2006, thus covering 28 Atlantic hurricane seasons (1979-2006). The LAM simulations were integrated for 6-month periods starting on June 1st (first ensemble member) or June 2nd (second ensemble member) for the same 28-year period. In all, we have covered 224 overlapping hurricane seasons spread across 8 experiments, 6 of which employ high-resolution over the tropical Atlantic.

2.3 Tropical Cyclone Detection and Tracking

The most efficient way to assess TC activity and interannual variability is by tracking individual storms through an automated procedure and thereby build up seasonal totals of TCs as a function of geographic location and year. We adopt such an approach in this

study, with the detection and tracking of tropical cyclones performed in two distinct steps. In the first step, potential storms are identified if certain atmospheric conditions are satisfied for a given timestep. As pointed out by Walsh et al. (2007), different TC criteria have been used by different groups with no agreed upon standard. Most of the methodological differences arise when trying to numerically identify whether the storms exhibit warm-core characteristics, which would set them apart from their cold-core, mid-latitude cyclone counterparts. Also, changes in horizontal resolution impact the different threshold criteria used in selecting possible storms, such as maximum wind speed, leaving much freedom for "tuning" these thresholds so that model results better fit the observed climatology.

Here, we apply Walsh et al.'s (2007) recommendations with regard to tropical cyclone detection. Since the goal is to perform an objective evaluation of the model, we make no particular effort to optimize the simulations with regard to the observed climatology. Thus, a potential storm is detected if :

- there is a minimum in central pressure [1].
- there is a relative vorticity maximum at 850 $hPa > 4 \times 10^{-5}\ s^{-1}$. This condition is added in order to reduce the number of local minima detected with condition 1.
- the surface (10 m) winds exceed 17 $m\ s^{-1}$ (65 $km\ h^{-1}$) in the vicinity ($< 2°$ for high resolution simulations) of the center. For the 2° and 1° simulations, we lowered the maximum wind speed threshold following Walsh et al. (2007) to 13 ms^{-1} and 15 ms^{-1} respectively.
- the number of consecutive, detected centers cover at least a 24 h period [2].
- a positive temperature anomaly is present in the mid- to upper-troposphere. This warm core anomaly is detected if the maximum (spatially-mean) temperature, in the vicinity ($< 2°$ for high resolution simulations) of the center at 500 hPa and 250 hPa, is $> 1°C$ and $> 0°C$, respectively, higher than the mean temperature at a radius of $< 5°$ for the same two pressure levels.

---

1. In the cases where two minimum in pressure were recorded within a $< 2°$ radius of each other, the highest pressure coordinate was discarded

2. This value was chosen in order to allow direct comparison with the storms stored in the National Hurricane Center best track database (HURDAT; available online at http ://www.nhc.noaa.gov/pastall.shtml).

- the low-level (850 hPa) vorticity is higher than the upper-level (250 hPa) vorticity. This condition further discriminates between cold core and warm core systems.

As in Gualdi et al. (2008), we find the total number of detected storms is not particularly sensitive the specific threshold value chosen, such as the differences in upper tropospheric temperature or the maximum in relative vorticity, as long as they are kept relatively low. The results are also not affected by the requirement that a minimum distance be traveled by any given storm. Once a given storm has been identified at a given timestep, it is linked/added to an existing track if it occurs within 2° and 24 h of the last coordinate of any given track. If multiple tracks qualify, priority is given to the closest one.

One problem we found using these conditions was the double counting of storms which weakened for a short period, only to later reintensify. This issue has already been recognized and addressed differently in Camargo and Zebiak (2002) and Chauvin et al. (2006). Here, we use another approach, wherein we utilize only a subset of the previous detection criteria and rerun the tracking procedure. We then compare the two sets of tracks, retaining only the tracks that were detected with both sets of criteria. The second set of criteria are :

- a minimum in central pressure.
- a maximum in vorticity greater than $4. \times 10^{-5}\ s^{-1}$.
- surface wind speed greater than $10\ m\ s^{-1}$ in the vicinity of the center.
- low-level (850 hPa) vorticity greater than upper-level (250 hPa) vorticity (implicitly a warm core).

In essence, we run the same tracking procedure but do not require the systems to display a warm core anomaly in the upper troposphere and lower the nearby threshold wind speed limit needed to qualify. In doing this, if an identified TC weakens and does not satisfy the first set of conditions but does the second, it will be retained as a single TC for the full track length rather than as two separate shorter TC tracks. This technique also provides the added benefit of extending the track of a storm back to its original disturbance, often an African easterly wave. An example of the improvement given by this technique can be seen in figure 2.2, which shows two sets of TC tracks for the same season (1997) from the same dataset (LAM driven by ERA-40). In the upper panel only the first detection scheme has been applied while in the lower panel both schemes have

been used.

Finally, it should be mentioned that the tracking procedure requires a minimum number of model grid points to be executed, meaning that cyclones will not be detected close to the boundaries of the limited area domain even though vorticity, wind, warm core and pressure conditions are fulfilled. This is not an issue on the southern, western nor eastern side of the domain, since the boundaries are a large distance from TC activity, but storms coming close to the Northern boundary ($\sim 45°\ N$) that recurve South can be lost and then double counted when the algorithm detects them for a second time. This type of boundary problem has earlier been pointed out by Landman et al. (2005). For that reason, the few storms entering the LAM domain through the Northern boundary at tropical cyclone strength ($> 17\ m\ s^{-1}$) or higher are not considered to be new storms but an extension of a previous storm.

The TC tracks detected are then used to create maps of track densities over the Atlantic, which allows easy comparison of TC activity between the different integrations and with TCs archived in HURDAT.

2.4 Impact of Resolution

We begin investigating the impact of increasing model resolution on simulated TC activity by comparing global TC activity in the fixed-resolution GCMs at 2°, 1° and GVAR (0.3°) simulation for 1979-2006. Table 2.1 displays the total number of storms for each simulation along with the observed number from the HURDAT database. Increasing resolution from 2° to 0.3° over the Atlantic increases the number of simulated storms from an unrealistically low total (63) to a more realistic (282) over the given period.

Increasing resolution appears to increase the realism of the TC geographical distribution. The left column in figure 2.3 shows all TCs detected between 1979-2006, plotted by the geographic location where they were first identified as TCs (location of cyclogenesis) by white dots. Values are plotted for GEM-Global 2° and 1°, as well as for GVAR and observations. Figure 2.4 shows the related TC tracks. Most TCs forming in the low-resolution 2° GCM are grouped in an area east of the American coast, with only a few storms forming in what is commonly referred to as the Main Development Region

(MDR; between $5°N$ and $20°N$ over the Atlantic). This situation is in sharp contrast with the GVAR simulation, where a large number of storms form just off the coast of Africa and through the MDR. The overall geographic distribution and number of TCs in GVAR is clearly closer to observed values (figure 2.3) than GEM 2°, with GEM 1° exhibiting some improvement over the 2° run. It should be pointed out that the absence of TC activity in the MDR in low-resolution simulations (GEM 2°) does not appear to be caused by a wind speed threshold that may have been set too high in the detection scheme, since further lowering the threshold increases the number of storms close to the American East coast, but does not change the total in the MDR (not shown). The absence of an active MDR is not unique to GEM and has been detected in simulations performed with other climate models (ECHAM4, ECHAM5, CCM3, NSIPP) at similar resolution (Camargo et al., 2007a). These simulations are in sharp contast to the low-resolution simulation of ECHAM3, which did display an active MDR (ibid.).

Changing the wind speed detection threshold in the Global 1° simulation, originally set to 15 $m\ s^{-1}$, to 14 $m\ s^{-1}$ or 16 $m\ s^{-1}$ has a somewhat significant impact on the total number of TCs, going from 110 to 171 and 75 respectively. However, the distribution in the Atlantic basin remains similar, with a larger proportion of storms forming close to the U.S. East coast and a smaller number now forming in the MDR. Irrespective of which of the three wind speed threshold are chosen, the total TC number in the Global 1° simulation remains higher than in the Global 2° and lower than in the GVAR simulation.

We define TC track density as the total number of detected tracks in a 5° by 5° grid box over the 26-year period, divided by the number of years simulated. This value is then smoothed by averaging the eight grid points surrounding the main analysis grid point with a one to eight weighting and dividing the total by two. The right column in figure 2.3 plots the climatological TC track density for observations (taken from HURDAT), GVAR and the GEM 2° and 1° runs. The improvement in cyclogenesis location seen in the left column also leads to more realistic tracks[3] (figure 2.4) and track densities : as resolution is increased, more storms originating from AEWs tend to form off the coast of Africa and then propagate across the Atlantic.

3. The jumpy looking tracks in GEM 2°, and to a lesser extent in GEM 1°, are caused by the coarse resolution of these simulations.

To get an idea of the general thermodynamic structure of simulated TCs in Figure 2.5 we plot four vertical profiles of the temperature anomaly (relative to the mean temperature over a 5°, 10°, 20° radius for 0.3°, 1°, 2° model resolutions respectively) and the horizontal winds for a composite of three storms at maximum intensity (all plots centered on the pressure minima) produced in the a) global 2°, b) 1° and c) d) GVAR (0.3°) integrations. Storms in 2.5a, 2.5b and 2.5c were chosen such that they were all located in the same general vicinity (around the Florida peninsula), and such that central pressures were nearly equal in all three sets of storms, all between 983 hPa (the lowest pressure detected in GEM 2°) and 998 hPa. Storms in 2.5d had central pressure between 952 hPa and 958 hPa, some of the stronger cyclones detected in the GVAR simulation. All composites show similar patterns, typical of TCs, with the maximum positive temperature anomaly occurring in the center of the storm, in the mid- to upper troposphere, and maximum horizontal winds occurring around 900 hPa to 850 hPa, near the pressure minimum, and progressively decreasing away from the center of the storm. However, the difference in size between the different resolution is quite substantial : the strongest winds in the 2°, 1° and 0.3° occur respectively at 5°, 2.5° and 1° from the center of the storm. There also appear to be an increase in wind intensity for a similar central pressure as resolution in increased : maximum winds go from 95 $km\ h^{-1}$ to 115 $km\ h^{-1}$ to 125 $km\ h^{-1}$, likely due to conservation of angular momentum as air propagates towards the storm center. This is not entirely surprising and was the reason for using different threshold values when detecting the TCs. Finally, the warm cores of the systems become increasingly confined to the upper troposphere as model resolution becomes finer and low-level wind speeds increase around the storm centre. Such a response to the increased vertical shear is to be expected from the thermal wind relation.

2.4.1 Large-Scale Fields

In this section, we compare TC distributions to a cyclogenesis potential index comprised of large-scale fields known to influence TC formation. In assessing this index, we aim to determine 1) if the various versions of GEM accurately simulate the large-scale fields known to influence TC activity, 2) if 1) is reasonably satisfied, whether the link between this large-scale index and the actual simulated number of TCs follows the observed relationship, and 3) whether these points are sensitive to model resolution and, in a later section, to the type of downscaling used (GVAR or LAM).

The selected fields are the vertical wind shear (V_{shear}) between the upper (200 hPa) and lower (850 hPa) troposphere, low-level (850 hPa) vorticity (ζ), mid-tropospheric humidity (700 hPa, $\mathcal{H}$) and atmospheric instability, as expressed by the Maximum Potential Intensity (MPI), which represents the theoretical maximum 10 m wind speed of a mature tropical cyclone given the current atmospheric instability and ocean surface temperatures[4] (Emanuel, 1995). Together, these fields make up the Genesis Potential Index (GPI; Emanuel and Nolan, 2004; Camargo et al., 2007b), defined as

$$\mathrm{GPI} = |10^5\eta|^{\frac{3}{2}} \left(\frac{\mathcal{H}}{50}\right)^3 \left(\frac{\mathrm{MPI}}{70}\right)^3 (1+0.1V_{shear})^{-2} \tag{2.1}$$

where η is the absolute vorticity. The GPI has been shown to be a good predictor of tropical cyclone activity (Camargo et al., 2007a). This index is somewhat similar to Gray's SGP, but addresses the issue of the climate change dependent SST parameter (Ryan et al., 1992) by integrating its influence into the maximum potential intensity term.

Figure 2.3 shows the GPI as derived from ERA-40 and four GEM simulations as well as the corresponding cyclogenesis locations taken from HURDAT and the GEM integrations. The figure indicates a good correspondence between cyclogenesis locations and high mean August-September-October (ASO) GPI values, for all GEM resolutions. As resolution is increased, there is a decrease in GPI for a large region east of the American coast and an increase over the MDR. These changes are consistent with a shift towards a higher proportion of storms forming over the MDR in the high-resolution simulations. The high GPI values in the global 2° simulation east of the American coast are due to mid-tropospheric relative humidity being $5-10\%$ higher than in the high-resolution simulation. This $5-10\%$ increase leads to large increase in the GPI since the latter increases as the cube of the relative humidity. It is worth noting that this increased value of the GPI is not associated with a larger number of TCs in the 2° GCM. In fact, even though the GPI is locally lower in GVAR compared to the 2° GCM, the number of cyclogenesis points in the Carribean/Gulf of Mexico is significantly higher. Aside from the changes in the GPI in the Gulf and off Africa between 2° and 1° runs, the overall GPI fields simulated by GVAR and the GCM runs are quite similar. This is also true for the individual components of the GPI.

4. Details on MPI are given in appendix A

Comparison between ERA-40 and GEM relative humidity indicates why much fewer tropical cyclones form in the Gulf of Mexico compared to observations : the monthly mean relative humidity over the Gulf is significantly lower in GEM during the beginning of the hurricane season (not shown). For the individual months of August and September, relative humidity is respectively $\sim$ 20% and $\sim$ 10% lower in the GVAR integration than the ERA-40 mean value of 55%. The underestimation of relative humidity is present in the high-resolution LAM simulations as well. A dry bias of 10%-20% in the mid-troposphere will strongly reduce the GPI value in the model (figure 2.3), making the Gulf region less conducive for TC formation. Physically, a mid-tropospheric dry bias will inhibit the development of organized deep convection and thereby TC formation. Such a dry bias may be due to a positive westerly wind bias in the upper troposphere in GEM. This westerly bias at 200 hPa leads to an excess upper level convergence and subsidence over the Gulf. The bias also leads to higher wind shear over the Gulf of Mexico and the Caribbean Sea during the months of August and September, further contributing to lower GPI values over the region.

Weak TC activity and mid-tropospheric humidity climatological values below reanalyses level over the Gulf of Mexico could also reflect a failure to accurately simulate the Madden-Julian oscillation (MJO). It is known that the MJO impacts TC activity in the Gulf of Mexico (Maloney and Hartmann, 2000) and it was shown that certain phases of the MJO act to increase the GPI over that particular region, predominantly through an increase in mid-tropospheric humidity (Camargo et al., 2009). Failure to realistically reproduce the MJO could prevent GEM from increasing relative humidity above the threshold needed to support deep convection and thus keep our TC numbers down over the Gulf of Mexico. However, an analysis of the MJO in GEM is beyond the scope of this study.

The mean MPI ASO values are quite similar across all simulations (not shown) and do not differ significantly from reanalysis. This is not surprising, since the MPI is closely tied to SST, which is based on observations in all simulations. Similarly, mean low-level vorticity in ASO for all simulations compares favorably to ERA-40 reanalysis (not shown), although it is somewhat lower in the Global 2° over the MDR.

It appears unlikely that the small differences in the large-scale fields could be solely responsible for the large difference in cyclogenesis and track density seen between GVAR and the 2° and 1° runs. Using the ECHAM5 model, Camargo et al. (2007a) found the GPI to increase over the Atlantic as resolution was progressively raised from T42 to T159. This led them to conclude that "when the horizontal resolution of the model is increased, not only is there an improvement in the dynamics of the simulated TC-like disturbances, but the environmental conditions become more conducive to generation of TCs" (ibid.). Their conclusion does not apply here, as the GPI response to change in resolution appears to be region dependent and relatively modest. If the GPI in the MDR increases with resolution, the region East of the American coast shows a higher GPI in the low-resolution than in all high-resolution simulations, in direct opposition to the cited conclusion. It would thus appear that in the case of GEM, the large increase in TC formation between low- and high-resolution simulations is primarily due to an improvement in the local interaction between large-scale fields and storm dynamics and in the dynamics of the storm itself. The negative bias in the GVAR GPI over the Gulf of Mexico is accompanied by a negative bias in cyclone numbers, suggesting the link between large-scale fields and TC formation is well represented in GVAR. Our results also suggest that, for a given region, higher GPI values would be required, on average, to produce TCs in low-resolution simulations. This is supported by the absence of storms in the MDR in GEM-Global 2°, even though the GPI is only slightly lower than in the high-resolution integrations.

Finally, the inability of the low-resolution model to simulate TCs in the MDR may also be related to its difficulty in simulating upstream AEWs, which tend to be weaker as they leave the African coast than in high-resolution simulations and die out when reaching the Atlantic ocean. It is well established that AEWs are important precursors for downstream cyclogenesis (Thorncroft and Hodges, 2001) and the inability to properly simulate AEWs coud lead to an inability to simulate realistic Atlantic tropical cyclone activity. To illustrate this further, we have used a small LAM grid at 0.3° resolution (figure 2.1d), driven at the boundaries by the low-resolution (GEM 2°) simulation over the same 28-year period. Cyclogenesis/GPI and track density for this integration are shown in figure 2.3e and figure 2.3ee and can be compared to the same results from the driving GEM 2° run. In this LAM, a number of TCs do form in the MDR, but in much fewer number than the GVAR simulation, which has the same resolution local to the LAM region, but 0.3° resolution also over Africa. Nevertheless, the increased number

of TCs in this small LAM compared to the driving GCM, underlines the importance of local resolution for representing Atlantic TC dynamics. The small LAM appears to also have inherited larger GPI values east of the American coast from its pilot GCM, thus leading to unrealistically high activity over the region. Comparing the track density for this simulation with observations (HURDAT) clearly shows an underestimation over the MDR combined with an overestimation over the subtropical Atlantic.

We cannot yet exclude that the treatment of LBCs plays a role in the poor representation of TC activity in 2.3e. However, simulations performed with the smaller grid (figure 2.1d) but using ERA-40 as LBCs show a much more active MDR, thus supporting the idea that the impact of AEW simulation on cyclogenesis appears to be resolution dependent in GEM.

2.5 Climatology of High-Resolution Simulations

In the previous section, we discussed the benefits of increasing GEM resolution from 2° to 0.3°. We now concentrate on the high resolution simulations and compare the various downscaling options. This analysis will highlight both the treatment of LBCs and their quality on simulated TC activity.

We start by comparing cyclogenesis locations, shown as dots in figure 2.6, and total storm numbers (table 2.1), for observations, GVAR and the two large LAM simulations driven by GEM 2° (LAM-GEM), for the 1979-2006 period, and two similar LAM domains driven by ERA-40/ECMWF boundary conditions (LAM-ERA). Figure 2.6 shows cyclogenesis locations and GPI for the two LAM-GEM and LAM-ERA runs and the mean track density for each set of LAM runs. The LAM integrations produces somewhat too many TCs, in contrast to the GVAR configuration (figure 2.3). The differences between the GVAR and LAM-GEM TC climatology is mostly due to higher activity East of the American coast in LAM-GEM. In fact, the geographical distribution of TCs simulated with the GVAR configuration is quite similar to observations and the difference in the total count between the two comes mostly from the Caribbean Sea and the Gulf of Mexico, where simulated activity is about half of what is observed. This lack of activity in the Gulf of Mexico and the Caribbean Sea appears common to the LAM-GEM simulations also, even if they tend to produce too many cyclones overall. The lack of cyclogenesis in this region should be expected considering the difference in

GPI simulated by the various GEM runs and that seen in ERA-40. It shows the TC processes in the model respond correctly to the large-scale, even when the large scale is in error. While there is some variability between individual simulations, all exhibit a fairly realistic geographical distribution of cyclogenesis with a significant number of TCs originating from African easterly waves and propagating into the Atlantic from West Africa.

The track densities in figure 2.6 are fairly realistic, although the model is too active in the sub-tropical Atlantic. This hyper-activity contrasts with the relative inactivity in the Gulf of Mexico and Caribbean Sea. The differences in cyclogenesis locations and track densities between the different sets of LAM integrations appear coherent with differences in GPI values. The ERA-40 driven LAM displays higher ASO GPI values near the Cape Verde region, off the African coast, and also produces more TCs in this region than does LAM-GEM. This increase in GPI in the LAM-ERA integrations is linked to a decrease in vertical wind shear over this particular region. The higher wind shear in LAM-GEM appears to have been inherited from the southern boundary, since the pilot, GEM 2°, displays higher wind shear values than ERA-40 reanalysis also in that region (not shown).

Similarly, over the Caribbean Sea, wind shear and mid-tropospheric subsidence are significantly reduced in the ERA driven runs, a region where the LAM driven by ERA-40 produces more TCs than the GVAR and LAM-GEM simulations. The lower wind shear in the LAM-ERA integrations is somewhat closer to the wind shear seen in the ERA-40 fields, while GVAR and both LAM integrations forced by the GEM-Global 2°, display high wind shear in these regions, similar to the forcing GEM-Global 2 run. This suggests the difference between the simulated shear is directly inherited through the (southern) lateral boundary. The excessive wind shear in GEM is linked to excessive convective activity over the South American continent : stronger convection in GEM over the Amazon modifies both low-level and upper-level wind fields such as to increase vertical wind shear over the Caribbean.

In figure 2.7a and 2.7b, we assess the intensity distribution of simulated TCs. This is done by plotting the frequency of occurrence of maximum wind speed (at 10 m) and minimum sea level pressure from two simulations (GVAR and one LAM-GEM) and

observations. Figure 2.7a indicates that GEM fails to simulate wind speeds of category 2 or higher on the Saffir-Simpson scale ($> 42\ ms^{-1}$). On the other hand, the lowest simulated central pressures (figure 2.7b) are typical of hurricanes up to category 3. This discrepancy is not unique to GEM and has been detected in previous studies (Knutson et al., 2007; Bender et al., 2007). It appears the observed relation between minimum central pressure and maximum wind speed does not hold in GEM's simulated TCs, as can be seen in figure 2.7c, which compares the covariability between maximum wind speed and minimum central pressure, for the two simulations, against observations. In both cases, as the central pressure drops below $\sim 1000\ hPa$, the associated maximum wind speed in GEM becomes increasingly biased low compared to observations at a similar central pressure. It has been suggested that failure to properly represent momentum exchange between the ocean and the atmosphere at very high wind speed is at least partly responsible for this discrepancy (Moon et al., 2007; Walsh et al., 2009). In GEM, the momentum transfer to the ocean, as defined by the drag coefficient (C_d), increases linearly with wind speed, whilst observations suggest the momentum transfer levels off, and maybe even decreases, for surface winds reaching the $30-35\ ms^{-1}$ range and higher (French et al., 2007). Powell et al. (2003) speculated that the presence of a sea foam layer caused by intense wave breaking over the ocean surface led to a reduction of momentum transferred to the ocean for very high wind speed. Preliminary tests performed with GEM suggest that by capping the momentum transferred to the ocean, through using a constant C_D value for winds $\gg 17\ ms^{-1}$, higher, hurricane-strength, wind speeds are produced and the relation between simulated central pressure and maximum wind speeds improves significantly. We are currently testing modified versions of the drag coefficient in GEM, which better fits observations. Results from these tests will be reported subsequently.

Figure 2.8 shows the intra-seasonal distribution of TCs for two simulations (GVAR and LAM-GEM). September is the most active month, similar to observations, but too much activity tends to occur late in the season and too little in August. In August, simulated activity is generally lower than observations primarily due to lack of activity in the Gulf of Mexico present in all simulations. This is due to the negative bias in mid-tropospheric relative humidity in that region (discussed in section 2.4.1). In LAM-GEM, this is compensated by an unusual large number of storms forming close to the American East Coast. In fact, most of the extra TCs detected in LAM-GEM compared to GVAR and LAM-ERA over that region occur in the June-July-August period. Comparison of the

different GPIs do not offer a satisfactory answer as why this is so, since climatological values are comparable for that period over that region. A possible explanation for these differences might lie with the position of the jet stream, which appears located further South in the LAM-GEM integrations. This southern shift could send precursor disturbances further South, where atmopheric conditions and SSTs are more conducive to cyclogenesis.

Finally, higher October TC activity seems to result from the combination of two factors in GEM : formation of many TCs off the coast of Africa, which is unusual for this time of year, and too many cyclones forming over the middle of the sub-tropical Atlantic Ocean. In both these regions, simulated vertical wind shear is lower than in ERA-40 reanalysis for that particular month.

2.6 Interannual Variability

In this section we compare the model's ability to reproduce the observed Atlantic interannual variability over the study period. By comparing the simulated interannual variability of the different integrations with observed activity, we hope to better understand the limitations of the different techniques used here.

We selected four different metrics to evaluate the model's ability to reproduce Atlantic TC interannual variability over the 28-year period :

- annual number of tropical cyclones ;
- annual number of hurricanes (storm with maximum wind speed greater than 33 ms^{-1}) ;
- annual number of tropical cyclone days ;
- annual power dissipation index (PDI), defined as the cube of the storm maximum wind speed summed over the lifetime of each storm.

We restrict our analysis to the high-resolution simulations only, since the lower (2° and 1°) resolution TC distributions are quite poor. For this analysis, we group together the three simulations for which the large-scale fields outside the region of interest were simulated by GEM at low resolution (2 LAM-GEM and GVAR) and the two simulations for which the LBCs were prescribed by reanalysis (LAM-ERA).

Annual mean time series for the four variables, for observations and each individual simulation, plus the ensemble mean, are shown in figure 2.9. The runs forced by GEM simulated large-scale fields are on the left, while those forced by ERA are on the right. Individual correlation coefficients are displayed in table 2.2 while the respective linear trends of each time series are given in table 2.3. Although there are large differences between individual runs, both ensemble means manage to capture a significant fraction of the variability in TCs, hurricanes and TC days. Not surprisingly, the ERA-driven simulations perform better, especially with respect to TC interannual variability, emphasizing the importance of large-scale variability, external to the Atlantic, for Atlantic TC simulation. For all metrics, the ensemble mean tends, on average, to perform better than individual integrations. From table 2.3, only the LAM-ERA integrations capture the upward trend in hurricane numbers and TC days, observed over the study period.

The ensemble means do not always capture the very quiet years (1982, 1983), nor the very active years (1995, 2005). It is worth pointing out that the LAM-ERA integrations seem to reproduce the interannual variability more accurately than the LAM-GEM or GVAR integrations (correlation coefficients for TCs being 0.72 vs 0.5, for hurricanes 0.68 vs 0.58 and for TC days, 0.72 vs 0.67) due to better large-scale control at the boundaries from ERA-40 data. For a similar period, using a smaller LAM domain and spectral nudging, the correlation index of Knutson et al. (2007) for TCs and hurricanes were respectively 0.74 and 0.86. The use of spectral nudging forces the large-scale fields simulated with the LAM domain to more closely follow the evolving, prescribed boundary forcing field. When accurate large-scale fields are available, such as the reanalyses, this technique will clearly help in simulating TC variability. It is less clear what benefits arise when the large-scale fields are derived from a GCM integration with its own biases. The latter process is the only means to generate scenarios/predictions of future TC activity.

For the PDI, although the ensemble means produce reasonable correlation coefficients, the mean values of the index are severely underpredicted. None of the simulations give a reasonable mean PDI value over the 28-year period, nor do they capture the observed upward trend. The main reason behind the failure to simulate realistic PDI values is the model's failure to produce realistic wind speeds in simulated tropical cyclones. Given

that the PDI scales with the cube of the wind speed, the failure to produce intense hurricanes greatly impacts the model's PDI.

In the previous section, using a smaller grid, we indicated that a realistic distribution of cyclogenesis events in the MDR is dependent on an adequate simulation of upstream AEWs. The correlation index between the number of hurricanes observed and simulated with the small LAM driven at the boundaries by GEM 2° is 0.08. However, if we only compare the interannual variability of TCs forming South of 25°N, the correlation index increases to 0.50, a value similar to the values obtained with the larger LAM integrations driven by GEM. The degradation when one includes TCs north of 25°N we believe occurs because the small LAM-GEM run fails to develop precursor TC systems sufficiently frequently off the coast of Africa as these storms are systematically too weak when entering into the LAM domain through the eastern boundary. As a result, too many of these systems propagate through the Atlantic without developing into TCs, only achieving TC strength north of 25°N.

In LAM-GEM, a larger percentage of the AEWs are strong enough to (correctly) form TCs south of 25°N, hence the LAM-GEM TC population is dominated (much more so than the small LAM-GEM) by TCs located south of 25°N. Since ENSO impacts on cyclogenesis equatorward and poleward of 25N are not necessarily the same (Camargo et al., 2007b), a dominance of TCs forming poleward of 25°N in the small LAM-GEM, caused by weak AEWs, leads to a significant degradation in the simulated interannual variability. A 0.50 correlation index suggests the impact of ENSO on TCs over the MDR (south of 25°N) is comparable in the small LAM-GEM to LAM-GEM, even if the absolute number of TCs in small LAM-GEM is biased low.

We also showed in the previous section that simulated cyclogenesis tends to occur in geographical locations with high climatological GPI values. In figure 2.10, we show the temporal correlation coefficient between GPI values at each model grid point and the total annual number of hurricanes . The simulated correlation is only shown for GVAR, but is equally well captured in the LAM-ERA integrations and somewhat less so in LAM-GEM runs. Clearly, GEM captures the relationship between large-scale fields (as expressed by GPI) and the number of TCs quite accurately.

A number of previous studies (Goldenberg and Shapiro, 1996 ; Gray et al., 1993) indicate that interannual variability of Atlantic TCs is correlated both with ENSO and Sahel rainfall variability. Here, we analyze these relationships as seen in observations and try to evaluate if similar relationships are captured in GEM.

2.6.1 Impact of ENSO

The El Niño Southern Oscillation is well-known to impact Atlantic tropical cyclone activity. Typically, El Niño events are associated with a decrease in activity while La Niña is associated with a higher than average activity. Increased convective activity in the East Pacific during El Niño years leads to increased upper troposphere westerlies across the Atlantic and therefore increased shear (Gray, 1984). Subsidence also increases in the Gulf of Mexico, leading to reduced relative humidity. Both changes are detrimental for TC formation, as can be understood through the GPI equation (Camargo et al., 2007b). Generally, reverse arguments hold for La Niña.

The Southern Oscillation Index (SOI) is the atmospheric manifestation of the coupled ENSO phenomenon and has been shown to be a good predictor of TC activity (Gray et al., 1993). Figure 2.11 shows the mean ASO SOI for the period 1979-2006 as simulated by GEM 2° and GVAR. Also shown is the SOI derived from ERA-40. Here, the SOI for the global 2° resolution, GVAR and ERA-40 is evaluated using the standard SOI formula[5] (Trenberth, 1984), but we use 1979-2006 as the base period to calculate anomalies. This measure of ENSO variability is well simulated by GEM and should produce a reasonable large-scale forcing of the tropical Atlantic from the Pacific. Correlation between individual SOI values and the different metrics of TC activity can be seen in table 2.4. LAM-ERA integrations perform very well, with a correlation coefficient between SOI and TCs similar to that seen between observed TCs and the ERA-40 SOI (0.44). GVAR also has a reasonable relationship while the LAM-GEM simulations are poor. An accurate SOI does not therefore appear to be a sufficient criterion to accurately force Atlantic TC variability from the Pacific and suggests problems in representing teleconnections from the Pacific into the Atlantic between GEM 2° and LAM-GEM. These problems may arise from the fixed boundary condition treatment in the LAM simulations compared to the 2-way smooth nesting in GVAR. A second possibility is that

5. $\text{SOI} = \frac{\text{Standardized MSLP Tahiti} - \text{Standardized MSLP Darwin}}{\text{Monthly Standard Deviation}}$

due to the mode of stretching in GEM, the tropical Pacific in GVAR has a longitudinal resolution of 2° but a latitudinal resolution of 0.3°. This increased resolution may help in simulating the tropical wave guide and associated teleconnections.

Recently, Kim et al. (2009) have investigated the relationship between ENSO and Atlantic TCs for the period 1950-2006. They identified two different El Niño "flavors", each found to impact Atlantic TC activity differently than the other. In the first instance, maximum SST warming occurs in the East Pacific in the Niño 3 region (EPW) while in the second case, referred to as Modoki El Niño (Ashok et al., 2007), the maximum warming occurs in the Central Pacific in the Niño 4 region (CPW). All East/Central Pacific cooling are considered La Niña events (EPC). For more information we refer to figure 1 in Kim et al. (2009).

Even though we evaluate a shorter time period, it is of interest to see if/how GEM can reproduce the different impacts on Atlantic TC activity associated with the different El Niño/La Niña events. For this purpose, we have evaluated composites of track density anomalies for the GVAR, the LAM-ERA ensemble and LAM-GEM ensembles associated with EPC events (1985, 1988, 1995, 1998, 1999), CPW events (1991, 1994, 2002, 2004) and EPW events (1982, 1987, 1997) and compared them with the equivalent track density anomalies from observations. The track density anomalies are calculated by subtracting the mean track density from the mean EPC, EPW and CPW track density for individual simulations. In figure 2.12, we only show results for the GVAR integration, with LAM-ERA integrations yielding similar results while LAM-GEM track anomalies are somewhat poorer. We believe these differences are likely also due to the higher resolution of GVAR in the tropical Pacific compared to GEM 2°.

Even though the period we analyze is somewhat shorter than Kim et al. (2009), the general patterns they highlighted are still apparent in the observations : i) a general decrease in TC activity over the entire Atlantic during EPW episodes, ii) a general increase in activity during EPC episodes and iii) an increase in activity in the western Atlantic and decrease in the central/eastern part of the Atlantic for CPW events. The detailed differences between our observed results and theirs likely arise from the fact their track records extend from 1950 to 2006 while we cover only the 1979-2006 period.

The GVAR simulation successfully reproduces the general reduction in activity over the entire Atlantic during EPW (figure 2.12), except over the Gulf of Mexico. This is not entirely surprising since TC activity is underestimated across all years in this region. The same integration shows a general increase in TC activity during EPC events similar to observations. However, there is some geographical shift in the region/intensity where the positive track density anomalies are simulated compared to observed : GVAR places the maximum increase east of the American coast and near the Florida panhandle while the observed maximum is more over the Gulf of Mexico. Difficulties in reproducing the maximum response over the Gulf is likely, at least in part, tied to the systematic bias in relative humidiy in the mid-troposphere in this region. Both observations and GVAR show a maximum over the MDR. For CPW events, the model manages to reproduce the decrease in activity in the central Atlantic, but fails to show an increase in the Western part of the basin.

In order to understand the origin of these changes, we look at the changes in the GPI during these three different types of events. Figure 2.13 shows changes in GPI between the climatological mean and EPW, CPW and EPC years in the reanalysis and the GVAR integration. During EPW events, the analysed GPI is reduced over the entire Atlantic basin, leading to a general decrease in TC activity. This reduction in GPI is generally well reproduced over the MDR in the GVAR integration, except for an area just off the coast of Africa. However, the GPI in this area tends to anti-correlate with TC activity in the simulations (figure 2.10). In GVAR there also appears to be a somewhat unrealistic increase in GPI in the subtropical Atlantic, caused by an unrealistic increase in relative humidity and low-level vorticity.

For CPW events, patterns of change in the GPI values between GVAR and reanalysis appear similar, except for the analysed increase in GPI in the Gulf of Mexico. This increase results from a combination of increasing mid-tropospheric humidity and low-level vorticity as well as a drop in vertical wind shear. The absence of this positive anomaly in the GVAR results probably explains why it fails to simulate an increase in track density in the Western part of the basin during CPW events. A general decrease in GPI over the MDR will tend to suppress cyclogenesis in that region and lead to fewer storms propagating westward in the Atlantic. Storms originating from AEWs would be most affected by this change in large-scale field conditions. This appears consistent with the reduction in track density in the mid-Atlantic, both observed and simulated in the

analysis and GVAR results.

Finally, both reanalysis and integrations show similar patterns in GPI changes during EPC events : a general increase in GPI over the entire MDR and a slight decrease in the subtropics. An increase in the GPI over the MDR will contribute to increased TC activity again consistent with the positive track anomaly observed and simulated. The absence of an increase in GPI over the Gulf of Mexico, north of $25°N$, in GVAR probably contributes to the smaller increase in track anomalies over that same region, compared to observations.

Overall, changes in GPI, both observed/analysed and simulated, help explain the changes in track density seen in the EPW, CPW and EPC events. As mentioned earlier, the LAM-GEM response to the three ENSO phases is not as accurate as GVAR. This is either due to the higher resolution of the GVAR model (latitudinally) in the equatorial Pacific or the Global variable resolution approach allows for a better propagation of the teleconnective signal from the Pacific into the Atlantic than the fixed boundary condition treatment in LAM-GEM. Further investigation of this is deferred to a later study. The poor representation of ENSO forcing over the Atlantic probably also contributes to the poorer interannual variability simulated by this configuration of GEM.

2.6.2 Impact of Sahel Rainfall

As shown above, failure to properly reproduce ENSO's teleconnections over the Atlantic will directly affect large-scale fields conducive to cyclogenesis and impact simulated TC activity. Goldenberg and Shapiro (1996) showed that Sahel rainfall has a stronger correlation with MDR wind shear than eastern Pacific SSTs, and, even though Aiyyer and Thorncroft (2006) suggest that the influence of Sahel rainfall on MDR TC activity has been decreasing in recent years, failure to properly reproduce the influence of Sahel rainfall on MDR vertical wind shear, or changes therein, could lead to a degradation in simulated TC activity on interannual timescales. Furthermore, it is well established that AEWs variability (intensity and frequency) act as important precursors for downstream TC development.

Figure 2.14 shows a time series of Sahel rainfall anomalies, defined as the ASO rainfall

difference with respect to climatology within the area bordered by $10°N$, $17.5°N$, $16°W$ and $10°E$, for observations, derived from the Global Precipitation Climatology Project (GPCP ; Adler et al., 2003) and individuals simulations. The temporal correlation index for Sahel rainfall between the two LAM-ERA simulations is 0.90 and 0.85 between the two LAM-GEM simulations. The only other significant correlations that could be found were between GPCP precipitation and the two LAM-ERA simulations (0.68, 0.65). This seems to suggest that the set-up used has a large impact on Sahel precipitation, or more precisely how SST distribution influences Sahel precipitation. Everything else remaining equal (that is, the relationship between Sahel rainfall and MDR TC activity), failure to properly simulate Sahel rainfall variability will lead to a degradation in simulated TC interannual variability.

Correlation between Sahel precipitation and GPI over the Atlantic are shown in figure 2.15. The differences between GVAR and LAM-GEM are striking : high correlations extend all across the MDR in GVAR but are negligible in the LAM-GEM configuration. The difference between GVAR and LAM-GEM correlations comes mostly, but not exclusively, from the wind shear term. The failure to simulate the relationship between MDR vertical wind shear and Sahel rainfall should then degrade the relationship between Sahel precipitation and MDR TC activity. Table 2.5 shows the correlation coefficients between Sahel rainfall anomalies and the total number of tropical cyclones and hurricanes forming South of $25°N$, these storms being those most likely to originate from the MDR. Indeed, there does not appear to be any link between Sahel precipitation and simulated TC activity in the LAM-GEM configuration. Conversely, in a case when the correlation between Sahel rainfall and GPI (and wind shear) is higher than what is observed over large portions of the MDR, as in GVAR, the correlation between Sahel rainfall anomalies and TC activity tends to be overestimated. Interestingly, correlation coefficients for the two series in the LAM-ERA simulations are similar to the observed correlation coefficients and similar to Aiyyer and Thorncroft (2006) observed 21-year segment running correlation (TC only) for the equivalent period.

In figure 2.16, we compare the mean ASO 2003 vertical profile of $\frac{v'^2}{2}$ at $10°N$ and $15°W$ (essentially tracking AEWs as they leave the coast of Africa) for six different integrations, where v' is the the 2.5-6-day bandpass-filtered meridional wind. The bandpass filter was designed such that it isolates the influence of AEWs, which are known to modulate Sahel rainfall (Reed et al., 1977). Higher meridional kinetic energy at

$925 - 850\ hPa$ is an indication of higher AEW activity (Thorncroft and Hodges, 2001), and, in this case, of both stronger and of a larger number of AEWs. From this figure, it seems clear that the global low resolution simulation does a very poor job of simulating AEWs, consistent with what was presented earlier. Also, both LAM-GEM runs appear to simulate weaker AEW activity in comparison to LAM-ERA and GVAR, despite the fact that 2003 shows the strongest and second strongest positive rainfall anomaly over the Sahel region in the two LAM-GEM simulations. Comparison with figure 4 in Thorncroft and Hodges (2001) indicates that LAM-GEM is more typical of a weak-activity year in regard to AEW, while LAM-ERA and GVAR are more reminiscent of a strong-activity year. This suggests that, due to weak AEW activity, the Sahel rain link to downstream wind shear, GPI and TC activity is lost in the LAM-GEM integrations.

The weaker AEWs in LAM-GEM appears to result from anomalous convective activity in the Gulf of Guinea in the GEM 2° simulation. This convection, absent in GVAR and ERA-40 reanalysis, induces anomalous upper-level meridional winds detrimental to convective activity over the Southern part of West Africa. This anomalous convection over the Gulf of Guinea is not unique to GEM, as it was reported that several GCMs fail to move the summer rain from the Gulf onto land (Christensen et al., 2007).

In section 2.5 we mentioned that convection over the South American continent was too strong in GEM compared to reanalysis, which increased vertical wind shear and reduced TC activity over the Caribbean. It is worth noting that strong correlations were found between convective activity (as represented by vertical velocity at 700 hPa) over the Northern part of the Amazon and GPI, through changes in vertical wind shear, over part of the Atlantic in LAM-GEM and GVAR. Similarly, correlations between Amazon convective activity and hurricane numbers were found to be between 0.4 (LAM-GEM) and 0.55 (GVAR). No such correlation are found in reanalysis/observations. This suggests that, beside the misrepresentation of the link between ENSO and AEWs (Sahel rainfall) with TC activity, an erroneously simulated influence of South American convection onto Carribean TC activity, not seen in observations, can degrade the representation of TC interannual variability in models.

2.7 Conclusions

By comparing different integrations performed with a range of configurations of GEM, at various resolutions (2°, 1°, 0.3°), we have shown an increase in the realism of simulated tropical cyclones and improvements in the number, geographical distribution and overall track density of theses storms in the Atlantic. Although the improvement in simulated TC activity was accompanied by a more realistic representation of the GPI, which represents the large-scale fields favorable to cyclogenesis, in the higher resolution simulation, the improvement in TC dynamics with increased resolution appears to be the main reason behind the increase in simulated activity.

We then compared different high-resolution (0.3°) simulations performed using two different dynamical downscaling techniques : one which uses a limited-area domain and one, a global-variable resolution domain. For the limited area domain, we used different lateral boundary conditions (ERA-40 reanalysis and GEM 2°), in order to understand the importance of accurately simulating processes located outside the tropical Atlantic on Atlantic TC activity. All these simulations show a relatively realistic distribution of TCs and intra-annual distribution, with maximum activity in September. None of the integrations produced storms stronger, based on the maximum surface wind speed, than category 1. However, storm central pressures typical of up to category 3 were present, suggesting a deficiency in the simulation of the TC near-surface momentum budget in GEM.

The high-resolution simulations had some level of skill in representing observed inter-annual variability over the recent past. Although, the (ensemble of) LAM driven by ERA-40 displayed the best correlation with observed activity, the other ensemble (GVAR and LAM-GEM) still managed to capture some of the observed interannual variability. This is in part caused by their capacity to reproduce ENSO teleconnections over the Atlantic. Finally, Sahel rainfall, through AEW activity, impacted TC activity differently in the different integrations. In GVAR and LAM-ERA, AEWs allowed convective activity over the Sahel region to somewhat impact, through changes in MDR vertical wind shear, Atlantic TC activity. In LAM-GEM, due to weaker AEWs, this link appears broken. It should be mentioned that the downscaling technique itself appears to have a strong impact on simulated Sahel rainfall. Since none of our simulations managed to capture the recent inter-annual variability in Sahel precipitation, linking it with TC activity will not

necessarily lead to better interannual variability. Finally, using a smaller domain, where AEW activity was essentially a boundary condition prescribed by the GEM-Global 2 run, we showed that an accurate simulation of AEW frequency/intensity was essential for simulating TC activity in the MDR.

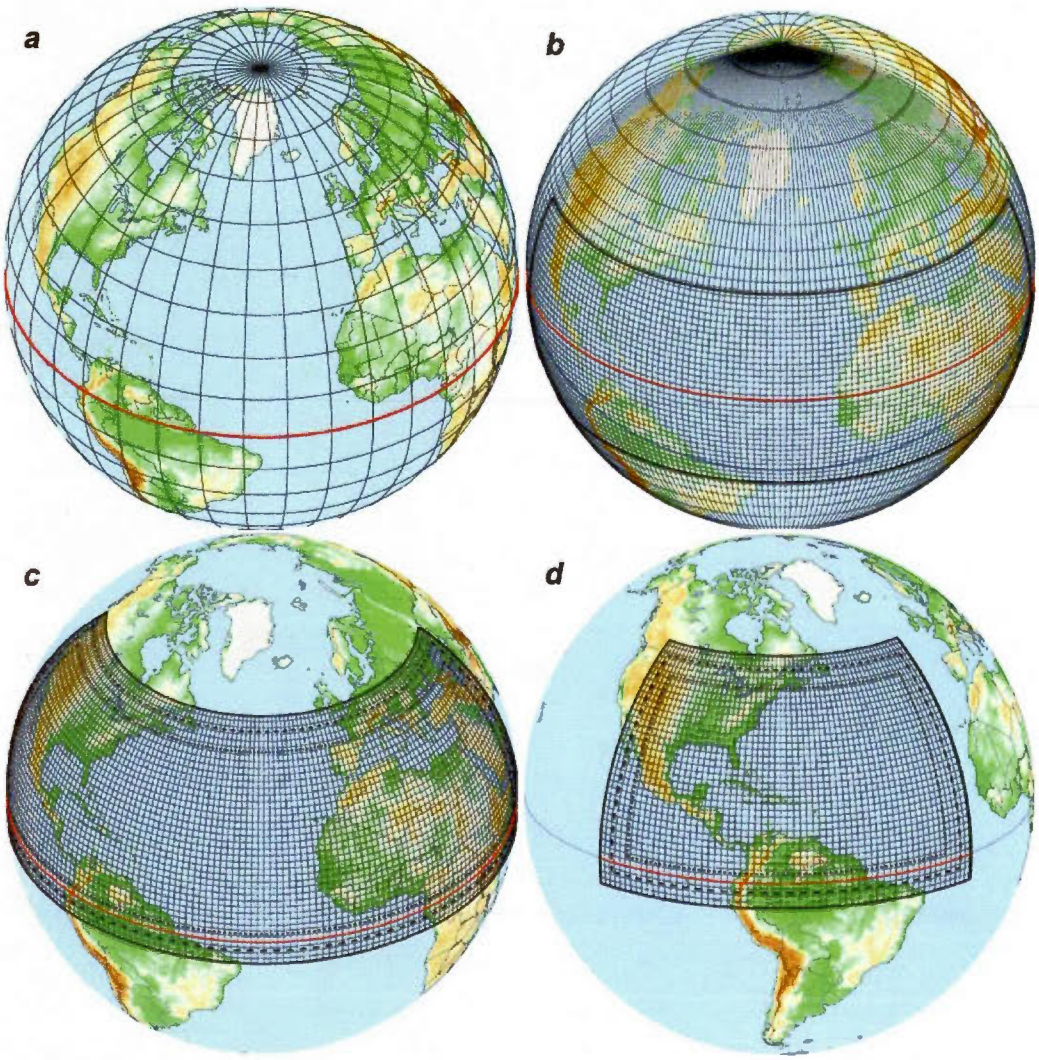

Figure 2.1 Different model configurations used in this study : a) global, uniform domain (2° and 1°), b) global, variable resolution domain (from 0.3° to 2°) and c) d) two uniform, limited-area domains (0.3°). Only every 5 grid point is plotted in the meshes. For GVAR, the thick black line separates the high-resolution area from the increasingly low resolution area. For the LAM, the area between the dash lines is the blending zone, while the area between the long dash and the thick black line is the pilot area. The red line is the grid equator, while the blue line is the true equator.

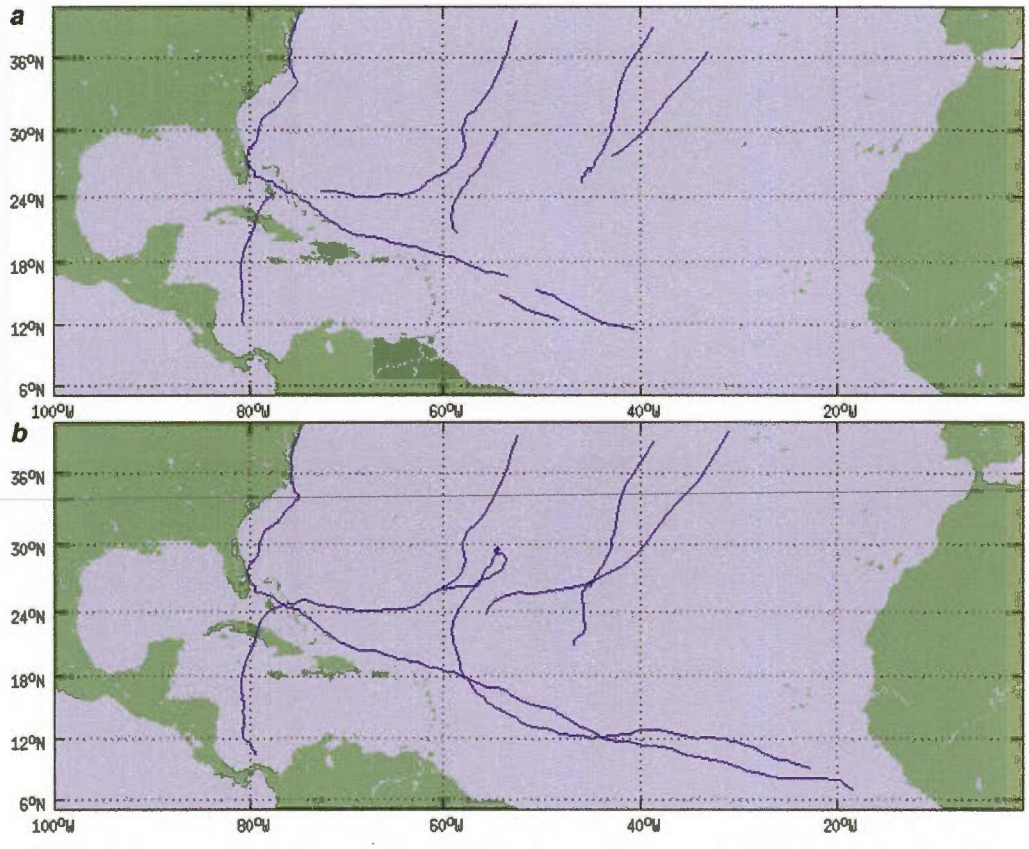

Figure 2.2 TC tracks detected for the same hurricane season (1997) by a) the first set of criteria, and b) the two sets of criteria.

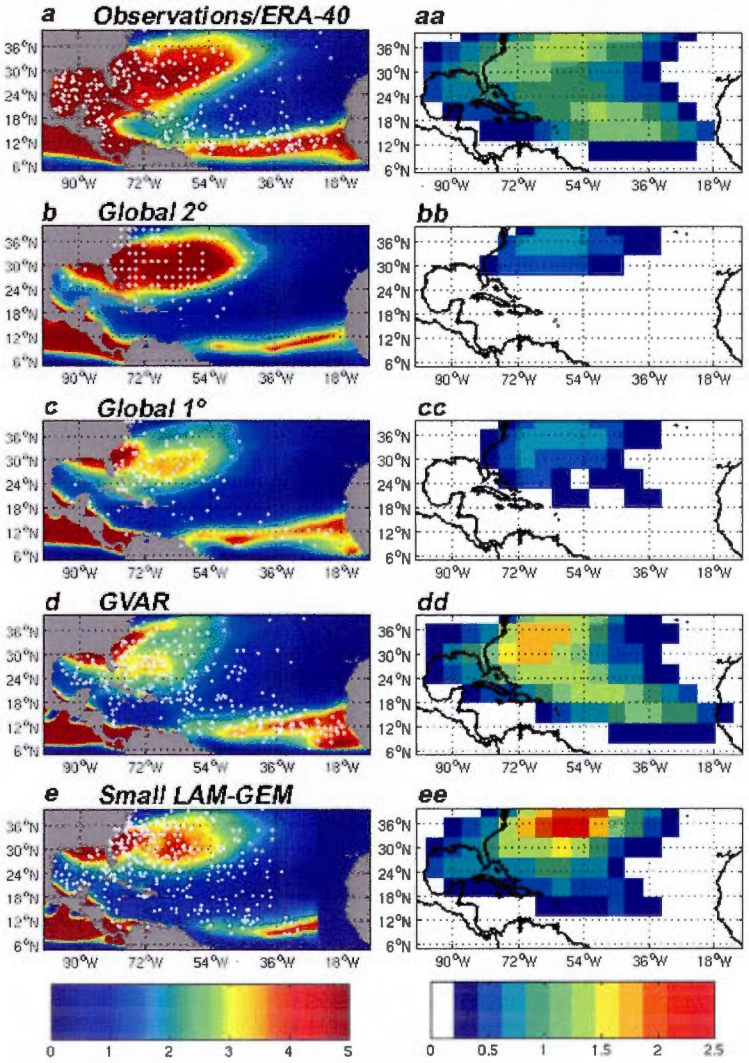

Figure 2.3 Left column : Seasonal (ASO) GPI for a) ERA-40 (1979-2001), b) GEM 2°, c) GEM 1°, d) Global-Variable resolution simulation, and e) small LAM driven by GEM 2°. The dots indicate cyclogenesis locations. Tropical cyclones forming in the Eastern Pacific are not shown. Right column : Track density for the 1979-2006 period for aa) observations (HURDAT), bb) GEM 2°, cc) GEM 1°, dd) Global-Variable resolution simulation, and ee) small LAM driven by GEM 2°. Units are number of TCs per 5° × 5° grid box per year.

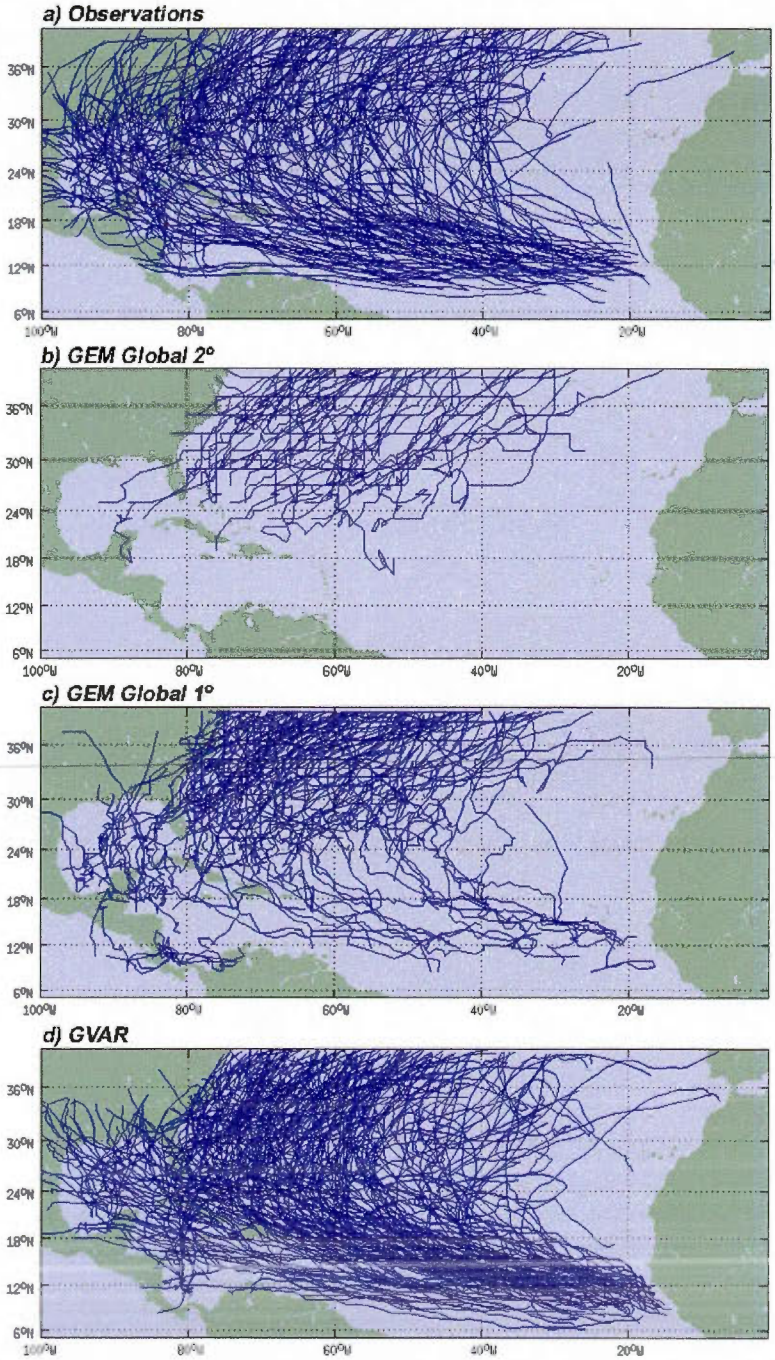

Figure 2.4 Climatology of June-November TC tracks for the period 1979-2006 for a) observations, b) GEM Global 2°, c) GEM Global 1° and d) GVAR.

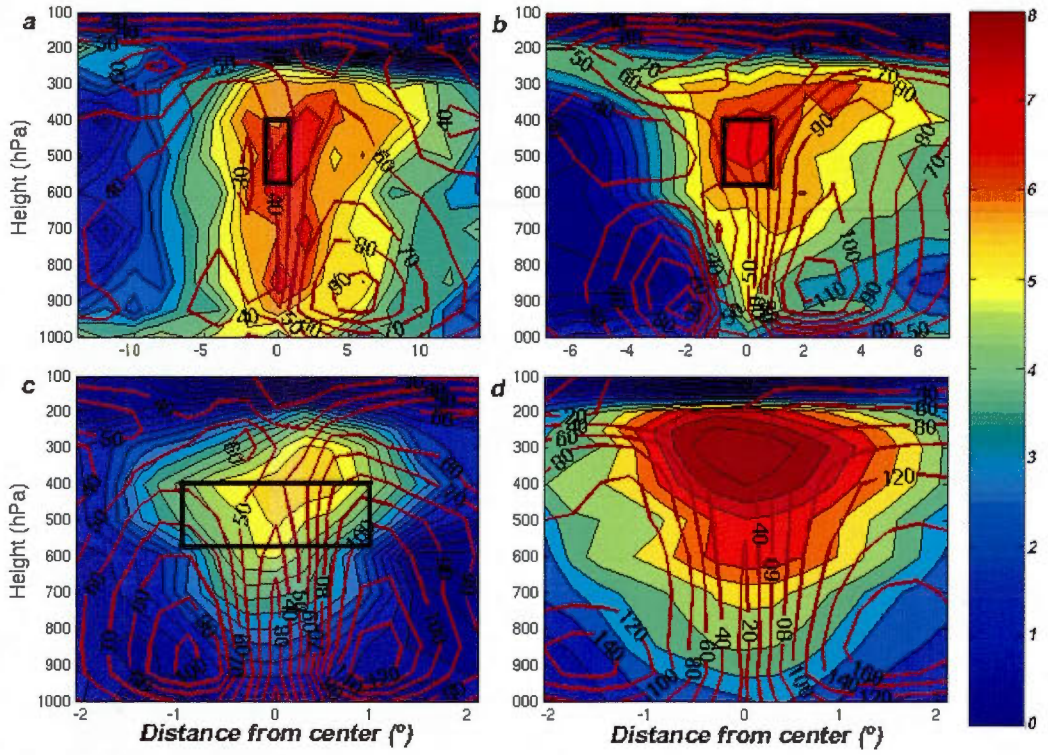

Figure 2.5 Composites of vertical profiles for horizontal wind and temperature anomaly for three tropical cyclones simulated at a) 2°, b) 1° and c) d) 0.3°. a), b) and c) show storms in the $982 - 998\ hPa$ range while d) represents storms in the $950 - 960\ hPa$ range. Note the change in the horizontal scale between storms. The black box is the same dimension in all three figures (2° horizontal width). Winds are in $km\ h^{-1}$, temperature in $°C$.

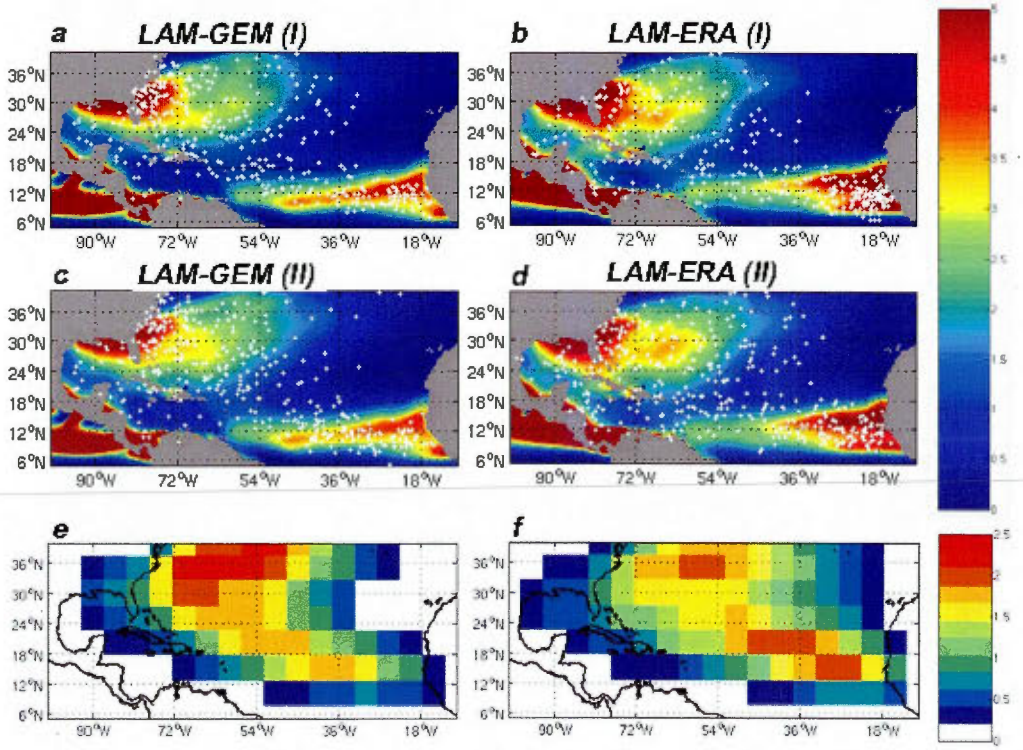

Figure 2.6 Left column : a) c) Seasonal (ASO) GPI, and e) ensemble mean track density for LAM driven by GEM 2° ; Right column : b) d) Seasonal (ASO) GPI and f) ensemble mean track density for LAM driven by ERA-40. The dots indicate cyclogenesis locations. Tropical cyclones forming in the Eastern Pacific are not shown. Units for track density are number of TCs per 5° × 5° grid box per year.

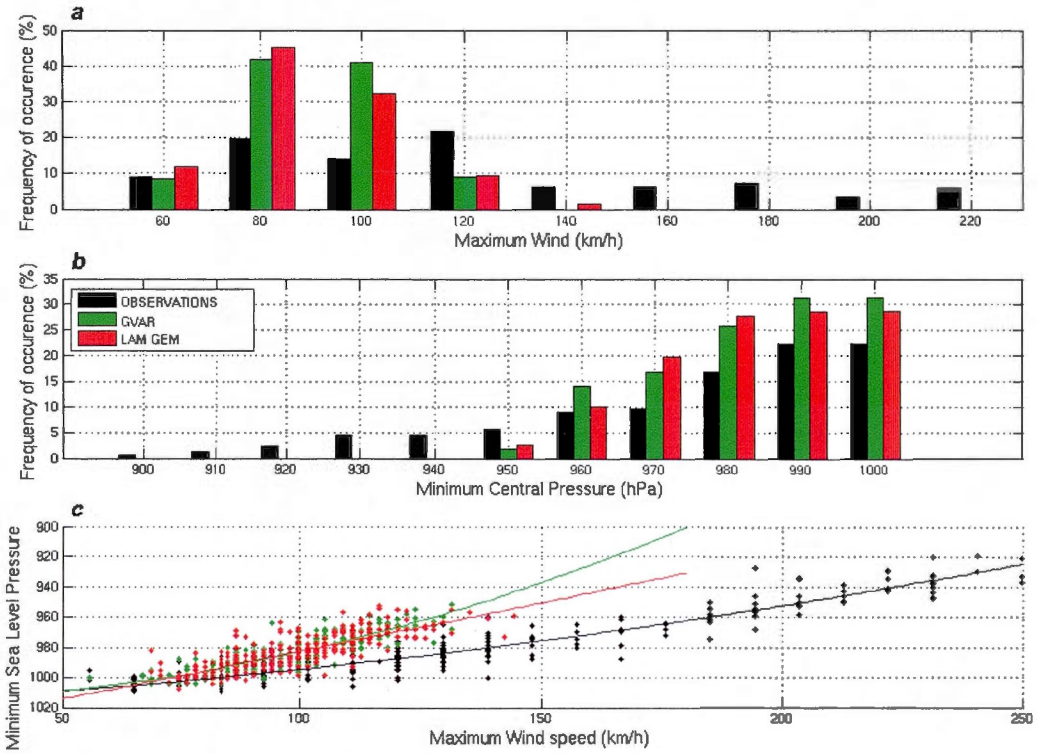

Figure 2.7 a) Maximum wind speed distribution, b) minimum central pressure distribution and c) relation between maximum wind and minimum central pressure, for observations and two high-resolution simulations for the 1979-2006 period.

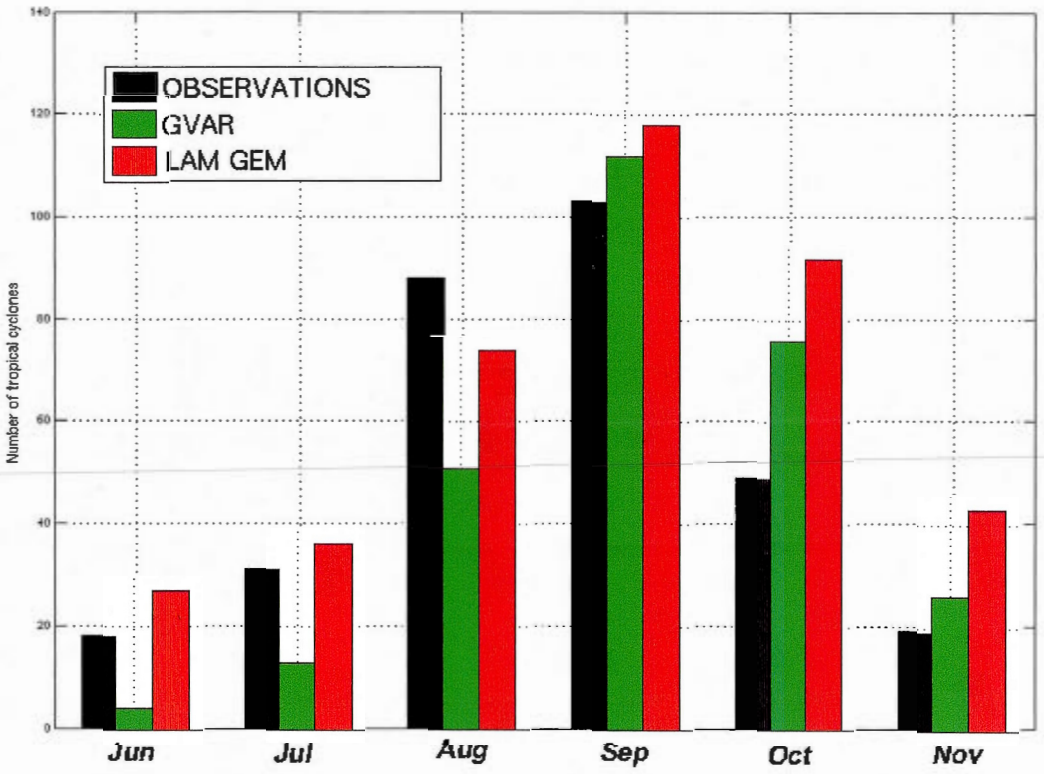

Figure 2.8 Monthly distribution of tropical cyclones for observations and two high-resolution simulations for the 1979-2006 period.

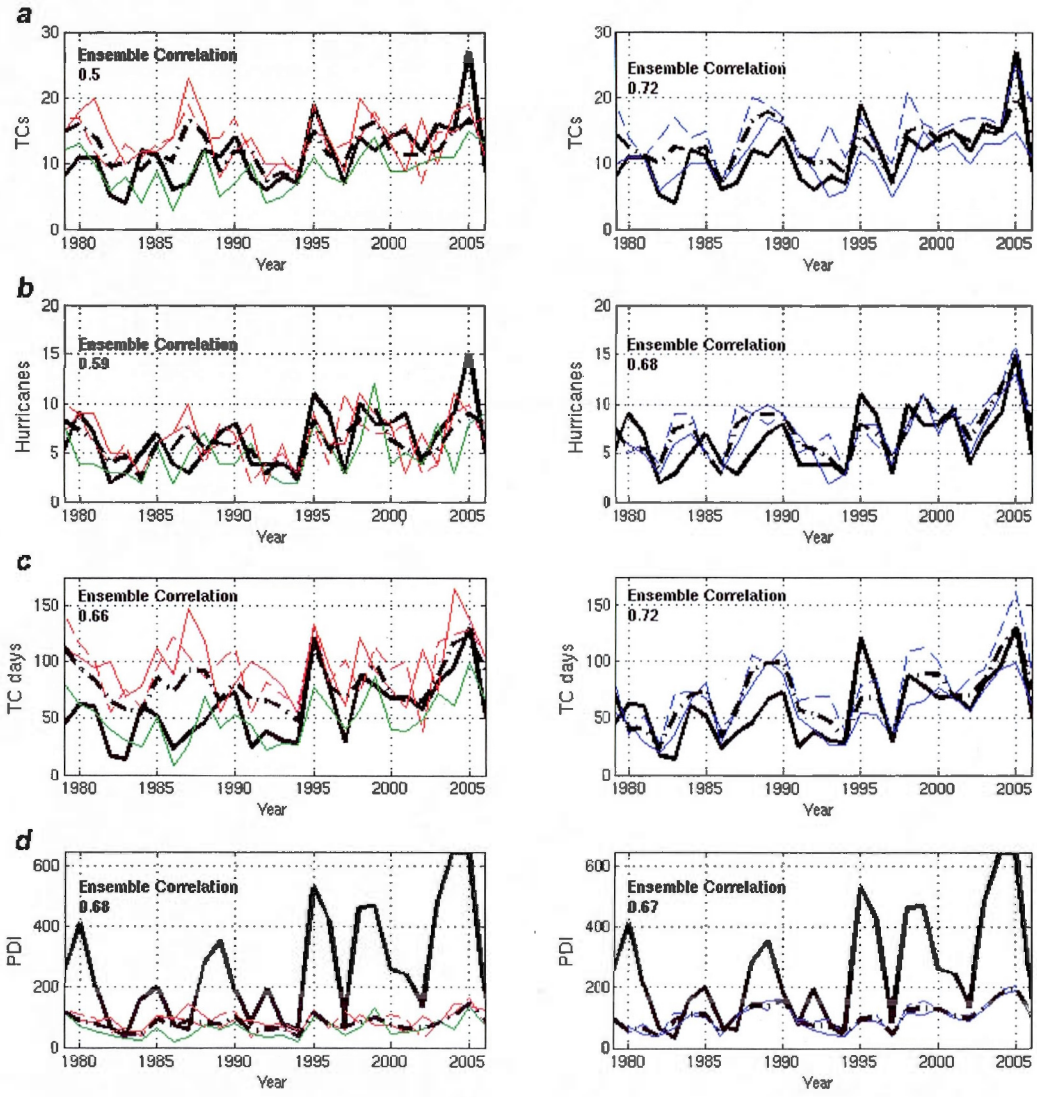

Figure 2.9 Interannual variability in a) TCs, b) hurricanes, c) TC days and d) PDI ($10^9 m^3 s^{-2}$) for the June-November, 1979-2006 period. The left column shows observations (black solid) and individual simulations, LAM-GEM (red solid and dash), GVAR (green) as well as GVAR and LAM-GEM ensemble mean (black dash). The right column shows observations (black solid) and individual simulations, LAM-ERA (blue solid and dash) as well as LAM-ERA ensemble mean (black dash). For each picture, correlation between the ensemble mean and observations has been reported

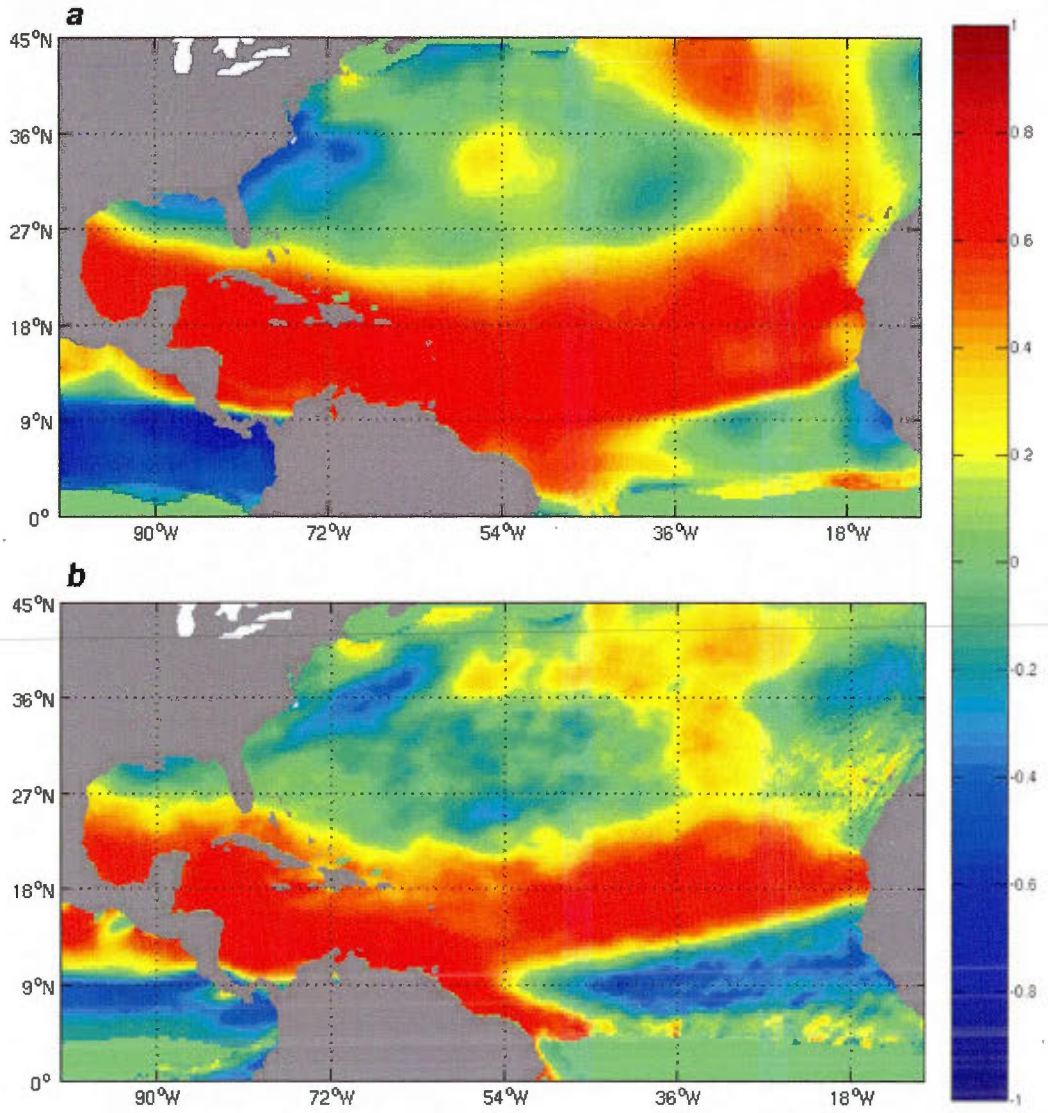

Figure 2.10 Temporal correlation between GPI values at individual grid points and annual number of hurricanes for a) ERA-40/observations and b) GVAR simulation.

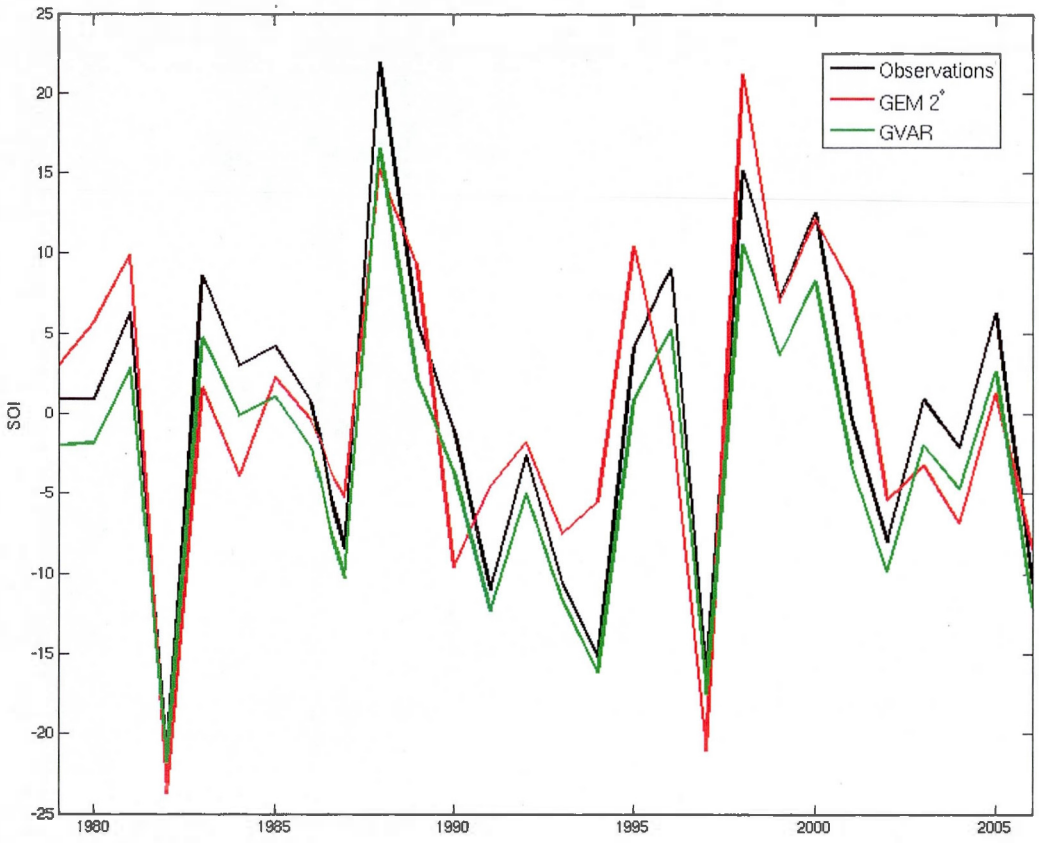

Figure 2.11 Mean ASO Southern Oscillation Index measured and simulated by two different integrations.

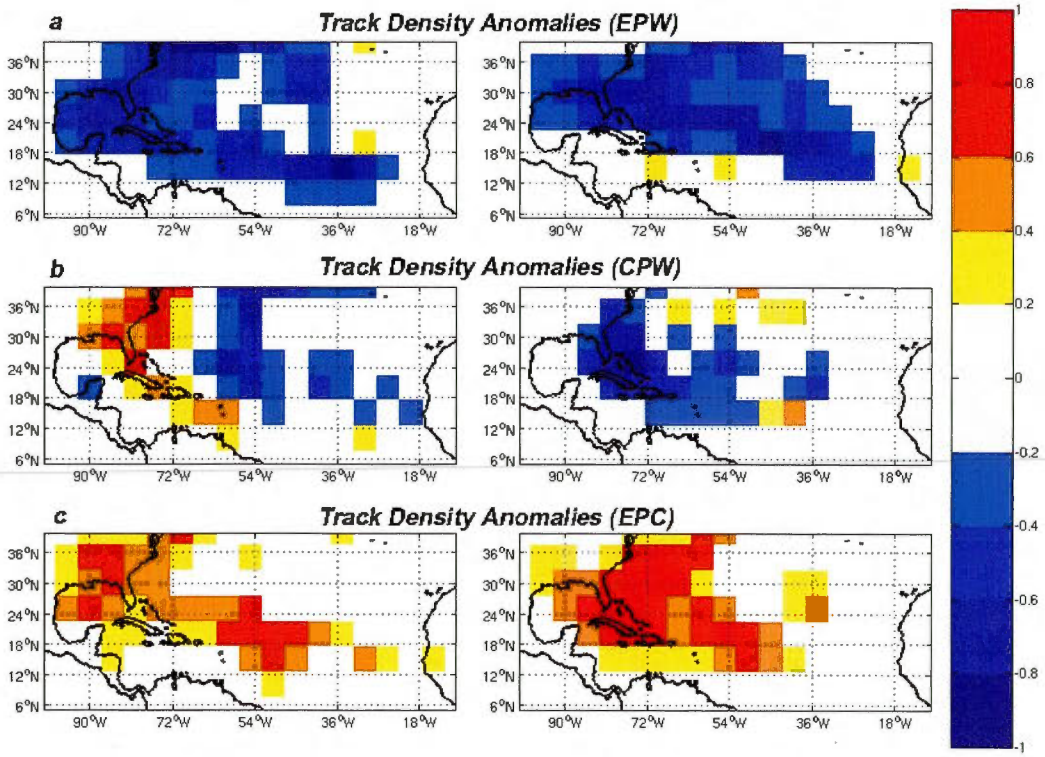

Figure 2.12 Composites of track density anomalies during a) EPW events, b) CPW events and c) EPC events for observations (left column) and for the GVAR simulation (right column) for the 1979-2006, ASO period. Units are number of TCs per 5° × 5° grid box per year.

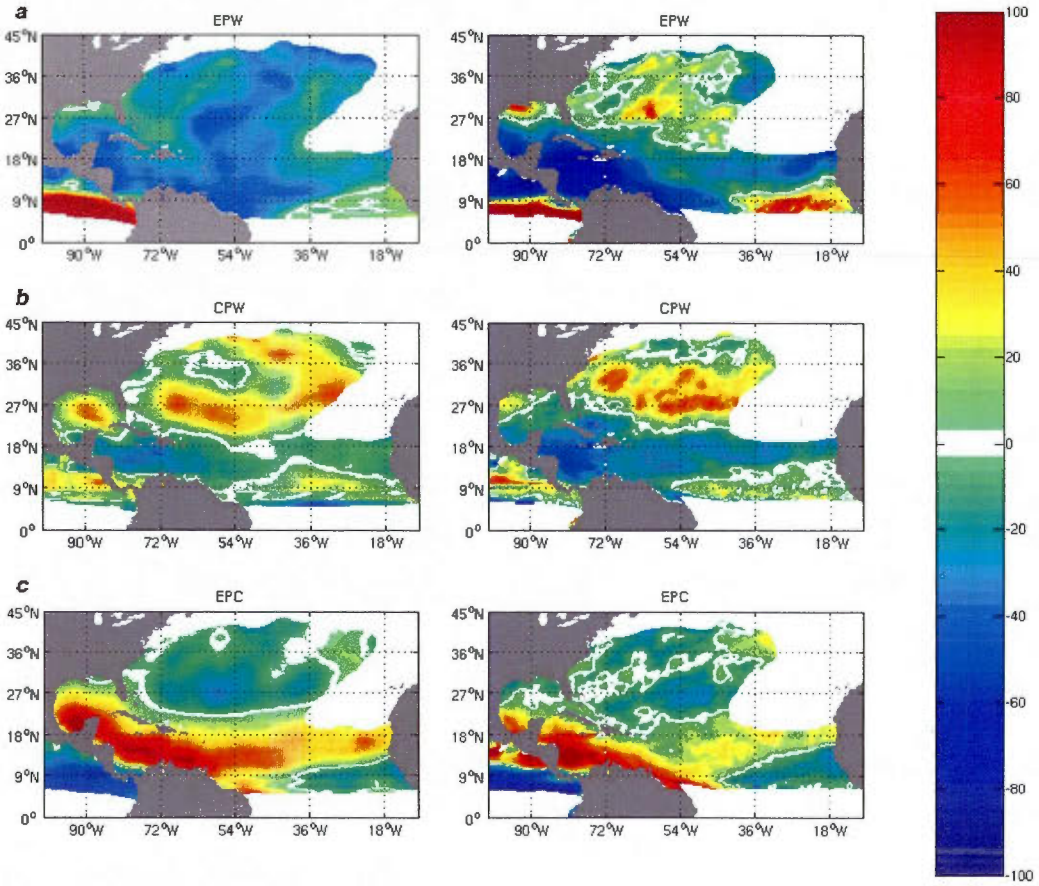

Figure 2.13 Percentage change in GPI values between climatological mean for a) EPW years, b) CPW years and c) EPC years, for ERA-40 (left column) and for the GVAR simulation (right column) for the 1979-2006, ASO period. Only areas for which climatological values are greater than 0.5 GPI unit are evaluated.

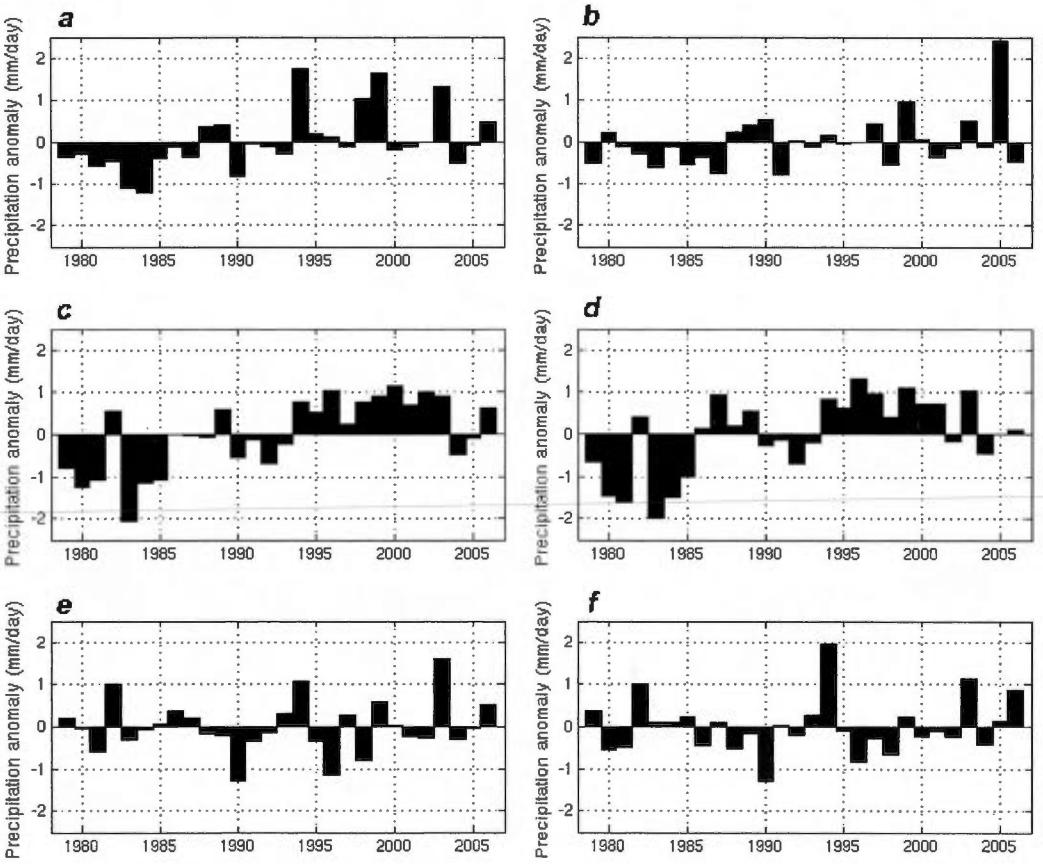

Figure 2.14 ASO Sahel precipitation anomalies compared to climatological mean for a) observations (GPCP), b) GVAR, c) d) LAM-ERA and e) f) LAM-GEM.

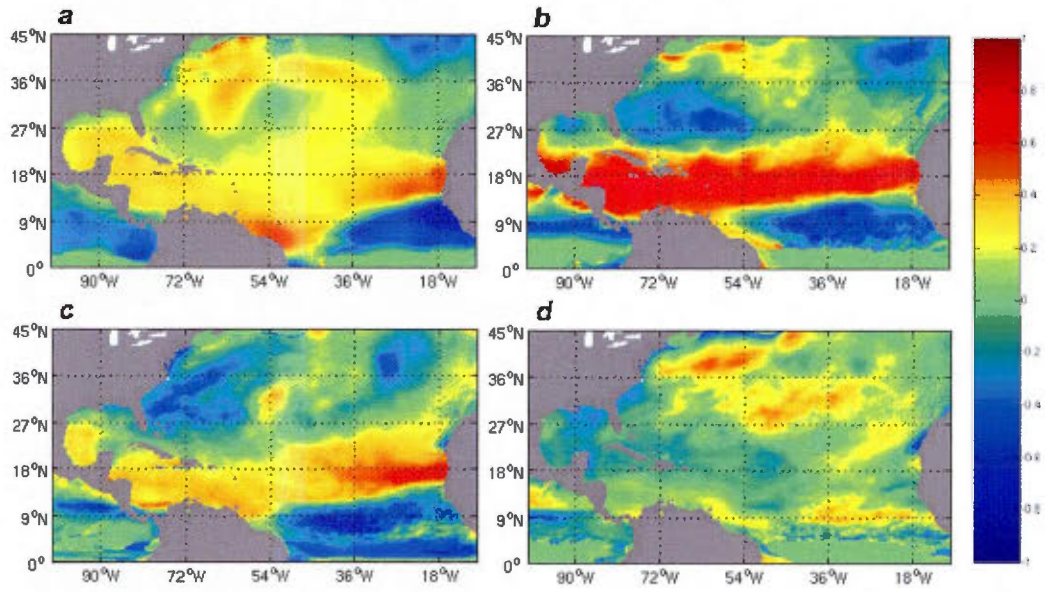

Figure 2.15 Maps of correlations between Sahel precipitation (ASO) and GPI (ASO) for a) GPCP observations/ERA-40 (GPI), b) GVAR, c) LAM-ERA and d) LAM-GEM.

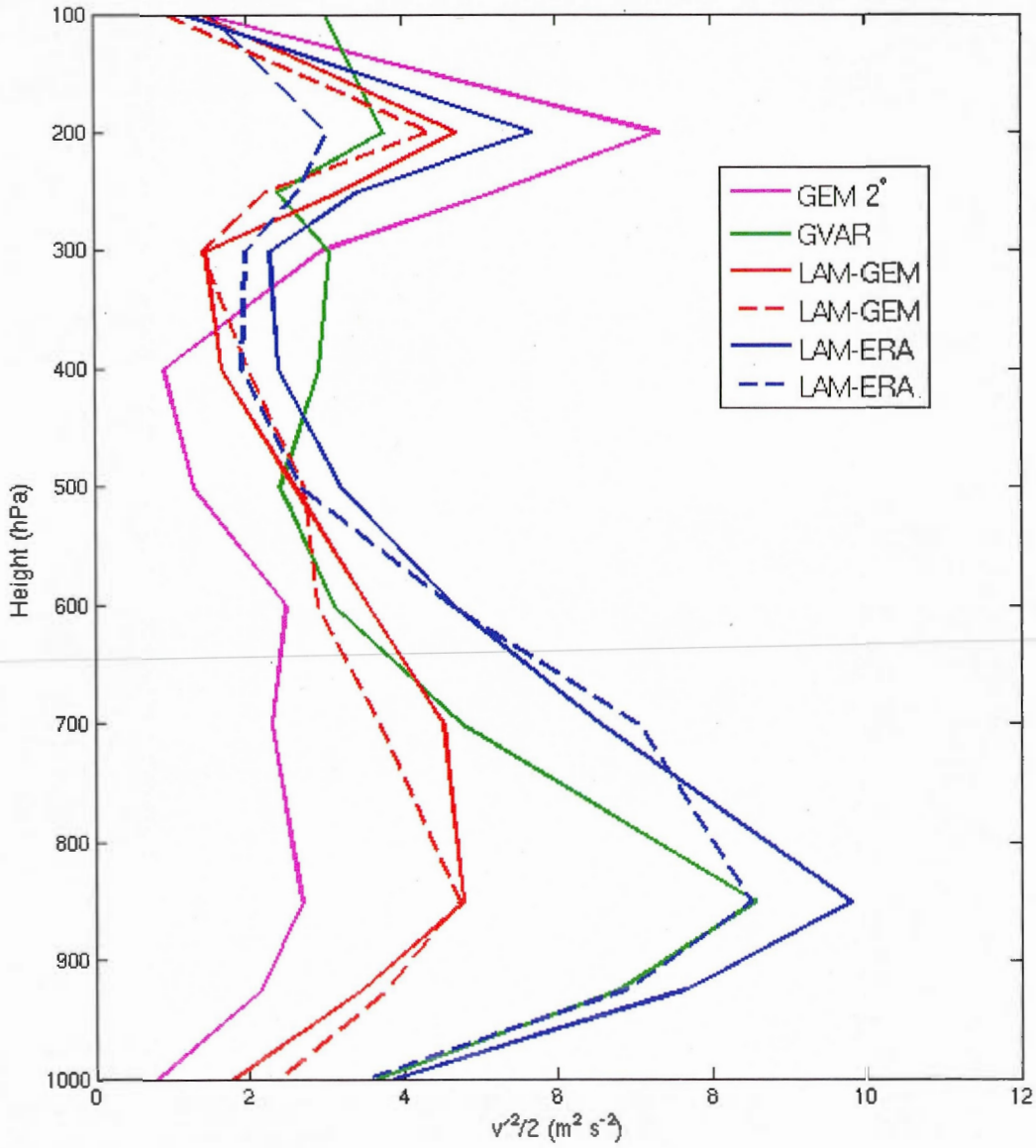

Figure 2.16 Vertical profile of the ASO 2003 $\frac{v'^2}{2}$ (where v' is the 2.5-6-day bandpass-filtered meridional wind) for 6 different simulations at location 10N, 15W.

Tableau 2.1 Total number of tropical cyclones detected and simulated, for the period June-November, 1979-2006.

	TCs
Observations	314
Global, 2°	63
Global, 1°	110
GVAR	282
Small LAM	342
LAM-GEM (1)	390
LAM-GEM (2)	385
LAM-ERA (1)	358
LAM-ERA (2)	397

Tableau 2.2 Correlation index between observed and simulated indices used to evaluate GEM interannual variability.

	TCs	Hurricanes	TC Days	PDI
LAM-GEM (1)	0.25	0.46	0.32	0.34
LAM-GEM (2)	0.44	0.42	0.50	0.51
GVAR	0.54	0.44	0.69	0.72
Ensemble	**0.50**	**0.58**	**0.67**	**0.66**
LAM-ERA (1)	0.64	0.71	0.65	0.63
LAM-ERA (2)	0.61	0.58	0.72	0.66
Ensemble	**0.72**	**0.68**	**0.72**	**0.67**

Tableau 2.3 Trends in the different metrics used to evaluate GEM interannual variability.

	TCs (TC/year)	Hurricanes (Hurricane/year)	TC Days (TC days/year)	PDI $((10^9 m^3 s^{-2})$/year)
Observations	0.31	0.15	1.8	10
LAM-GEM (1)	0.01	0.06	0.2	1
LAM-GEM (2)	0.07	0.04	0.3	1
GVAR	0.13	0.10	0.8	1
LAM-ERA (1)	0.10	0.15	1.1	2
LAM-ERA (2)	0.15	0.16	2.1	3

Tableau 2.4 Correlation index between SOI and different metrics used to evaluate GEM interannual variability.

	TCs	Hurricanes	TC Days
Observations	0.44	0.54	0.47
LAM-ERA (1)	0.49	0.48	0.48
LAM-ERA (2)	0.42	0.41	0.54
LAM-GEM (1)	0.20	0.27	0.02
LAM-GEM (2)	-0.29	0.18	0.24
GVAR	0.30	0.33	0.36

Tableau 2.5 Correlation index between Sahel precipitation and tropical cyclone and hurricane numbers.

	TCs	Hurricanes
Observations	0.26	0.34
LAM-ERA (1)	0.25	0.25
LAM-ERA (2)	0.27	0.36
LAM-GEM (1)	-0.17	-0.10
LAM-GEM (2)	0.08	-0.08
GVAR	0.41	0.43

CHAPITRE III

UNDERSTANDING AND SIMULATING THE LINK BETWEEN AFRICAN EASTERLY WAVES AND ATLANTIC TROPICAL CYCLONES USING A REGIONAL CLIMATE MODEL : THE ROLE OF DOMAIN SIZE AND LATERAL BOUNDARY CONDITIONS.

Abstract

Using a suite of lateral boundary conditions, we investigate the impact of domain size and boundary conditions on the Atlantic tropical cyclone and African Easterly Wave activity simulated by a regional climate model for the 1979-2006 period. Irrespective of boundary conditions, simulations closest to observed climatology are obtained using a domain covering both the entire tropical Atlantic and northern African region. There is a clear degradation when the high-resolution model domain is diminished to cover only part of the African continent or only the tropical Atlantic, in part due to poorer representation of African easterly waves in the low-resolution pilot simulation. Furthermore, reducing the size of the domain increases the influence of biases in the boundary data, which for domains covering only the tropical Atlantic, have a large impact on TC activity. Beyond a certain threshold of mean African easterly wave intensity, the large-scale Atlantic atmospheric environment becomes the primary control on simulated TC activity, as evidenced by changes in a genesis potential index.

All ERA40-driven integrations manage to capture the observed interannual variability and to reproduce the upward trend in tropical cyclone activity observed during that period. When driven by low-resolution GEM integrations, the regional climate model captures interannual variability (albeit with lower correlation coefficients) only if tropical cyclones form in sufficient numbers in the main development region. However, all GEM-driven integrations fail to capture the upward trend in Atlantic tropical cyclone activity. In most integrations, variations in Atlantic tropical cyclone activity appear

uncorrelated with variation in African easterly wave activity and Sahel rainfall.

3.1 Introduction

Due to an increase in computing power, climate models can now be run at sufficiently high resolution to resolve features closely resembling tropical cyclones (TCs). Following this, several attempts have been made in recent years, with relative success, to reproduce observed TC activity, particularly in the Atlantic. For example, Knutson et al. (2007), Larow et al. (2008), Murakami and Wang (2010) and Caron et al. (2010), using different global/regional climate models (GCMs; RCMs) with resolution <100 km covering relatively similar periods (~25 years) over the recent past, managed to produce reasonable numbers of Atlantic TCs, with correlation coefficients of 0.74, 0.78, 0.46 and 0.72, respectively. Zhao et al. (2009), examining solely hurricane-strength storms, found a correlation coefficient of 0.83. Observed variability in TC activity can be captured by the models because storm activity is dependant on the underlying sea surface temperature (SST) and induced large-scale fields, and also because these large-scale features tend to be reproduced relatively well in atmospheric models.

Many studies have linked Atlantic tropical cyclone activity to the African climate. On seasonal/decadal timescale, a positive correlation has been found between West African rainfall during the JJAS months and Atlantic hurricane activity of the same year (Landsea and Gray, 1992). Although, whether or not this correlation is stationary has been questioned recently (Aiyyer and Thorncroft, 2006; Fink et al., 2010). The relationship between West African rainfall and Atlantic TC is usually interpreted such that changes in the large-scale environment over the Atlantic, more precisely the Main Development Region (MDR) where most of TC form, are induced by latent heat release driven by deep convection over the African continent such as to impact cyclogenesis. Positive precipitation anomalies (and thus positive latent heat anomalies) are associated with lower vertical wind shear, conducive to cyclogenesis, through changes in upper level easterly winds.

On daily timescale, many Atlantic TCs and a majority of the most intense hurricanes (category 3-5 on the Saffir-Simpson scale) can trace their origin back to African Easterly Waves (AEWs; Landsea, 1993). These synoptic systems propagate westward over the

Sub-Saharian region, typically with a period of 3-5 days and a wavelength varying from 2500 to 3500 km. These AEWs grow through a mixed barotropic-baroclinic process, deriving their energy from the African easterly jet, a maximum in the zonal wind of $12 - 15\ ms^{-1}$ at 600 hPa and $\sim 15°N$ over Northern Africa, and the relatively strong meridional gradient in low-level temperature south of the Sahara (Burpee, 1972; Reed et al., 1977).

While some attempts have been made to evaluate AEWs in GCMs and RCMs (Chauvin et al., 2005; Hsieh and Cook, 2005), the downstream impact on TC activity has not been addressed. Conversely, in the TC studies mentioned above, relationship with AEWs is not investigated. Failure to capture an adequate relationship between Atlantic TCs and AEWs could have a negative impact on the ability of a RCM or GCM to project future tropical cyclone activity. Here, we attempt to bridge this gap by evaluating the ability of a RCM at capturing observed Atlantic TC activity and by studying how the simulated TCs relate to upstream AEW activity. Moreover, we investigate the role of boundary conditions on TC and AEW activity, as well as the impact of boundary location on TC activity and the further impact this has on the relationship between the two. The aim is to highlight the respective role of AEWs and pilot-derived large-scale fields on Atlantic TC activity.

In section 2, we give a description of the model used, the experimental set-up, the TC tracking algorithm and of the genesis potential index used to assess large-scale conditions favourable to TC formation. In section 3, the simulated climatology of Atlantic TCs and AEWs are evaluated in a range of high-resolution simulations and the impact of upstream AEWs on TC climatology in the different configurations is investigated. In section 4, we analyse interannual variability of Atlantic TCs in the different simulations as well as the role played by AEWs in the detected variability. Finally, in section 5, we compare an ensemble of simulations performed with climatological SSTs with an ensemble of observed SSTs. Concluding remarks are in section 6.

3.2 Model Description and Experiment Configuration

3.2.1 A brief description of GEM

The Global Environmental Multiscale (GEM) model is a fully non-hydrostatic model, employing a semi-implicit, semi-Lagrangian dynamical core on an Arakawa staggered C-grid. The model uses a hybrid-terrain-following vertical coordinate (Simmons and Burridge, 1981) with 53 levels (top at 10 *hPa*) in limited-area mode *and 60 levels (top at 2 hPa) in global-variable resolution mode (see below).* GEM uses the Kain-Fritsch scheme (Kain and Fritsch, 1990) for deep convective processes, the Kuo transient scheme for shallow convection (Kuo, 1965 ; Bélair et al., 2005), the Sundqvist scheme (Sundqvist et al., 1989) for large-scale condensation and the correlated-K scheme for solar and terrestrial radiation (Li and Barker, 2005). Subgrid-scale orographic gravity-wave drag is due to McFarlane (1987) and low-level orographic blocking to Zadra et al. (2003). Land surface processes are represented by the ISBA scheme (Bélair et al., 2003). Finally, sub-grid scale turbulent fluxes are calculated using an implicit vertical diffusion scheme with prognostic turbulent kinetic energy and a mixing length based on Bougeault and Lacarrère (1989) (Bélair et al., 1999). The interested reader is referred to Zadra et al. (2008) and Côté et al. (1998) for more details.

3.2.2 Model Configuration

GEM can be run as a GCM, with global area extent, or as a nested RCM, with the grid covering only a limited area of the globe. In the latter case, global coverage is traded for resolution, allowing one to increase that resolution beyond what is typical of present-day GCMs used in climate studies. Finite geographical coverage in the RCM case means that atmospheric conditions at the edge of the lateral boundaries must be prescribed, either with reanalysis data or a GCM simulation (Davies, 1976).

For this experiment, we integrate the model in both configurations. We first perform two integrations with uniform grids of 2° and 1° resolution, analogous in resolution to present-day GCMs used in climate change modelling and climate change prediction. We then perform a serie of three high resolution limited-area model (LAM) integrations using different grids and different lateral boundary conditions (LBCs). We use i) a small limited area domain at 0.3° fixed resolution, covering only the tropical and sub-tropical Atlantic (between $5°S$ and $\sim 45°N$; figure 3.1a), ii) an intermediate, 0.3° fixed resolu-

tion grid covering the tropical and sub-tropical Atlantic and part of Western African (figure 3.1b), and iii) a large 0.3° resolution grid, extending from the Eastern Pacific to the Arabian Sea (figure 3.1c). For i), ii), and iii), the resolution remains constant and the western, southern and northern boundaries remain fixed while the eastern boundary is allowed to vary.

For the three LAM configurations, we use a serie of LBCs : 1) output from the GEM-Global 2° integration, 2) output from the GEM-Global 1° integration (hereafter referred to as LAM-GEM2d and LAM-GEM1d, respectively), and 3) European Centre for Medium-Range Weather Forecasts (ECMWF) Reanalysis data, ERA-40 (Uppala et al., 2005 ; hereafter referred to as LAM-ERA). Since ERA40 does not extend beyond August 2002, we use the ECMWF operational analyses to cover the 2002-2006 period. Finally, we performed two integrations with grid i) and ERA40 reanalysis, but using 1979-2006 climatological SSTs. No large-scale spectral nudging has been performed in this study.

Comparing simulations performed using grid i) will highlight the impact of LBCs, more specifically AEWs, on downstream Atlantic TC activity. Comparing grids i) and iii) with similar LBCs will highlight the benefit of simulating AEWs at high resolution, and, more generally, comparing grids i), ii) and iii) will highlight the role the LAM domain size play in terms of TCs and the control of TCs by AEWs when using the LAM technique. Finally, comparing simulations performed with grid i) and observed SST vs climatological SST should help isolate the impact of upstream AEWs on MDR TC activity.

All integrations have been performed using observed SSTs and sea-ice fraction derived from the Atmospheric Model Intercomparison Project v2 (AMIP2 ; Gleckler et al. 1996), applied in the model on a daily basis from linearly interpolated monthly mean data. Global integrations were started on September 1st, 1978, and ended on December 1st, 2006, thus covering 28 Atlantic hurricane seasons (1979-2006). The LAM simulations were integrated for 6-month periods starting on June 1st for the same 28-year period. This represents a total of 420 overlapping hurricane seasons simulated at high resolution.

3.2.3 Detection and Tracking of Tropical Cyclones

To efficiently assess simulated TC activity, storms are detected and tracked through an automated procedure, which determines whether or not specific atmospheric conditions, similar to those observed in 'real" TCs, are present in the virtual data. When the predetermined criteria are satisfied for a sufficient number of consecutive timesteps, a TC is considered to be present. We briefly review this procedure here, but more details can be found in Caron et al. (2010).

The objective criteria used to detect TCs, derived from Walsh et al. (2007), are as follows :

- a minimum in central pressure ;
- a relative vorticity maximum at 850 $hPa > 4 \times 10^{-5}\ s^{-1}$;
- the surface (10 m) winds exceed 17 $m\ s^{-1}$ (65 $km\ h^{-1}$) in the vicinity ($< 2°$ of the center ;
- the number of consecutive, detected centers cover at least a 24 h period ;
- a positive temperature anomaly in the mid- to upper-troposphere. This warm core anomaly is detected if the maximum (spatially-average) temperature, in the vicinity ($< 2°$) of the center at 500 hPa and 250 hPa, is $> 1°C$ and $> 0°C$, respectively, higher than the mean temperature at a radius of $< 5°$ for the same two pressure levels.
- the low-level (850 hPa) vorticity is higher than the upper-level (250 hPa) vorticity.

To avoid multiple counting of storms that decrease below TC strength at a given time but re-intensify later on, we relax the detection conditions and rerun the tracking procedure over the same set of data. We then compare both sets of tracks and retain only the tracks that were detected with both sets of criteria. The relaxed criteria are :

- a minimum in central pressure ;
- a maximum in vorticity greater than $4. \times\ 10^{-5}\ s^{-1}$;
- surface wind speed greater than 10 $m\ s^{-1}$ in the vicinity of the center ;
- low-level (850 hPa) vorticity greater than upper-level (250 hPa) vorticity (implicitly a warm core).

In short, this second set of criteria allows tracking of TC precursor systems and fills in the gaps when TC maximum wind speeds oscillate around the tropical storm threshold of 17 $m\ s^{-1}$ and/or the positive temperature anomaly in the upper troposphere is weak. Comparing the two sets of tracks allows us to reject the systems detected with the second set of criteria that never reached TC strength. The TC tracks detected are then used to build climatological and annual statistics, thus allowing for easy comparison between each integration and with observed climatology. For more details on the tracking of TCs in GEM, the reader is referred to Caron et al. (2010).

3.2.4 Genesis Potential Index

In order to analyse the impact of changes in the large scale field on TC activty, we compare TC distributions to a cyclogenesis potential index comprised of large-scale fields known to influence TC formation. The selected fields are the vertical wind shear (V_{shear}) between the upper (200 hPa) and lower (850 hPa) troposphere, low-level (850 hPa) vorticity (ζ), mid-tropospheric humidity (700 hPa, $\mathcal{H}$) and atmospheric instability, as expressed by the Maximum Potential Intensity (MPI), which represents the theoretical maximum 10 m wind speed of a mature tropical cyclone given the current atmospheric instability and ocean surface temperatures. Together, these fields make up the Genesis Potential Index (GPI; Emanuel and Nolan, 2004), defined as

$$\mathrm{GPI} = |10^5 \eta|^{\frac{3}{2}} \left(\frac{\mathcal{H}}{50}\right)^3 \left(\frac{\mathrm{MPI}}{70}\right)^3 (1 + 0.1 V_{shear})^{-2} \tag{3.1}$$

where η is the absolute vorticity. The GPI has been shown to be a good predictor of tropical cyclone activity (Camargo et al., 2007a). More information on the GPI can be found in Camargo et al. (2007b).

3.3 Climatology

3.3.1 Atlantic Tropical Cyclones

We begin evaluating the relationship between simulated AEWs and Atlantic TCs by comparing TC activity in the different GEM integrations. We first compare TC activity in the simulations performed with the smallest LAM grid, which covers only the Atlantic (figure 3.1a). In this configuration, AEWs occur entirely within the pilot (reanalysis or GCM simulation) and the waves "propagate" into the LAM through the eastern

boundary as a prescribed boundary condition. Cyclogenesis locations for the simulations performed using ERA40, GEM 1° and GEM 2° as LBCs can be seen respectively in figure 3.2(a), 3.2(b) and 3.2(c). Cyclogenesis is defined here as the locations where the storms were first detected by the automated procedure, which makes it easier to separate between AEW-originating and non-AEW-originating TCs. For comparisons, observed cyclogenesis for the equivalent 1979-2006 period can be seen in figure 3.2(l).

Compared to observations, the small LAM driven by ERA40 forms too many TCs overall, most of which occur over the MDR region (defined here as the area located between $8°N$, $20°N$, $80°W$ and $15°W$), where twice as many TCs as observed are formed. By comparison, the small LAM driven with GEM 1° forms a reasonable number of TCs overall including the MDR, although there does appear to be an underestimate in TC activity over the Gulf and the Caribbean Sea, which is compensated by an overestimate East of the American coast. Caron et al. (2010) showed that the underestimate over the Gulf of Mexico resulted from a dry bias in the mid-troposphere while the underestimate over the Caribbean Sea was linked to high wind shear, originating from strong convection over the South American continent in the GEM Global simulation. The small LAM driven by GEM 2° also gives a reasonable overall number of TCs although the spatial distribution is quite different from the simulation driven by GEM 1°. In particular, there is a significant shift in cyclogenesis from the MDR to the subtropical region, with the GEM 2° driven integration showing very high activity beside the eastern coast of the U.S. Over the region most likely to be impacted by incoming AEWs, the MDR, there is approximately a 100% increase in cyclogenesis going from the LAM driven by GEM 2°, to the LAM driven by GEM 1°, and again to the LAM driven by ERA40.

We then perform three simulations using the same LBCs (ERA40, GEM 1° and GEM 2°), but with a larger grid. This grid of intermediate size has the same western, southern and northern boundaries as the previous grid, but the eastern boundary is shifted to the Greenwich meridian (figure 3.1b). Simulations performed with this grid will be referred to as MEDLAM. In these simulations, AEWs still propagate into the grid from the eastern lateral boundary (as they originate East of the Greenwich Meridian), but are allowed to evolve over the Western part of Africa, within the LAM domain, at high resolution. Also, the transition from land to ocean occurs completely within the domain of simulation. Cyclogenesis events for these three simulations are shown in figures 3.2(d-f). Even though cyclogenesis tends to occur closer to the African coast, the results are

strikingly similar to those shown in the first row of figure 3.2 : the overall number of cyclogenesis events is fairly constant in the three pairs of simulations, the relative distribution between the different Atlantic regions also remains relatively constant and the ~100% increase in cyclogenesis events over the MDR as we go from GEM 2° to GEM 1° to ERA40 LBCs is still present. In the MDR, both LAM runs driven by GEM 1° form the most realistic number of TC's, while the ERA driven LAMs overestimate TCs and the GEM 2° driven LAMs significantly underestimate TC numbers. This pattern is reversed off the American coast with the LAM driven by GEM 2° exhibiting the largest TC genesis numbers.

Finally, while again keeping the western, southern and northern boundaries fixed, we extend the eastern boundary such that the grid encompasses all of Northern Africa (figure 3.1c). Simulations performed with this grid will be referred to as BIGLAM. In this configuration, the high resolution domain covers the entire AEW track. The formation and propagation of AEWs thus occur entirely within the LAM domain. With this larger grid, we perform two simulations, started 24 h apart, with ERA40 as LBCs, two using GEM 2° and one using GEM 1°. This is done to sample the robustness of our results. Ideally, we would have liked to increase the ensemble size beyond two members, but were constrained by limited computer resources. Also, we chose to create ensembles with this larger domain instead of the smaller ones since this domain has the largest freedom to deviate from the boundary data. Cyclogenesis events for these integrations are shown in figure 3.2(g-k). The total number of TCs for the ERA40 driven integration is somewhat reduced compared to the small and intermediate LAMs. The total number of TCs in GEM 2° driven runs improves significantly over the previous two configurations. While the LAM driven by GEM 1° appears to be less sensitive to domain size, although moving the eastern boundary further East does increase the total number of storms somewhat in the GEM 1° driven integration. The increase is particularly noticeable over the MDR region, where the total now lies relatively close to the total in the ERA40 and GEM 2° driven integrations. This is not entirely unexpected, since LBCs will have a smaller impact on larger domains, with the internal LAM physics and common SST forcing dominating.

To summarize, the impact of different LBCs on the total number of TCs reduces as the domain size increases, the largest differences in TC activity are observed in the smallest LAM, especially over the MDR where AEWs propagate into the LAM and the

sensitivity to the domain size is biggest for GEM 2° LBCs. Discussion of the underlying causes behind these differences is deferred to section 3.3.3, after an analysis of AEW activity in the different LAMs has been made.

3.3.2 African Easterly Waves

From the results of the previous section, it is clear that both the LBC dataset and the location of the eastern boundary play a significant role in the Atlantic tropical cyclone genesis simulated by a given LAM. Changes in either will impact how the AEWs enter the domain of integration, subsequent downstream TC activity as well as large-scale fields within which TCs form. In this section, we identify differences in AEW activity between the different configurations presented previously. We then go on to relate these differences to explainable differences in downstream TCs.

In order to identify and compare GEM AEW activity, we first compute the mean power spectrum of the 850 hPa meridional wind, which has been shown to be a good indicator of AEW activity (Moustaoui et al., 2002). We do this over the region limited by $8°N$, $12°N$, $17°W$ and $5°W$. The 850 hPa level was also shown to be the level with highest meridional kinetic energy linked to AEW activity in Caron et al. (2010). Results for the different simulations for 1986 are shown in figure 3.3 with the ERA40 activity also shown in 3.3a. This year was chosen as an ENSO-neutral year; results generally hold for other years as well. It should be noted that ERA40 precipitation variance in the 2-6 day window is somewhat underestimated compared to satellite-derived TRMM (Adler et al., 2000) data (figure 3.4). Although straight modeling link between diabatic heating (linked to precipitation) and dynamics (wind) is not totally complete as there is the potential for assimilation of wind information that might offset some of the weak signal from the diabatic forcing, this nonetheless suggests that ERA40 wind variance, in the same 2-6 day window, is biased low compared to reality.

All simulations exhibit increased activity in the 2.5 to 6 day range, with a peak around 4 days. This result is fairly constant across the years, as can be seen in table 3.1, which shows the mean period of maximum power for all simulations and reanalysis (ERA40 and ECMWF) as well as their respective standard deviation. There appears to be an increase in power (in the $2.5 - 6$ day range) with resolution and some differences in intensity amongst the high resolution simulations, with BIGLAMERA exhibiting the

strongest activity, MEDLAMGEM 2° the weakest of the high resolution, and GEM 2° the weakest overall. Results are similar for 850 hPa vorticity.

After recognizing there is an increase in wave activity in the 2.5-6 day window over the Sahel region, we apply a 2.5-6 days bandpass filter at each grid point, to the 850 hPa meridional wind component. Figure 3.5 shows a Hovmöller diagram of the resulting filtered meridional wind along 10° between $30°W$ and $40°E$ for a two-month period (August-September, 1986) for ERA40, two high-resolution simulations (BIGLAMERA, BIGLAMGEM2d) and for the 1° and 2° global integrations. Waves are clearly seen propagating westward in all four cases, with a period of ~4 days and a wavelength ranging between 2500 and 3500 km. The simulated period and wavelength are very similar to those previously detected in observations and reanalysis (Reed, 1978; Diedhiou et al., 1999). While the differences are not always so pronounced, BIGLAMERA tends to form more intense waves, starting further East, than the other high-resolution simulations and BIGLAMGEM1d tends, generally, to form stronger waves than BIGLAMGEM2d (not shown). Finally, weaker waves are detected in the global 2° simulations while the global 1°, which forms AEWs further East than GEM 2°, shows waves of intensity similar to BIGLAMGEM2d.

To compare the climatological differences in AEW activity, we evaluate the mean 28-year variance of the $2.5 - 6$ day bandpass filtered 850 hPa meridional wind during the JJASO season in the various simulations and in ERA40 reanalysis. Results are shown in figure 3.6. Reanalyses show two maxima in activity : a northern track around $20°N$, and a southern track around $10°N$. Both sets of tracks have previously been identified by Thorncroft and Hodges (2001), who linked cyclogenesis in the Atlantic primarily to the southern tracks, although more recently, Ross and Krishnamurti (2007) showed some northern waves that migrate southward when reaching the coast can also play a role in cyclogenesis in the early part (June-July) of the season. Wave activity in GEM 2° appears weaker than in ERA40 and shows only one track, along $\sim 17°N$, corresponding more or less to the northernmost track shown in reanalysis, while having an almost non-existent Southerly wave track. Stronger wave activity is seen as we increase the global model resolution from 2° to 1°, with the appearance of a southerly wave track and maxima in activity located in a similar location to reanalysis. The northern track however remains the strongest of the two in contrast to the relative distribution in reanalysis.

Figure 3.6 also shows the mean JJASO filtered variance for the three simulations performed with the intermediate and large LAM grids. Comparing AEW activity in the different simulations reveals that :

- LBCs play a dominant role in how AEWs are simulated in the LAM, even in the large grids.
- there is a large difference in AEW intensity between GEM 2°- and GEM 1°-driven integrations, reminiscent of the large difference detected in the two global integrations. This is especially true in the case of the intermediate grid, where boundary conditions play a larger role than in the large grid.
- AEWs are detected in some simulations as far East as $10°E$, in agreement with previous studies (Reed et al., 1988; Moustaoui et al., 2002).
- AEW activity increases as resolution is increased and as the eastern boundary is moved eastward, i.e. giving more space for systems to spin-up under increased resolution.
- most of the increase detected by moving the eastern boundary eastward occurs in the southern wave track. In fact, pushing the boundary further East tends to move the absolute maximum in GEM-driven integrations from the northern to the southern track.

Table 3.2 shows the total number of waves detected coming off the coast of Africa in the different simulations, for the period JJASO 1979-2006, based on values greater than $0.5\ ms^{-1}$ [1] of the filtered meridional wind speed between $11°N$ and $13°N$ at the African coast. Figure 3.7 shows the wave intensity distribution for the same simulations. The total number of waves does not vary significantly between integrations, all simulations displaying a total between 1083 and 1147, or an average of 8 waves per month, consistent with the average of 7-8 waves detected by Avila and Pasch (1995) during the summers of 1967-1993. Differences in activity originate mainly from differences in the intensity of waves, as can be seen on figure 3.7. On average, increasing resolution and pushing the eastern boundary eastward leads to stronger waves leaving the African coast. These results appear consistent with the small sample presented in the Hovmöller diagrams of figure 3.5.

---

1. The $0.5\ m\ s^{-1}$ threshold has been used by Diedhiou et al. (1998) to identify AEWs. Increasing the threshold limit to $1\ ms^{-1}$ reduces the totals slightly, but does not significantly impact the overall results.

In order to understand the origin of the large differences in wave activity amongst the different simulations, we plot the meridional cross sections of the mean August-September variance of the $2.5-6$ day filtered meridional wind along a meridional cross-section at $30°W$, $10°W$ and $10°E$ for BIGLAMERA, BIGLAMGEM1d and BIGLAMGEM2d in figure 3.8. At $10°E$, wave activity is present only in BIGLAMERA and shows a maximum at 700 hPa, while the GEM driven integrations show no activity at this longitude. At $10°W$, all three simulations show two main areas of activity : a more southern track along $11°-12°N$ with maximum activity at $700-850$ hPa and a more northern track along $20°N$ with maximum amplitude at $925hPa$. The northern track is strongest in BIGLAMERA, but fairly similar in both BIGLAMGEM2d and BIGLAMGEM. Conversely, the southern tracks show significant differences between the three integrations, in accordance with figure 3.6. Finally, at $30°W$, only one track is visible along $11°-12°N$, with maximum activity located at $700-850$ hPa.

The fact that the northern tracks are relatively similar in all three integrations while large differences are observed in the southern tracks arises due to the different processes through which wave growth occurs in the two different areas : the wetter southern waves were observed to grow through conversion of zonal kinetic energy to eddy kinetic energy while the dryer northern AEWs were observed to develop mainly through conversion of zonal available potential energy to eddy available potential energy (to eddy kinetic energy), originating from the large thermal gradient over Africa's surface (Norquist et al., 1977 ; Moustaoui et al., 2002 ; Diedhiou et al. 2002). Comparison of the cross sections of the covariance between the $2.5-6$ day filtered meridional wind and temperature (figure 3.9), which was shown to represent conversion from zonal available potential energy to eddy available potential energy (ibid.), confirms that this process is exclusive to the northern track. Maximum covariance occurs between $15°-20°N$ in all three configurations. This is consistent with figure 4b in Diedhiou et al. (2002), who performed a similar analysis using NCAR reanalysis (August-September 1979-1995). The negative covariances represents a southward heat flux driven by the warm northerly winds of the Sahara.

Comparison of the cross sections of the covariance between the $2.5-6$ day filtered meridional and zonal winds ($u'v'$; figure 3.10), which is considered to estimate the conversion

term from zonal kinetic energy to eddy kinetic energy, helps explain the differences detected in the southern track. At $10°E$ significantly larger covariance values are detected in BIGLAMERA when compared to the other two integrations. At $10°W$, positive covariance values are detected up to almost 400 hPa in BIGLAMERA, but stop at 600 hPa in BIGLAMGEM1d and BIGLAMGEM2d. At $30°W$, large covariance values are observed across the mid-troposphere in all three cases. These differences in covariance between the different integrations appear linked to the structure of the African Easterly Jet (AEJ). Figure 3.11 shows the meridional sections of mean zonal wind at the three same longitudes for the same three simulations. The AEJ is seen at $\sim$ 600 hPa and above between $10°N - 15°N$, depending on the longitude and the simulation. In the BIGLAMGEM1d and BIGLAMGEM2d integrations, the wider jet structure, especially apparent at $10°W$ appears to be linked to smaller positive covariance values south of the jet. The differences in covariance values between $10°W$ and $30°W$ are especially noticeable in BIGLAMGEM2d and appear to coincide with changes in the shape of the AEJ. This flat jet structure visible in BIGLAMGEM2d, and to a lesser extent in BIGLAMGEM1d, is directly inherited from the pilot through the southern boundary. The lower resolution simulations show a wider AEJ, centred between $5°N - 10°N$ (not shown). Both BIGLAMGEM1d and BIGLAMGEM2d also show a tendency towards an AEJ located at lower latitude than in BIGLAMERA. This could be related to a stronger monsoon wind in BIGLAMERA bringing colder monsoonal wind deeper into the continent, thus reducing the temperature at the southern edge of the Sahara and moving the strong temperature gradient responsible for the maintenance of the jet, further north. Finally, we computed in full the dominant term of barotropic energy conversion from zonal to eddy kinetic energy ($-(u'v')\frac{\partial u}{\partial y}$; Norquist et al., 1977), averaged between $20°W - 0$, the area showing the most wave growth in the simulations. Results can be seen in figure 3.12. BIGLAMERA is clearly the simulation showing the strongest barotropic growth, with maximum values located in the vicinity of the southern wave track.

3.3.3 Impact of AEW activity on TC activity

In this section, we investigate the link between the simulated TC activity shown in section 3.3.1 and the AEW activity discussed in section 3.3.2. Comparing TC activity in figures 3.2 and the associated AEW activity in figure 3.6 reveals that the relationship between AEWs and Atlantic TCs is not straightforward : higher AEW activity does not necessarily translate into higher TC activity. For example, even though ERA40 AEW activity is weaker than almost all AEW activity produced by the different GEM confi-

gurations, the small LAM driven with ERA40 (with ERA40 waves as LBC) produces the largest number of TCs (with a marked maxima close to the African coast), particularly close to the African coast. Similarly, large differences in wave activity between the simulations performed with the small grid, where AEWs are those of the pilot (ERA40, GEM 1° and GEM 2°), and the intermediate grid do not lead, regardless of the LBC dataset, to an equivalent change in TC activity. As an exemple, note the large difference in variance between ERA40 and MEDLAMERA (figure 3.6) that does not translate in TC differences in the MDR (figure 3.2). On the other hand, changes in simulated AEW activity between the integrations performed with the intermediate and large grids, independent of LBC type, are accompanied by a change in TC activity.

We start by comparing the activity in the simulations performed with the largest grids. In this ensemble, the LBCs should have the smallest impact (of all three grids) on TC activity given their relative distance from the Atlantic and the MDR. This appears to be the case since TC activity is relatively similar over the MDR in all five simulations for the 1979-2006 period. In fact, TC activity over the MDR is similar when driven by GEM 2° and GEM 1° and slightly higher ($\sim$ 2 TCs/year) when driven with ERA40. Before attributing this change to changes in AEW activity, we compare the GPI, which encompasses the different large-scale fields known to impact cyclogenesis, between the three configurations. Mean GPI values for the ASO season obtained with the largest grid are shown in the first row of figure 3.13. Both GEM driven runs show similar GPI values consistent with the simulated cyclogenesis. GPI in the ERA40 driven simulations is also very similar, except at the eastern edge of the MDR, where it tends to be higher, also consistent with higher TC activity in these simulations. While a large portion of the MDR exhibits lower vertical wind shear in BIGLAMERA, close to the African coast, higher GPI values in ERA40 driven runs are the result from higher ($\sim$ 5%) relative humidity.

When comparing TC activity in the ERA driven simulations with the GEM 2° driven (the most dissimilar simulations in terms of TCs), the overall number of Atlantic TCs is relatively similar, but a larger fraction of TCs form in the MDR in BIGLAMERA than in BIGLAMGEM2d, which conversely produces more TCs North of 20°. BIGLAMGEM1d lies somewhere in between, but closer to BIGLAMGEM2d. In this configuration, the largest impact of higher AEW activity is not to increase the total number of TCs produced, but to move cyclogenesis events closer to the African coast

(to the South-East of the basin). In particular, BIGLAMERA appears to have excessive amounts of TC genesis directly off the African coast, compared to observations in figure 3.2. This results from the combination of active AEW variability (figure 3.6c) and a, perhaps overly, supportive large scale. BIGLAM driven by GEM 1° and 2° have very similar TC genesis numbers in the MDR region, even though there is a clear increase in AEW activity in the southern AEW track (compare figure 3.6f and 3.6i). The two BIGLAMGEM configurations have very similar large scales, as evidenced by the GPI values, suggesting that beyond a given threshold of AEW activity, it is the degree of "supportiveness" of large-scale conditions over the Atlantic that determines TC activity. We also note that the degree of "supportiveness" of the large scale near the African coast, while correlating with local TC genesis numbers, is inversely correlated with TC genesis outside the MDR (predominantly to the North). This essentially results from the fact that, if a wave develops in a supportive environment near the African coast, it is no longer available for cyclogenesis further North. Conversely, if waves do not develop in the MDR, then the disturbances remain intact to perhaps experience cyclogenesis later in their track.

Comparison of intermediate size simulations show large differences both in terms of TCs and AEWs. AEW activity is seen to increase as LBCs change from GEM 2° to GEM 1° to ERA40 (figure 3.6). This increase is accompanied by a significant increase in TC formation over the MDR (figure 3.2). However, it is not clear that the latter TC increase is solely due to the former AEW increase, since the GPI over the MDR is also seen to increase in the MEDLAM configuration when LBCs change from GEM 2° to GEM 1° to ERA40 (second row of figure 3.13). Low-level vorticity, mid-tropospheric humidity and vertical wind shear all contribute to the increase in GPI values simulated over the MDR. Of these three factors, only changes in low-level vorticity can be directly linked to increase AEW intensity.

Differences in TC genesis between the large and the intermediate size grids are also consistent with changes in GPI values. Due to a $\sim +5\%$ change in relative humidity and a slight decrease in vertical wind shear, GPI increases over the MDR immediately off the African coast, in the intermediate size simulation driven by ERA40, compared to the large grid with the same LBCs. The larger number of TCs forming in the intermediate LAM driven by ERA40 compared to the larger grid, despite weaker AEW activity (figure 3.6), again suggests that the large-scale conditions influenced by LBCs

are the primary determinant of differences in TC genesis numbers in the MDR, at least for AEW activity beyond a certain threshold. Despite relatively similar AEW activity, the intermediate size simulation driven with GEM 1° shows a small decrease in TC numbers over the MDR compared to the simulation performed with the largest grid and same LBCs. This decrease in activity is consistent with the small decrease in GPI, resulting from lower relative humidity values, over the same region. This primary role of large-scale conditions ahead of AEW activity in determining TC numbers in the MDR is most evident for the Small LAM driven by ERA40 where relatively weak AEW variability (figure 3.6) is accompanied by double the number of TCs forming in the MDR than seen in observations, mainly due to the highly supportive large scale as evidenced by the high GPI values in this region (figure 3.13). The primary term increasing GPI compared to the GEM driven Small LAM is higher RH values (15%-20% higher during the most active month of September). Andersson et al. (2005) and others have shown relative humidity values are overestimated in ERA40 (this was one reason for the development of the ERA-Interim dataset). Combined with the excessive TCs in SMALL-LAMERA, we suggest the GPI in SMALL-LAMERA (and ERA40 itself) overestimates reality. Furthermore, we suggest that this effect (positive bias) is still evident in MEDLAMERA in terms of its impact on TC cyclogenesis and leads in general to an incorrect relationship between AEW intensity and TC development in the ERA driven runs, with AEW intensity increases being accompanied by a reduction in the number of TCs formed in the MDR as the LAM domain size increases from SMALL to MED to BIG. This occurs because as the domain size increases, AEWs have more high resolution space to develop, while the larger domain reduced the impact of the ERA boundaries on relative humidity and GPI values over the MDR region. The relatively small differences in relative humidity values in the MDR between the ERA driven runs of varying size (5%-10% from small to intermediate and 0%-5% from intermediate to large) and the large response of TCs indicates a high level of accuracy is required to accurately simulate processes controlling TC genesis over the tropical Atlantic.

There is consistent picture of TC numbers in the MDR increasing as one moves from GEM 2° to GEM 1° to ERA40 LBCs with a commensurate reverse signal in TC genesis numbers off the American coast, being often highest in GEM 2° driven simulations. These trends become less evident as the influence of the LBC decreases with increasing domain size. The inability of AEW disturbances to develop in the MDR, either due to AEWs being too weak or the large scale environment not supportive of genesis, results

in these disturbances continuing to propagate across the Atlantic, eventually forming TCs in erroneous number compared to observations over warm SSTs further west.

Large differences in TC activity can be seen between the intermediate and large grids when driven by GEM 2°. With these LBCs, the intermediate size configuration produces both weaker waves and lower GPI values over the MDR than the large domain. A significant decrease in relative humidity (up to more than $10\% - 15\%$) and increase in vertical wind shear of about 10 ms^{-1} are responsible for these differences in GPI over the region. On its own, a 15% increase in relative humidity over the MDR in the BIGLAMGEM2d would lead to $\sim$ 100% increase in GPI values over the MDR. Due to the inverse relationship between vertical wind shear and GPI, the main impact of $10ms^{-1}$ decrease in vertical wind shear, while slightly increasing GPI values where they are already conducive to cyclogenesis, is to increase the area favourable to TC development. This change in wind shear likely explains why most TCs form along a thin band between $9° - 10°N$ in MEDLAMGEM2d, but form across a wider $8° - 15°$ band in BIGLAMGEM2d (see figure 3.2). The overall increase in TC genesis numbers in BIGLAMGEM2d compared to MEDLAMGEM2d is likely a combination of both a more active (southerly) AEW track and a more conducive large-scale. Finally, higher GPI values, due to higher relative humidity and lower wind shear, are also detected East of the American coast in the intermediate size grid compared to the larger one, also with GEM 2° LBCs. Again, this is consistent with changes in simulated TC activity. The systematic failure to produce realistic cyclogenesis locations in the small grids forced by GEM 2° and to a lesser extent GEM 1°, i.e. too few TCs in the MDR and too many off the American coast, is readily apparent when plotting SST distribution at cyclogenesis (not shown). In these simulations, SSTs tend to be bias low, with many storms forming over $24 - 25°C$. Such a systematic error would likely render any climate change sensitivity, performed with this configuration, incorrect and suggests the need for a larger LAM domain than the small one tested here when investigating TC changes in climate change simulations driven by AOGCM of 1° or coarser.

Cyclogenesis numbers do not differ greatly between the small and intermediate grids [2]

2. The westward displacement of TC formation detected in the smaller grid is due to the eastern boundary being located over the Atlantic. The tracking routine does not trace back the TCs to the pilot simulation.

when driven by GEM 2° or 1°. This is consistent with the relatively constant GPI values simulated over the entire Atlantic domain for these configurations (third row, figure 3.13). Despite stronger AEW activity in the intermediate configurations, monthly mean values of 850 hPa vorticity remain, in both GEM 2° and 1° driven cases, relatively constant over the MDR (not shown), suggesting the increase in AEW activity obtained by moving the Eastern boundary eastward to 0° does not propagate significantly over the MDR. The relatively constant number of TCs between the small and intermediate grids using ERA40 as LBCs is more difficult to explain, especially given the large differences in upstream AEW activity. In moving from the small domain to the intermediate grid with ERA boundaries, there is a significant increase ($\sim$ 10%) in monthly mean relative humidity over most of the Atlantic, including the MDR. This translates into a GPI increase of $\sim 80\% - 90\%$. A number of studies have documented a positive bias in tropical relative humidity values (Andersson et al., 2005 ; Uppala et al., 2005). This bias appears to be passed on to the RCM when using the smallest grid (and to a lesser degree, also to the intermediate size grid). The higher relative humidity values are supportive of deep convection and thereby TC formation, suggesting weak AEW activity at the boundaries of SMALL-LAMERA, compared to stronger waves in the MEDLAMERA, is compensated for in terms of TC genesis by a large scale environment over the tropical Atlantic that is most likely overly supportive of TC development . In other words, in terms of simulating TC development over the Atlantic, a negative bias in AEW activity can potentially be (more than) balanced by biases in large scale fields, such as relative humidity or vertical wind shear, resulting in accurate simulation of TC numbers from two compensating errors. Such errors would likely induce an incorrect TC sensitivity to anthropogenic climate change in this configuration, even though the basic simulated TC numbers look reasonable.

To conclude, the large-scale atmospheric environment appears to be the primary control on simulated TC activity, with AEW activity in itself being insufficient to predict simulated Atlantic TC numbers. Increasing the size of the LAM domain reduces the influence of biases in the boundary data, which, for the smaller domains, has a large impact on TC activity.

3.4 Interannual Variability

3.4.1 Atlantic Tropical Cyclones

A climate model should be able to reproduce both the climatology of TCs as well as the observed fluctuations in TC activity. Past studies have indicated a link between Sahel rainfall, AEWs and interannual variability in TCs (Landsea and Gray, 1992; Goldenberg and Shapiro, 1996), with this link itself potentially changing over time (Aiyyer and Thorncroft, 2006; Fink et al., 2010). Thus, in this section, we compare the interannual variability of simulated AEW and TC activity in order to determine 1) if the various model configurations can simulate interannual variability in AEW activity and 2) if they can, whether this has an impact on simulated TC interannual variability. We use three metrics similar to those of Caron et al. (2010) to evaluate the model's ability to capture Atlantic TC interannual variability. They are :

- annual number of tropical cyclones forming in the MDR (south of $20°N$ and east of $80°W$), these being the most likely to originate from AEWs;
- annual number of hurricanes over the entire basin;
- a corrected annual power dissipation index (PDI).

Originally defined as the cube of the storm maximum wind speed summed over the lifetime of each storm, the PDI (Emanuel, 2005) was shown to be severely underestimated in GEM simulations (Caron et al., 2010). The primary reason for this was the failure of GEM to produce intense hurricanes (beyond category 2 on the Saffir-Simpson scale) and associated high wind speeds likely due to low resolution and excessively high atmosphere-surface momentum exchange due to shortcomings of the drag coefficient parameterization at high wind speeds (Moon et al., 2007; Walsh et al., 2010). Because the PDI scales with the cube of the wind speed, a few intense storms are responsible for the very high PDI values observed during certain years (e.g. 2004 and 2005), the failure to produce such TCs will severely degrade the simulated PDI.

To reduce the impact of this bias, we modify the calculation of the model PDI. Figure 3.14 shows the relationship between storm minimum central surface pressure (CSP) and maximum 10 m wind speed, from both observations and two GEM simulations. The observed relationship between the two fields is not well reproduced in GEM, with model

storms exhibiting category 3-like central pressures, but only category 1 wind speeds. Recognizing that simulated minimum central pressures are more typical of observed TCs than simulated maximum wind speeds, we reevaluated the PDI based on central pressure. For each timestep of all TCs, the simulated minimum central pressure is assigned a new diagnostic wind speed based on the best-fit observed relationship derived from the black curve of figure 3.14. The PDI for each storm is then recalculated using this new wind speed. The new index, henceforth referred to as PDI*, is the PDI that would be measured if the relationship between CSP and 10 m wind speed was accurately reproduced in GEM. Given that there are no storms with pressures lower than category 3-equivalent on the Saffir-Simpson scale (except for a few rare category 4's), this modification does not entirely eliminate the "power deficit" associated with GEM simulations. It is nonetheless a good first order correction. The observed PDI is not changed and is derived from observed maximum wind speed.

Annual mean time series for the three variables described above, for observations and individual simulations, plus the ensemble mean, are shown in figure 3.15. The ensembles are grouped based on types of LBC[3] used. Comparison of the individual temporal correlations given in table 3.3 for the ERA40 driven integrations indicates no obvious difference between the different configurations. No single integration produces the best correlation for all three metrics : all capture approximately the same level of interannual variability and changing the domain size does not appear to significantly affect the capacity of the model to reproduce the observed variability. Not surprisingly, the ensemble mean performs best for all three variables of the ERA40 driven ensembles. For comparison, the ensemble correlation indices for HRs and PDI in Knutson et al. (2007; performed at 18 km resolution) were, respectively, 0.86 and 0.72. Those integrations were performed using spectral nudging, which is not the case here. Spectral nudging forces the large-scale fields simulated in the LAM domain to follow the prescribed boundary forcing fields (Laprise, 2008). When reanalyses are used as LBCs, this technique should generally lead to an improvement in simulated TC activity.

---

3. Here, we also include two 28-year simulations performed with the smallest grid and using slightly different versions of GEM. One version uses an alternate surface flux formulation, based on Moon et al. (2007), while in the second, we also modified the threshold value required to initiate deep convection in the Kain-Fritcsh convective parametrization scheme. Basic results were not significantly affected and the two simulations are used only to increase the ensemble size.

Although it fails to produce very high PDI* values in the latter part (1995 onward) of the 28-year period, figure 3.15i shows that the ERA40-driven ensemble is quite skillful at reproducing the observed PDI interannual variability. The failure to produce very high PDI* values occurs because GEM simulates very few storms with central pressures below 940 hPa, therefore underestimating the PDI* of the most active season, especially those with intense hurricanes. Some of that underestimation is compensated by an excess of simulated TCs, particularly in the smaller ERA40 driven simulations (figure 3.2). The relatively good interannual variability simulated by the ERA40 ensemble indicates that the model captures on years that are conducive to TCs, but does this more through an increase in TC numbers, not more intense TCs. Overall, the simulated PDI* is a significant improvement over the simulated PDI, derived from maximum surface wind, shown in Caron et al. (2010).

Table 3.4 shows linear trends in MDR TCs, HRs and PDI* over the period 1979-2006. The ERA40 driven simulations capture the upward trend in MDR TCs over the period, although with too large a magnitude, and reproduce the total HR trend relatively accurately. In contrast, except for one simulation, the ERA40 driven ensemble slightly underestimates the observed increase in PDI over the same period. Again, this is related to the absence of very strong (category 4, 5) storms in the model. The upward trend in PDI* in the ERA-driven integrations is caused by an increase in the total number of storms forming in the South-Eastern part of the basin, close to the African coast, combined with an increase in the intensity of the strongest storms, similar to that detected by Elsner et al., (2008) using reanalysed observational data. The strongest storms here are those for which the lifetime-minimum surface pressure is located in the first $20th$ percentile for any given year. The first column in figure 3.16 shows the different trends in pressure for the median, 0.75 quantile, and 1.5 times the interquartile range in observations, BIGLAMERA and BIGLAMGEM2d, while the second column shows the various trends in tropical cyclone minimum sufrace pressure by quantile, from 0.1 to 0.9 in increments of 0.1. BIGLAMERA (figure 3.16, second row) does not fully capture the increase in storm intensity observed during the 1979-2006 period, in part due to the failure to produce very intense hurricanes, but gives clear indications towards stronger hurricanes.

The situation is quite different in the GEM 2° driven integrations, where the small and intermediate-size grids integrations fail to capture the observed interannual variability or the observed trends in any of the three metrics. This failure most likely arises from

the overall inability of these configurations to simulate sufficient TC activity in the MDR. Storms forming over that region tend to live longer, and thus become stronger than storms forming closer to the coast or further North (and thus contribute disproportionately to hurricane numbers and PDI) . With GEM 2° as LBCs, an improvement in the ability to capture interannual variability is apparent when simulations are performed with the larger grid. However, the large grid configuration is still significantly poorer than ERA40-driven simulations at capturing observed variability. From table 3.4, the GEM 2° driven runs fail to capture the observed upward trend in activity. This is especially true for the number of hurricanes and PDI, for which both values are severely underestimated. Furthermore, there is no significant increase in the intensity of the strongest storms, as seen in the ERA40-driven integrations (figure 3.16, third row).

One possible factor for the different PDI* and HR trends in the various simulations may be the vertical wind shear simulated over the Atlantic. Figure 3.17a-d shows the different linear trends in vertical wind shear (between 200 hPa and 850 hPa) in ERA40, BIGLAMERA, BIGLAMGEM1d and BIGLAMGEM2d. BIGLAMERA amplifies the analysed decrease in vertical wind shear over the MDR such that a strong decreasing trend, supporting an increased TC activity, is detected in this configuration. In contrast, vertical wind shear in BIGLAMGEM2d and BIGLAMGEM1d are observed to decrease slightly or remain constant during the 28-year period. Both are consistent with the simulated trends in TC activity.

Interannual variability simulated by the small and intermediate domains improves significantly when driven by GEM 1° compared to GEM 2° (table 3.3). This improvement is likely linked to the greater number of storms forming over the MDR linked to stronger AEW activity than in GEM 2°. However, no obvious benefit is seen from using a larger grid in terms of capturing the observed interannual variability, nor does there appear to be an obvious benefit from using GEM 1° over GEM 2° as LBCs for the large domain. Both configurations capture similar levels of interannual variability, likely linked to reasonable AEW input from both (due to the large LAM domain) and same specified SST forcing. Finally, the three GEM 1° driven simulations also fail to capture the upward trend in activity. In fact, despite increasing SSTs, the ensemble mean predicts a slight reduction in activity over the 28-year period (table 3.4) possibly linked to the trend in wind shear seen over the MDR in this integration (figure 3.17d).

The different interannual correlation coefficients detected between simulations sharing the same grid but different LBCs can be explained, in part, through the different large-scale fields passed into the LAM. Changes in these large-scale fields are ultimately driven by the underlying SSTs, which are the same for all simulations. Figure 3.18 shows maps of correlation indices between JASO SSTs and MDR TC timeseries for observations/reanalysis and three simulations performed with the largest grids but different LBCs. Results are similar if we look at hurricanes and PDI*. Observed changes in hurricane activity are seen to correlate with SSTs over the tropical Atlantic, and the western Pacific, and anti-correlate with the Eastern tropical Pacific (more or less the Nino 3.4 region). The LAM driven with ERA40 shows a similar pattern. Conversely, changes in TC activity in the LAM driven by GEM 1° is associated with changes in both the eastern Pacific and in a large portion of the Indian ocean. No significant correlations can be found over the Atlantic. In contrast, the GEM 2° hurricane activity correlates relatively well with the tropical Atlantic, but not with the Pacific ocean. These results are also valid in the second ensemble member, when it is available. Failure to account for both Atlantic and Pacific ocean's influence on Atlantic TCs in GEM driven integrations will necessarily lead to a degradation in the model ability to reproduce observed TC interannual variability.

To summarize, the smallest domain is best at capturing interannual variability and trends when observation-based LBCs (e.g. ERA40) are used, while the largest LAM is better when GCM simulations at low resolution are used as LBCs. This is especially true when TC activity is severely underestimated in the MDR and highlights the danger of relying solely on analyses when designing an appropriate grid. Finally, relatively good TC interannual variability may come about partially from compensating incorrect results/biases, which may give a false impression of accuracy in simulated TC processes and subsequently lead to overconfidence in what may be erroneous climate change signals. For example, the interannual variability in SMALL LAM-ERA may be good because of the combination of weak AEW activity (from ERA40 LBCs) propagating into a large scale atmosphere overly conducive to TC development (moist bias over MDR).

3.4.2 Impact of changes in African Easterly Wave Activity on TCs, Interannual Variability and Trends

Having established the degree to which the various GEM configurations can simulate observed trends and interannual variability in Atlantic TC activity, in this section we investigate the relationship between variations in AEW activity and Atlantic TC activity. To establish to what degree AEW activity contributes to the overall Atlantic TC interannual variability, we start by evaluating the correlation indices between the three variables discussed in the previous section (MDR TCs, HRs and PDI*) and the mean yearly variance of the 2.5-6 day JASO bandpass filtered meridional wind over the region limited by $20°W$, $10°W$, $5°N$ and $15°N$[4]. This area corresponds to the region with the maximum amplitude in filtered V over the African continent, as seen on figure 3.6, and covers the region where AEWs enter the Atlantic region. As mentioned in the previous section, higher variance corresponds to stronger waves but not necessarily to more waves, since all simulations tend to produce roughly the same number of AEWs (table 3.2). In the case of the smallest LAM, which covers only the Atlantic, the correlation is performed with the variance calculated in the pilot (ERA40, GEM 1° and 2° simulations). The correlation indices for the different configurations are shown in table 3.5. Shifting the area over which the mean variance is evaluated does not significantly affect the results. Only the simulations performed with the largest grid and driven with reanalysis show significant correlation with all three selected TC variables, although there is also a clear tendency for AEW correlations to increase with domain size irrespective of the LBC dataset. This result is supported by the long trail of positive correlations between the mean variance timeseries of the filtered meridional wind (over the same African region) and 850 hPa vorticity extending across the Atlantic, from Cape Verde to Cuba and the Bahamas, in the BIGLAMERA simulations, but absent in all the others (not shown). This trail of positive correlations is co-located with the tracks of Atlantic tropical cyclone originating from AEWs in these two simulations.

To understand why BIGLAMERA is the only configuration showing any significant correlation between AEW and TC activity, we evaluated the correlation indices between the same mean Sahel variance timeseries presented above and the JAS timeseries of the GPI as well as its individual components at each grid point over the Atlantic. BIGLA-

4. Although not technically exact, we will refer to this area as the Western Sahel in order to alleviate the text.

MERA is the only configuration showing strong correlation between AEW activity and the GPI across the MDR. BIGLAMGEM1d shows strong correlation over only part of the MDR, while the rest of the configurations show no significant correlations (figure 3.19). For both BIGLAMERA and BIGLAMGEM1d, these correlations appear to be driven by changes in the 200 hPa zonal wind, which show high negative correlation with AEW activity over the MDR in both cases (not shown). This is consistent with stronger convective activity over the African continent leading to stronger upper-level outflow and weaker upper-level westerlies over the MDR (easterly anomalies). With the exception of the intermediate grid driven by ERA40, none of the other simulations show significant correlations between AEW activity and upper-level winds, suggesting that convective activity over the African continent is insufficient to impact upper-level winds in these configurations.

Furthermore, in BIGLAMERA, AEW activity is seen to correlate positively with mean JAS low-level (850 hPa) positive (westerly) zonal winds over the MDR. Westerly zonal winds at 850 hPa near the African coast correspond to the monsoon flow that drives stronger convective activity over the African continent. Changes in the zonal upper-level winds and, in the case of BIGLAMERA, changes in zonal low-level winds, lead to changes in vertical wind shear, which both reflect and support (through strong monsoon flow) increased convective activity over West Africa and in turn modify the GPI values over the MDR.

Since an underestimated 850 hPa meridional wind variance over the Sahel region in ERA40 is likely to lead to a poor AEW-TC relationship, we also investigate JAS Western Sahel rainfall variability using GPCP and simulated rainfall. Correlations between observed and simulated rainfall for the 28-year period are given in table 3.6. The largest grid tends to perform better, especially when driven by GEM 2°. The global 2° simulation completely fails to capture the observed variability and this failure is passed down in the intermediate size simulation, which develops a poorer monsoon due to the constraints of the pilot. We then correlate the western Sahel precipitation with the three measures of Atlantic TC activity. Results are shown in table 3.5. Results obtained using 850 hPa variance generally holds, with BIGLAMERA being the only configuration showing any significant correlations. Although not significant, correlations found in the SMALL-LAMERA configuration are much closer to the correlations derived from observations.

3.5 Simulations with Climatological SSTs

We performed two additional simulations using the smallest grid and ERA40 as LBCs. For these simulations we replaced the time-varying SST field with climatological mean annual cycle SSTs (1979-2006) [5] (henceforth referred to as CLIMSST ensemble). By removing interannual variations in Atlantic SSTs, we hope to better isolate the impact of local SST on Atlantic TC activity. Since we use reanalyses to drive the LAM, we do not completely remove the influence of SSTs. The effect of remote SST variability that has an impact on the large-scale atmospheric conditions propagating into the Atlantic region (such as ENSO-related SST variability) will be transmitted into the LAM domain through the prescribed ERA boundary conditions. Furthermore, tropical Atlantic SST variability that influences the year-to-year intensity of the west African monsoon and convective activity over Africa can be translated back into the LAM region via the ERA40 BCs. The main SST forcing we remove is the direct, local SST impact on AEW and TC development processes over the tropical Atlantic itself.

Figure 3.20 shows the geographical distribution of cyclogenesis events for the two integrations performed with climatological SSTs. Both distributions are very similar to the integration performed with observed SST seen in figure 3.2(a), with the majority of storms originating from AEWs developing over the MDR, and clusters of storms in the Gulf of Mexico, Caribbean Sea and East of the American coast. The two CLIMSST integrations tend to form fewer storms (358) overall than the three equivalent domain, ERA forced simulations with observed SSTs (428, 392, 388). This difference is most marked for the MDR region. The fourth column in figure 3.15 shows the interannual variability of the number of TCs forming in the MDR, hurricanes and PDI*, while table 3.3 shows the individual correlations as well as the ensemble correlation between the observed and the simulated values of these three variables. It is interesting to note that some high activity years are very well captured by both simulations (1995, 2004), while others are not (1998, 2005). Conversely, the quiet TC period 1991-1994 is not at all reproduced in the CLIMSST ensemble. Since our previous ERA40 driven ensemble manages to capture these anomalous years relatively well, it suggests Atlantic SSTs had a particularly important impact on TC activity during these seasons.

---

5. Ideally, we would have performed additional simulations with climatological SSTs using the larger grid, but the computer resources available did not allow it.

The ensemble mean correlation (with observed values) indices for MDR TCs, HRs and PDI* are, respectively, 0.48, 0.28 and 0.48, significantly lower than the 0.77, 0.74 and 0.75 values from a three member ensemble of the small domain, ERA40 forced simulations employing observed SSTs (henceforth referred to as OBSSST ensemble). Comparison of the CLIMSST and OBSSST correlation coefficients suggests that interannual variations in Atlantic SSTs explain roughly 36% and 47% of the observed variance in simulated MDR TCs and HRs respectively. These values are relatively close to the 46% estimated (for both variables) by Saunders and Lea (2008) using a statistical model.

The last section of table 3.4 shows the linear trends for individual CLIMSST simulations and the ensemble mean trend for the three different variables. The upward trends seen with observed SSTs and ERA40 as LBCs are greatly reduced when climatological SSTs are used : the CLIMSST ensemble trends in MDR TCs, HRs and PDI* are, respectively, 50%, 22% and 32% of the ensemble mean. This reduction in the upward trend is accompanied by a reduced downward trend in vertical wind shear detected over a large portion of the MDR compared to previous ERA40 driven integrations (figure 3.17e). Although not shown, the changes in vertical wind shear (for an overlapping area) simulated with the small LAM using ERA40 LBCs and observed SSTs are similar to those of BIGLAMERA shown in figure 3.17b. In contrast to all the other ERA40 driven simulations, no upward trend in the intensity of the strongest TCs could be detected in the two CLIMSST runs (not shown). These results support the idea that most of the increase in Atlantic TC activity simulated for the last 30 years in the ERA40 driven integrations can be linked to changes in Atlantic SSTs. We infer this from the larger trends seen in the ERA-driven OBSSST ensemble compared to the CLIMSST ensemble. Based on these differences, we suggest the majority of the upward trend in the observed MDR TCs, HRs and PDI* is also primarily a result of Atlantic SSTs. Furthermore, figure 3.17 suggests that a trend of reducing wind shear over the tropical Atlantic has also contributed to the MDR TCs, HRs and PDI* upward trend, with part of this trend being due to local SSTs and remote factors. The lack of upward trend in the strongest storms in CLIMSST simulation compared to OBSST further suggests this trend arises primarily due to local SST influence and explain the disproportionately large decrease in PDI* and HRs from OBSSST to CLIMSST in table 3.4 compared to the MDR TC reduction, the former two being particularly sensitive to changes in intense TCs.

Removing Atlantic SSTs interannual variability also increases the impact of ENSO

over the MDR, as can be seen on figure 3.21, which shows correlation indices between mean annual Nino3.4 SST anomalies and JAS Atlantic GPI values. Since ENSO active region is largely located outside the domain of integration, the ENSO teleconnections are a prescribed atmospheric LBC in both OBSSST and CLIMSST. In both ensembles, changes in upper-level winds, associated with changes in the Walker circulation driven by ENSO, are responsible for the areas of significant correlations. El Niño increases subsidence and vertical wind shear, both detrimental to TCs, over the Atlantic. However, the increase in subsidence also increases short wave radiation at the surface, driving SSTs upward and offsetting some of the negative effect on TCs. By using climatological SSTs, we remove this teleconnection, which can explain why we measure stronger correlation between El Niño and GPI values over the MDR in CLIMSST.

3.6 Concluding Remarks

By comparing different integrations performed with a regional climate model set-up in a variety of configurations, we have shown that as the domain size increases, the impact of different LBCs on TC activity decreases. Regardless of boundary conditions, the results closest to observed climatology were obtained with a domain covering the entire tropical Atlantic and northern African region. The degradation in simulated TC activity detected in the smaller domains was linked in part to weak AEW activity in the pilot simulation and to stronger impact of biases inherited from the pilot, present in the large-scale fields, most notably relative humidity in the case of ERA40.

We then compared AEW activity in the different integrations and showed that all exhibited some level of activity in the 2.5-6 day range at 850 hPa. Mean wave intensity was seen to be influenced by many factors, including resolution and the distance over which the waves were allowed to develop at high resolution. Moreover, the ability of the model to properly resolve the AEJ also had an impact on intensity of the waves propagating in the southern track, with simulations exhibiting lower horizontal shear at the jet level associated with weaker wave activity. The ability of the model at resolving the jet was directly inherited from the pilot simulation. On the other hand, the total number of waves coming off the African coast did not, however, appear to be impacted by resolution.

We then evaluated the impact of LBCs on the ability of the model to capture observed

TC interannual variability. All ERA40 driven integrations were quite skillful at reproducing interannual changes in TC activity, in part because the changes in atmospheric fields driven by changes in SSTs over the tropical Pacific and tropical Atlantic were well captured in these simulations. For the smallest domain, compensating errors (weak AEWs vs high relative humidity), led to relatively accurate variability. Although the ERA-driven ensemble displayed the best correlation with observed activity, GEM driven integrations still managed to capture observed interannual variability with some level of skill, given that the mean AEW intensity level was sufficiently high to form TCs over the MDR. ERA40 driven simulations managed to somewhat capture the observed upward trend in Atlantic TC activity, whereas despite increasing Atlantic SSTs, none of the GEM driven integrations managed to reproduce this upward trend. We suggest that this failure is linked to the failure to reproduce a downward trend in vertical wind shear over the MDR in these simulations. Generally, Atlantic TC activity appears uncorrelated to AEW activity, as measured by 850 hPa variance, and western Sahel rainfall. The exception is the BIGLAMERA configuration, where AEW activity is observed to correlate positively with TC activity as well as the GPI over the MDR. In this case, changes in GPI values are primarily driven by changes in upper level zonal winds.

Finally, we compared simulations performed using observed and climatological SSTs. This CLIMSST ensemble managed to capture levels of interannual variability comparable to the GEM driven integrations, and, despite any trend in Atlantic SSTs, managed to produce a weak upward trend in TC activity due to a decrease in vertical wind shear over the MDR. El-Niño effect on TC activity also appears heightened in these integrations. We suggest this is because the ENSO teleconnection effect on Atlantic SSTs, which acts to counteract the negative effect of increased vertical wind shear, is removed.

A few of the results included here should act as a cautionary tale for climate simulations investigating future TC activity. First, a sufficiently high level of AEW activity is shown to be necessary to simulate a realistic distribution of Atlantic TC activity. Weaker waves will take longer to intensify and will form too far north, outside the MDR, causing SSTs at cyclogenesis to be biased-low. Moreover, there is evidence for an out-of-phase relationship between hurricanes forming south and north of $25°N$ (Gray, 1994). Thus, failure to simulate sufficient levels of AEW activity will potentially lead to an erroneous climate change signal. Secondly, we have shown that compensating errors can somewhat balance one another out and lead to a somewhat reasonable number of

TCs in a given configuration for the wrong reasons. One case here showed weak AEWs propagating into an atmosphere overly conducive to TC development due to very high relative humidity. Such errors likely induce an incorrect TC sensitivity to anthropogenic climate change, which will then lead to an incorrect projection of future TC activity in that particular configuration. Both of these issues were addressed here by extending the domain of integration to cover all of northern Africa as well as the tropical Atlantic.

Finally, good results with reanalyses do not guarantee good results with other LBCs. All RCM simulations performed using a low-resolution GEM integration as LBCs completely fail to predict, despite increasing local SSTs, an increase in Atlantic TC activity over the last $\sim$30 years. Similarly, the ability of the RCM to reproduce interannual variability is severly degraded, thus highlighting the crucial role played by atmospheric fields located outside the domain of integration and LBCs.

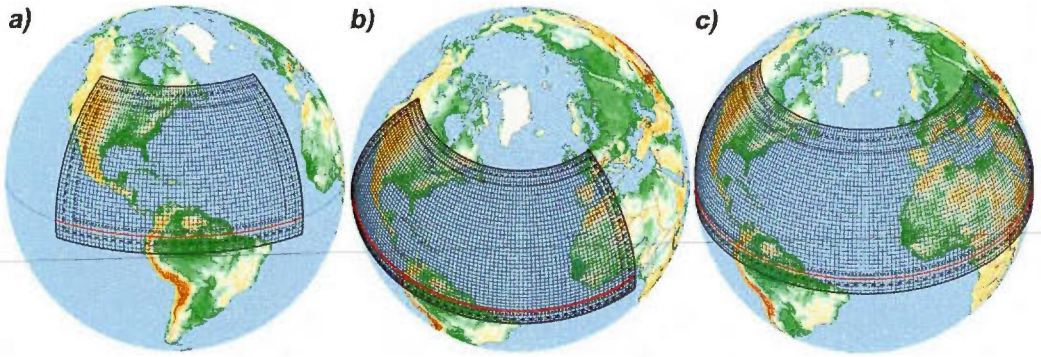

Figure 3.1 Different model configurations used in this study.

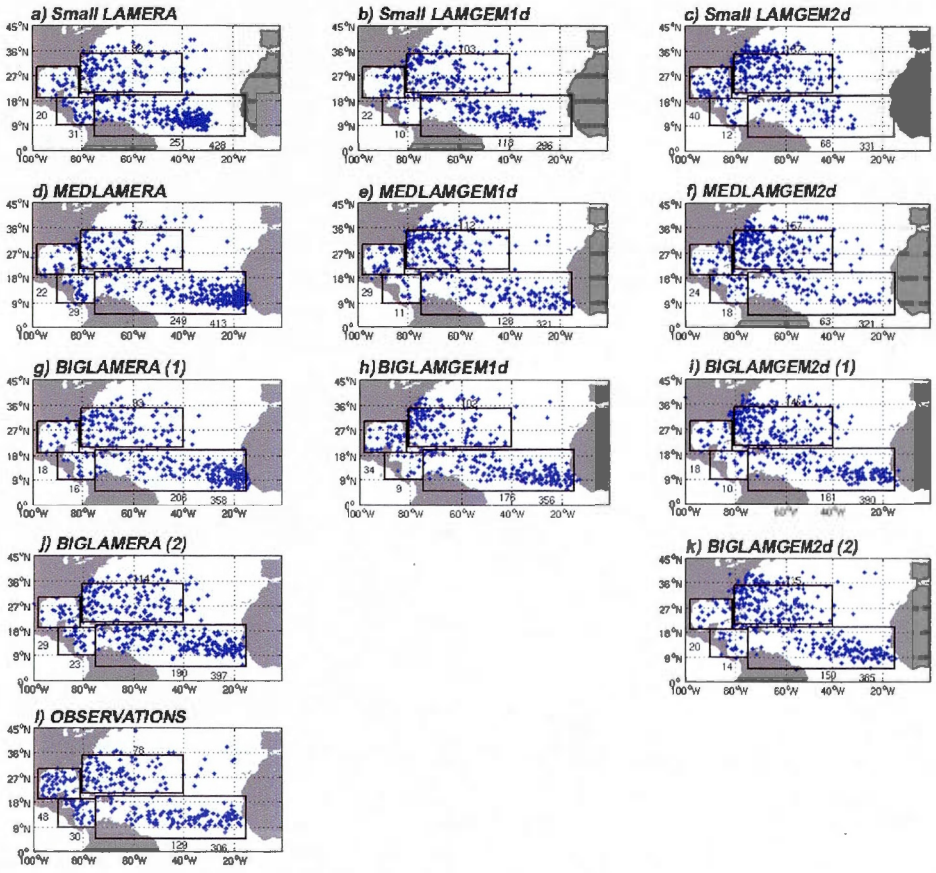

Figure 3.2 Locations where TCs are first detected in observations and simulations performed with the three different grids and three different sets of LBCs. The total number of storms is written at the bottom right, while the total number of storms included in each of the four rectangular boxes is written beside each one of them.

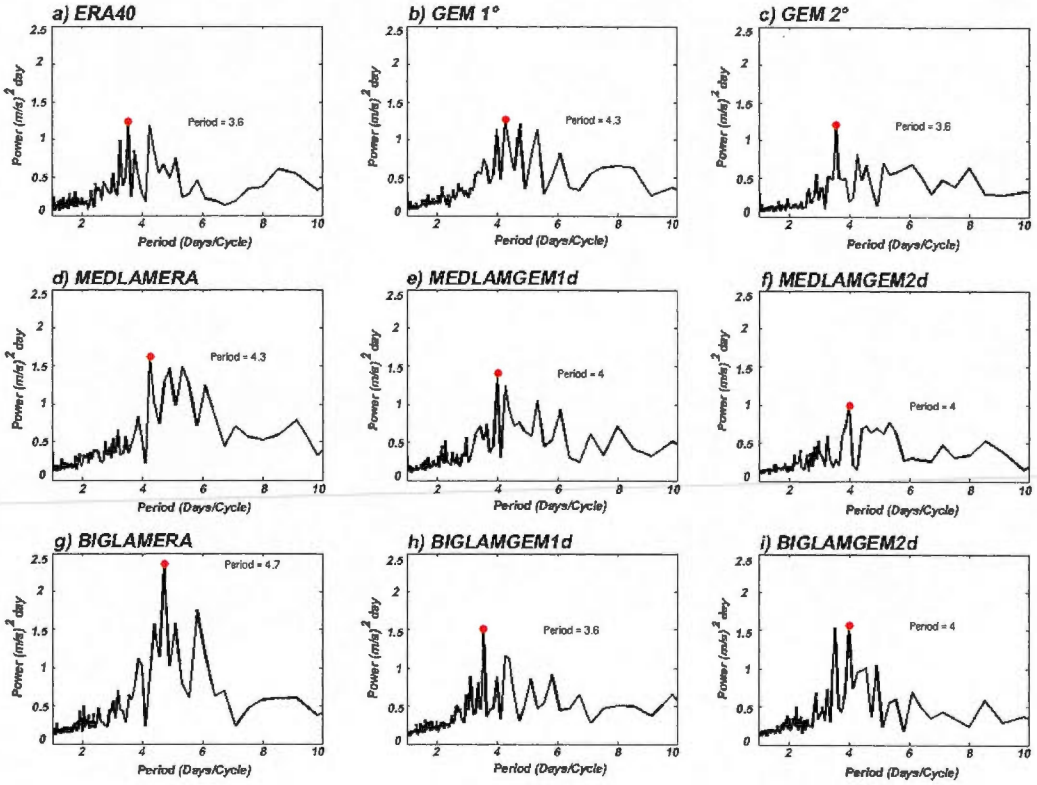

Figure 3.3 Mean power spectrum of 850 hPa meridional wind over the region limited by $8°N$, $12°N$, $17°W$ and $5°W$ during JJASO 1986 for ERA40 reanalysis and 8 GEM simulations. For each cases, the period with maximum amplitude is indicated.

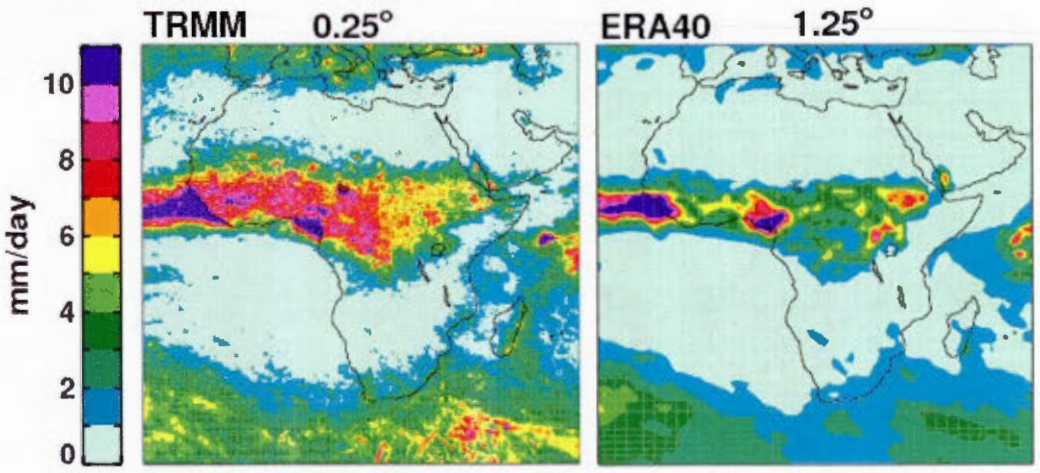

Figure 3.4 Comparison of mean (1998-2001) standard deviation for 2.5-6 day bandpass filtered JAS precipitations for TRMM satellite data and ERA40 reanalysis.

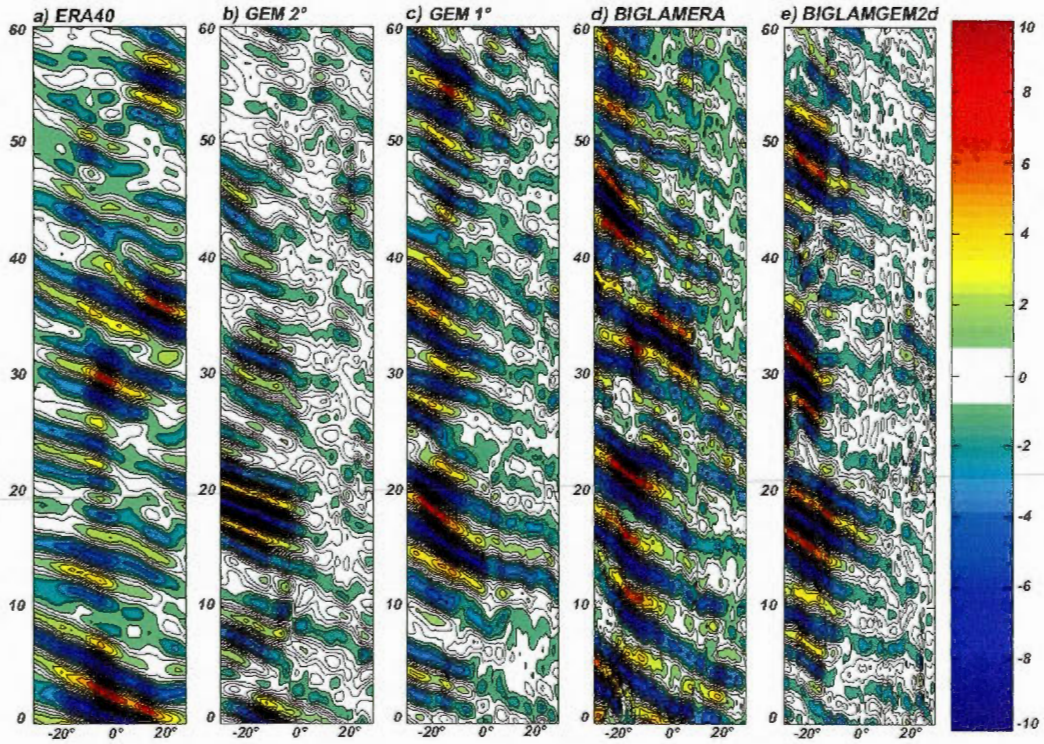

Figure 3.5 Hovmöller diagrams of $2.5 - 6$ day bandpass filtered 850 hPa meridional wind at $10°N$ between $30°W$ and $30°E$ for a) ERA40, b) GEM 2°, c) GEM 1°, d) BIGLAMERA and e) BIGLAMGEM2d. The vertical axis shows the days since August 1st, 1986. Units are $m\ s^{-1}$.

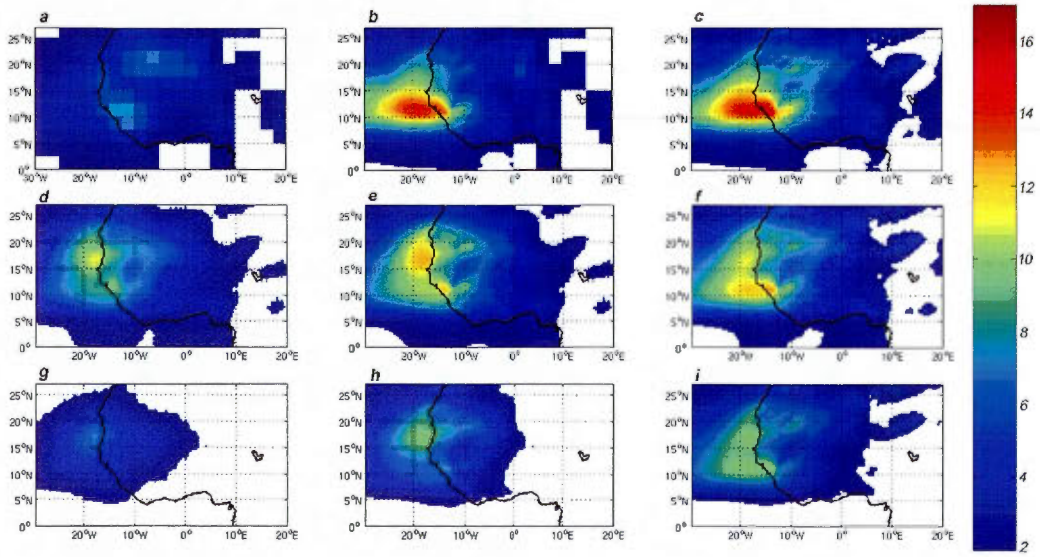

Figure 3.6 Mean 28-year variance of 2.5-6 day bandpass filtered 850 hPa meridional wind (during JJASO) for a) ERA40 reanalysis, b) MEDLAMERA, c) BIGLAMERA, d) GEM 1°, e) MEDLAMGEM1d, f) BIGLAMGEM1d, g) GEM 2°, h) MEDLAMGEM2d and i) BIGLAMGEM2d. Units are $m\ s^{-1}$ and only variance greater than $2m\ s^{-1}$ are shown. For the intermediate size grids, variance East of 0° is that of the pilot.

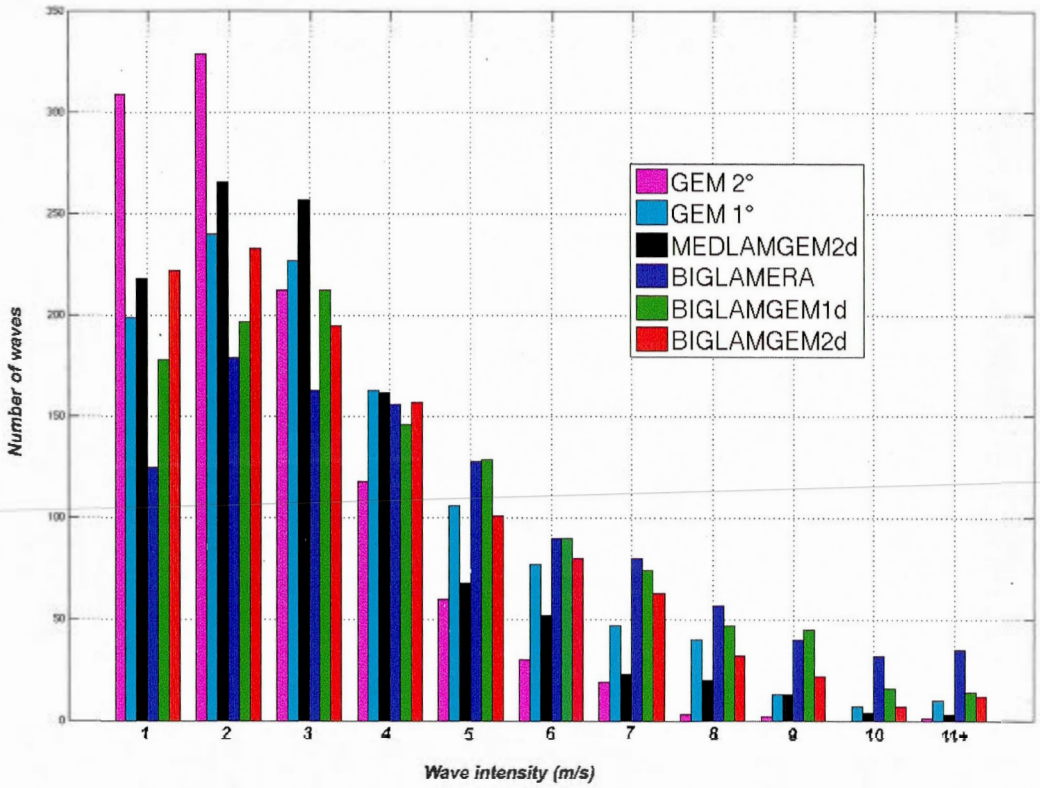

Figure 3.7 Intensity distribution of AEWs leaving the African coast between $11°N$ and $13°N$ based on filtered meridional wind speed, for the period JJASO 1979-2006. Units of x-axis are m/s. The last column includes all waves $> 10\ m/s$.

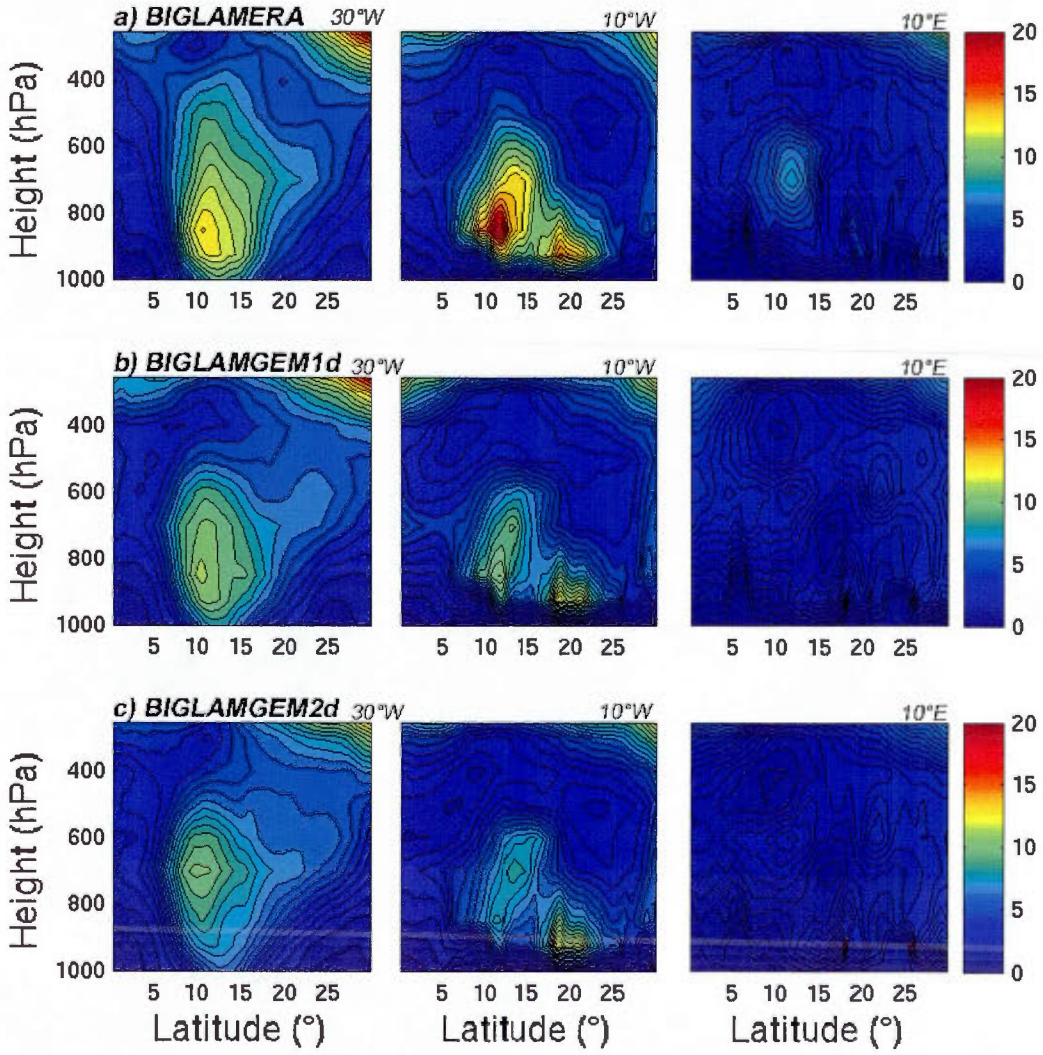

Figure 3.8 Meridional cross-section along $30°W$ (first column), $10°W$ (second column) and $10°E$ (third column) of the mean 2.5-6 days filtered August-September meridional wind variance for BIGLAMERA (first row), BIGLAMGEM1d (second row) and BIGLAMGEM2d (third row). Units are $m^2\ s^{-2}$.

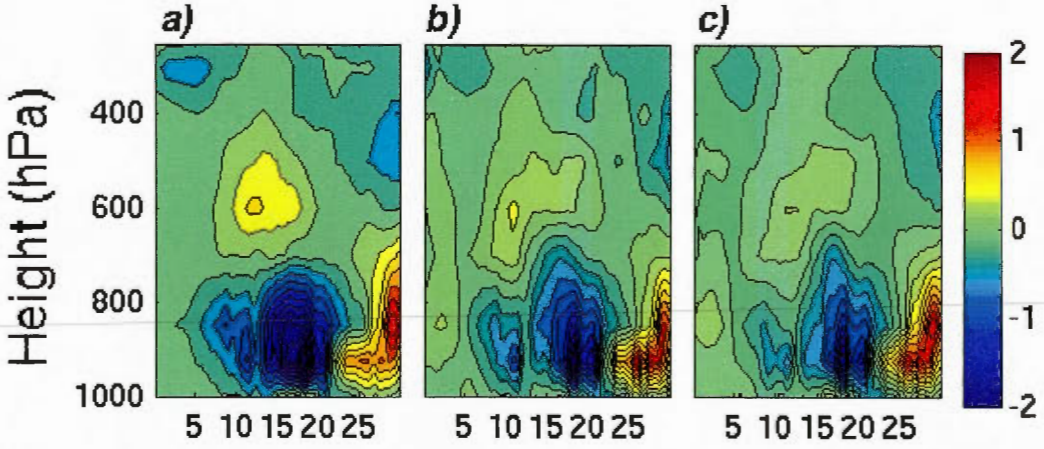

Figure 3.9 Meridional cross-section along $10°W$ of mean August-September covariances of 2.5-6 days filtered meridional wind and temperature for a) BIGLAMERA, b) BIGLAMGEM1d and c) BIGLAMGEM2d. Units are $K\ m\ s^{-1}$.

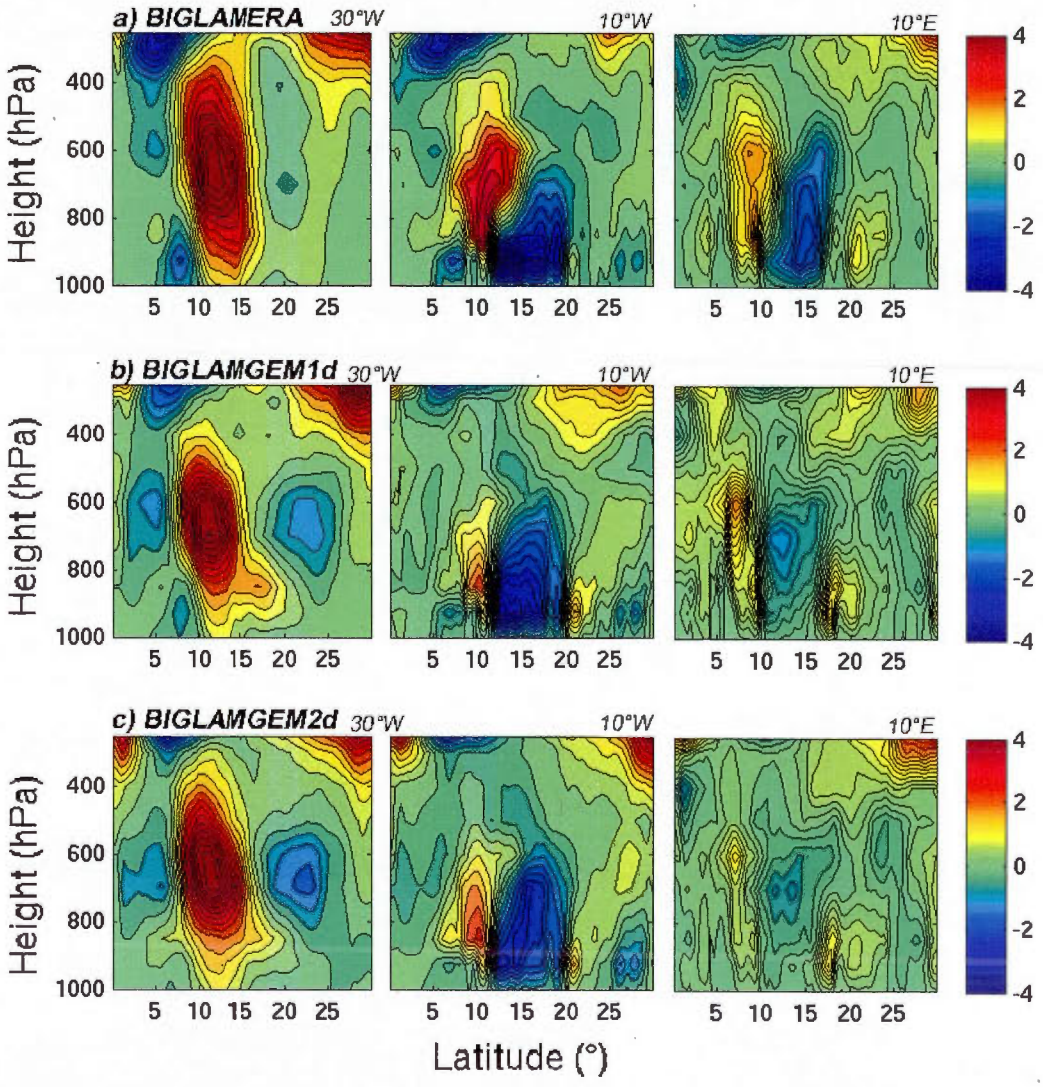

Figure 3.10 Meridional cross-section along $30°W$ (first column), $10°W$ (second column) and $10°E$ (third column) of mean August-September covariances of 2.5-6 days filtered meridional and zonal wind for BIGLAMERA (first row), BIGLAMGEM1d (second row) and BIGLAMGEM2d (third row). Units are $m^2\ s^{-2}$.

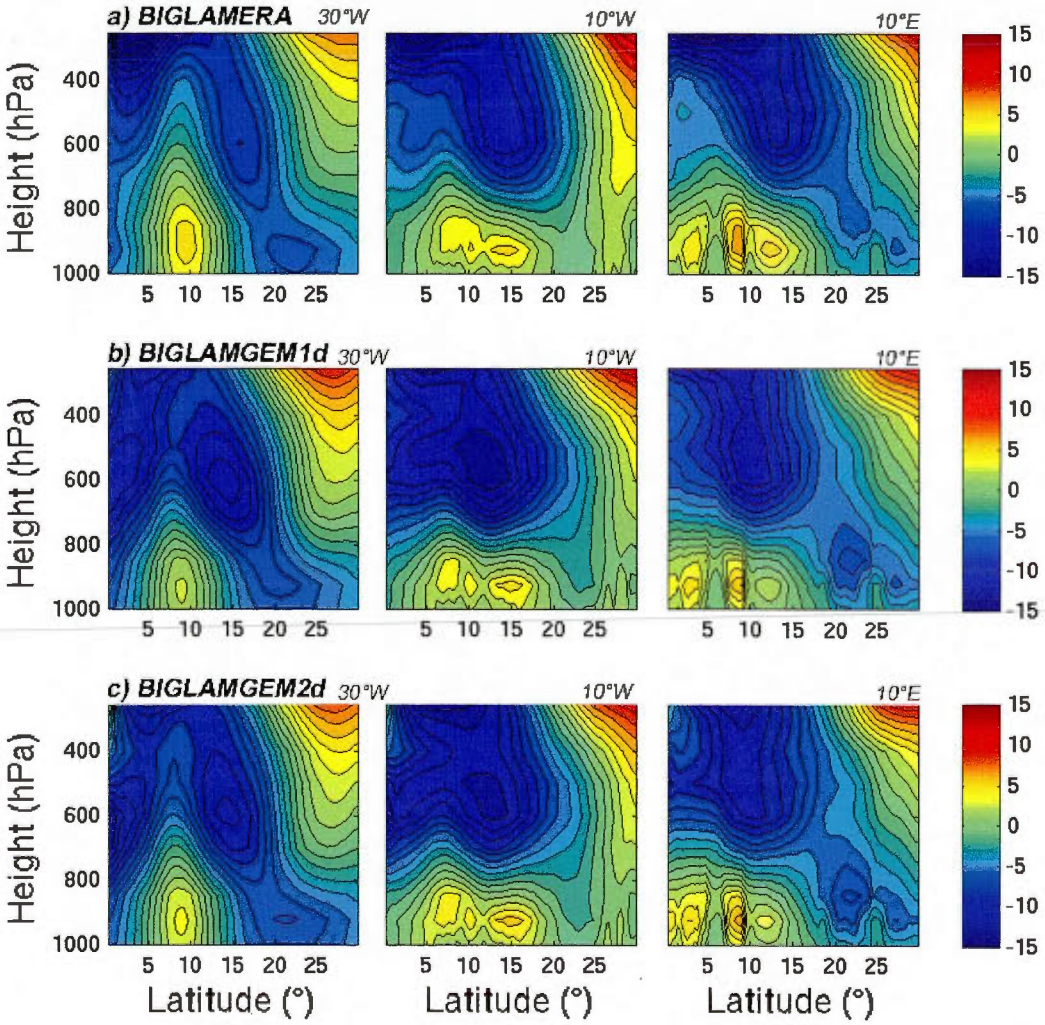

Figure 3.11 Meridional cross-section along $30°W$ (first column), $10°W$ (second column) and $10°E$ (third column) of mean August-September zonal winds for BIGLAMERA (first row), BIGLAMGEM1d (second row) and BIGLAMGEM1d (thrid row). Units are $m^2\ s^{-2}$.

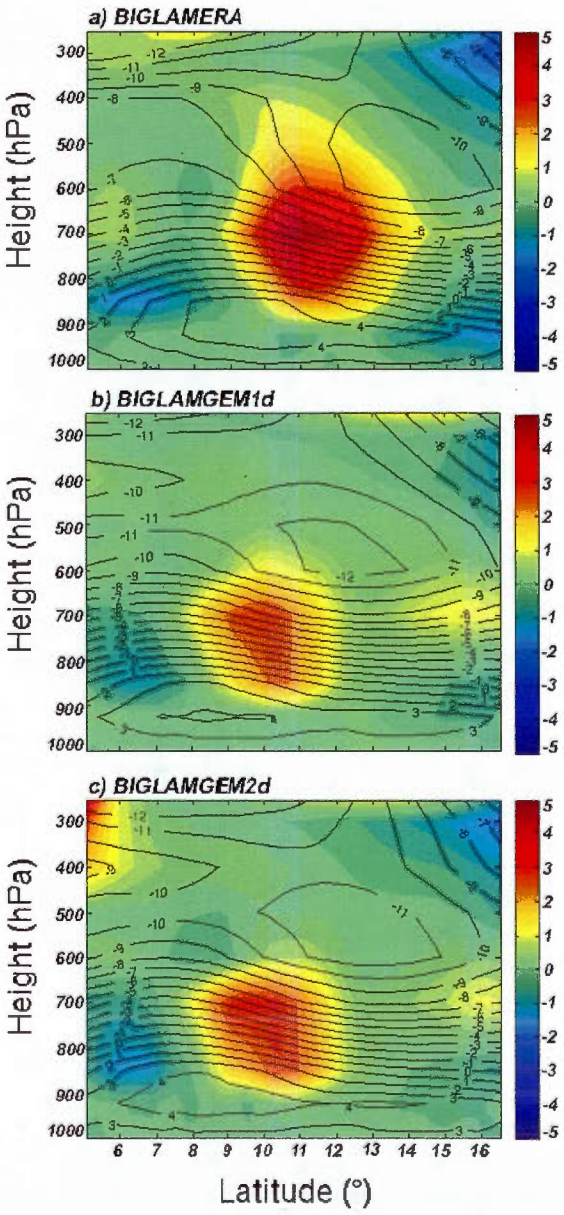

Figure 3.12 In color : Mean meridional cross-section of $-(u'v')\partial u/\partial y$ (main conversion term from zonal to eddy kinetic energy) between 0° and 20°W during August-September 1979-2006 for a) BIGLAMERA, b) BIGLAMGEM1d and c) BIGLAMGEM2d. Units are $10^{-5}m^2s^{-3}$. The black lines represent the mean zonal wind between 0° and 20°W during August-September 1979-2006 for the corresponding simulation.

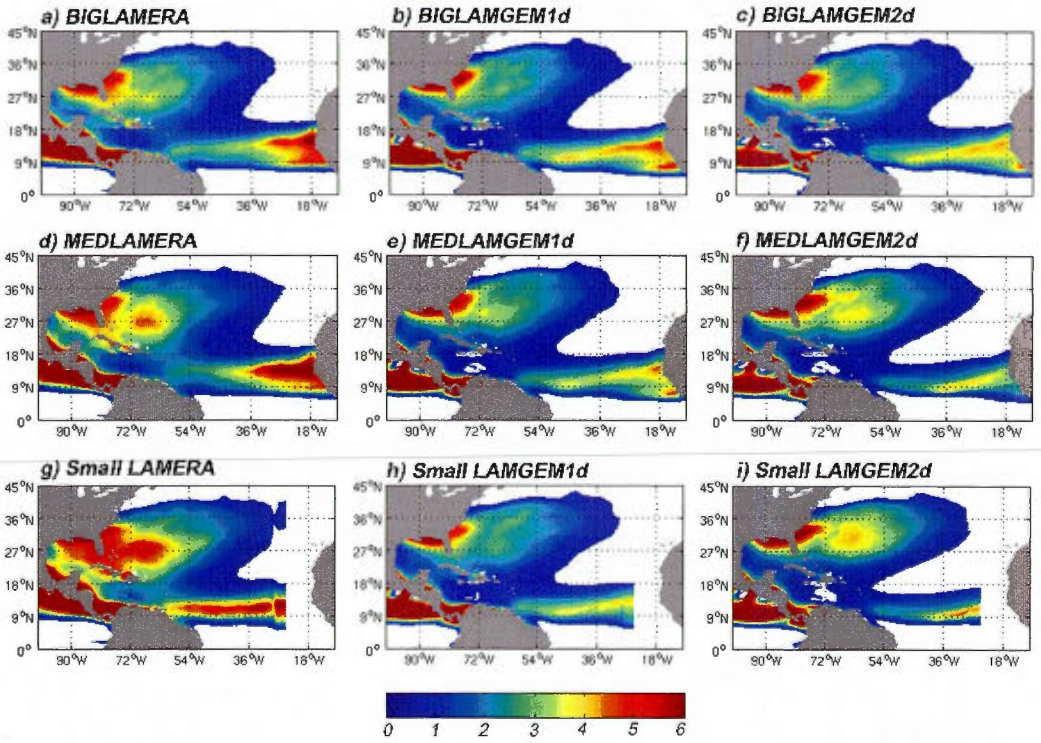

Figure 3.13 Mean ASO GPI values for 9 different simulations. First row is for large grid, second row, intermediate size grid, third row, small grid. First column is ERA40 LBCs, second column, GEM 1°, third column, GEM 2°.

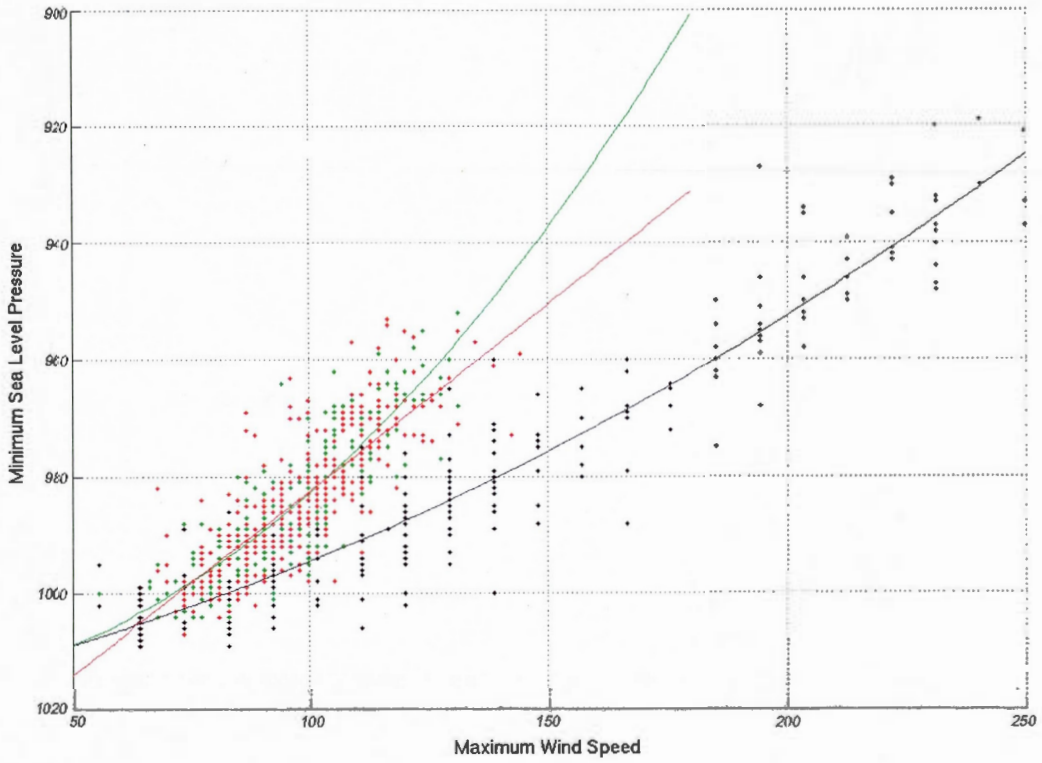

Figure 3.14 Relationship between minimum surface central pressure and TC maximum surface wind speed in GEM (green and red) and observations (black). Pressures are in hPa and winds in $km\ h^{-1}$.

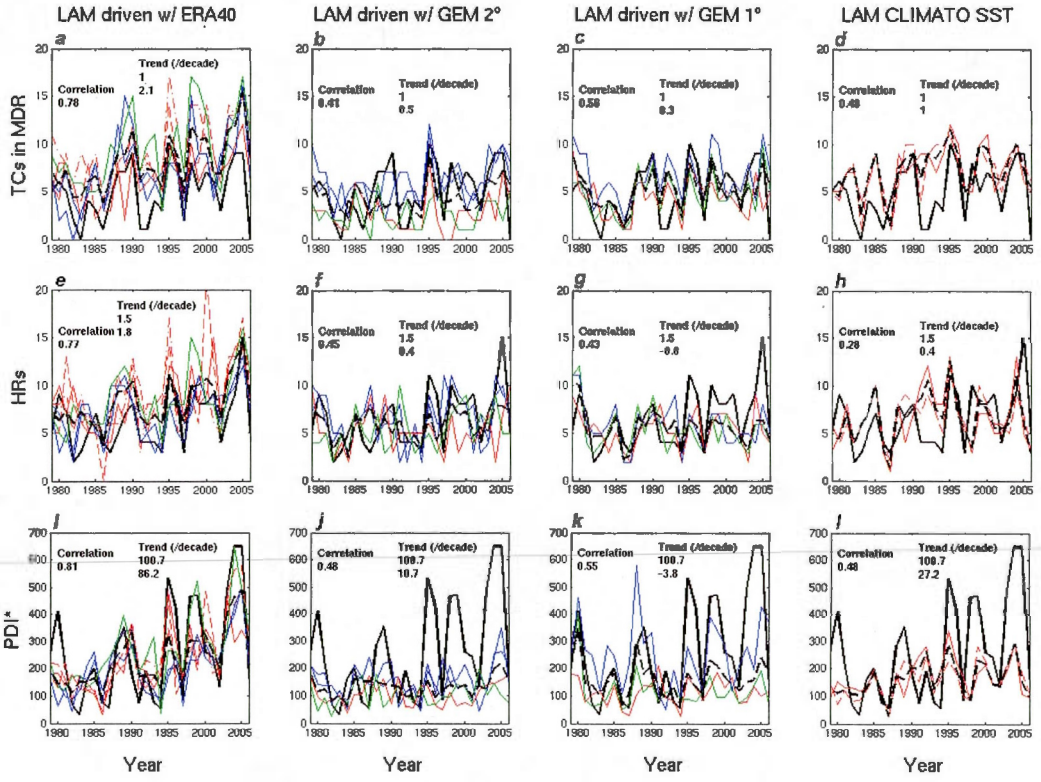

Figure 3.15 Interannual variability in TCs (first row), in hurricanes (second row) and PDI* (third row; in units of $10^9 m^3 s^{-2}$) for the June-November period, 1979-2006. The first colum is composed of ERA40 driven LAM simulations, the second column, GEM 2° driven LAM simulations, the third column, GEM 1° driven LAM simulations (all with observed, interannualy varying SST). The fourth column shows ERA40 driven LAM simulations using climatological (1979-2006) SST. The full black lines represent observations, the dashed black lines, the ensemble means, the red color, small LAM simulations, the green lines, intermediate LAM simulations and the blue lines, large LAM simulations. For each graph, correlation between the ensemble mean and observations is shown, as well as the observed and ensemble mean trends.

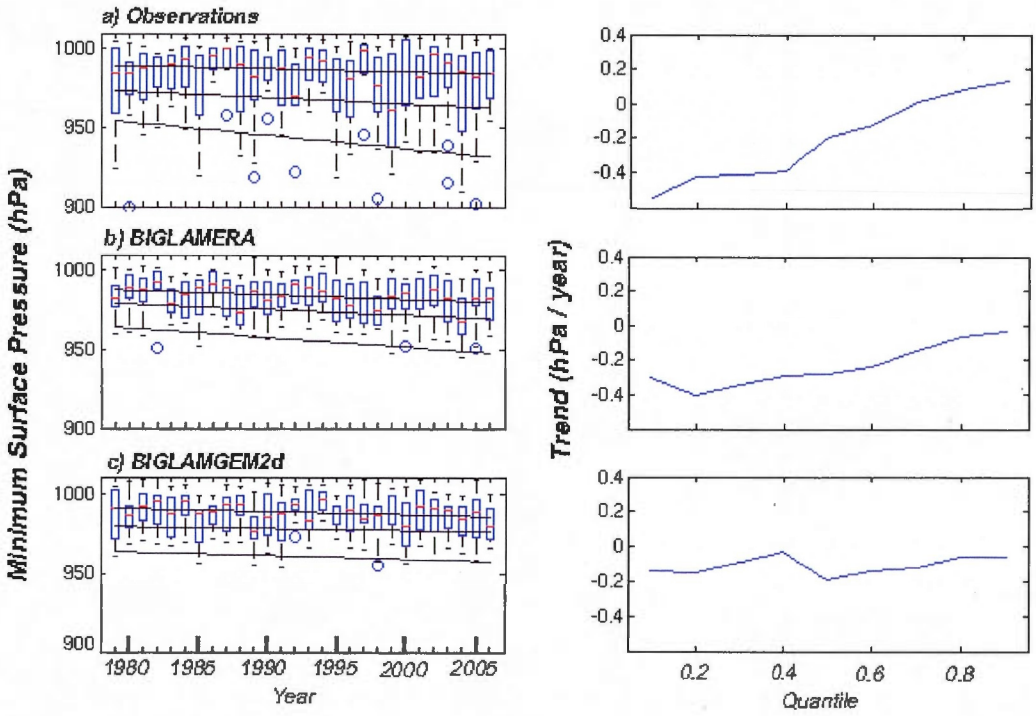

Figure 3.16 First column : Box plots, by year, of tropical cyclone lifetime-minimum surface pressures for a) observations, b) BIGLAMERA and c) BIGLAMGEM2d.Trend lines are shown for the median, 0.75 quantile, and 1.5 times the interquartile range. Second column : Trends in tropical cyclone lifetime-minimum surface pressure by quantile, from 0.1 to 0.9 in increments of 0.1, for a) observations, b) BIGLAMERA and c) BIGLAMGEM2d. Trends are in units of $hPa\ year^{-1}$.

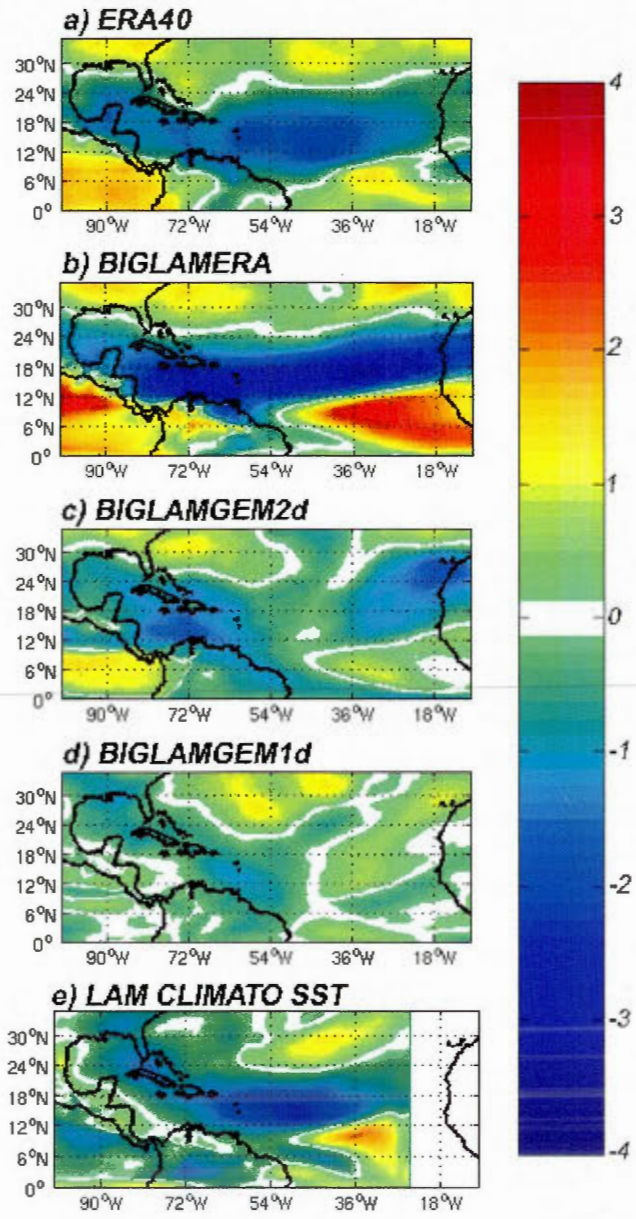

Figure 3.17 Trends in vertical wind shear over the Atlantic during the 1979-2006 period in a) ERA40 reanalysis and b) BIGLAMERA, c) BIGLAMGEM1d, d) BIGLAMGEM2d and e) LAM CLIMSST integrations. Units are $m\ s^{-1}/decade$.

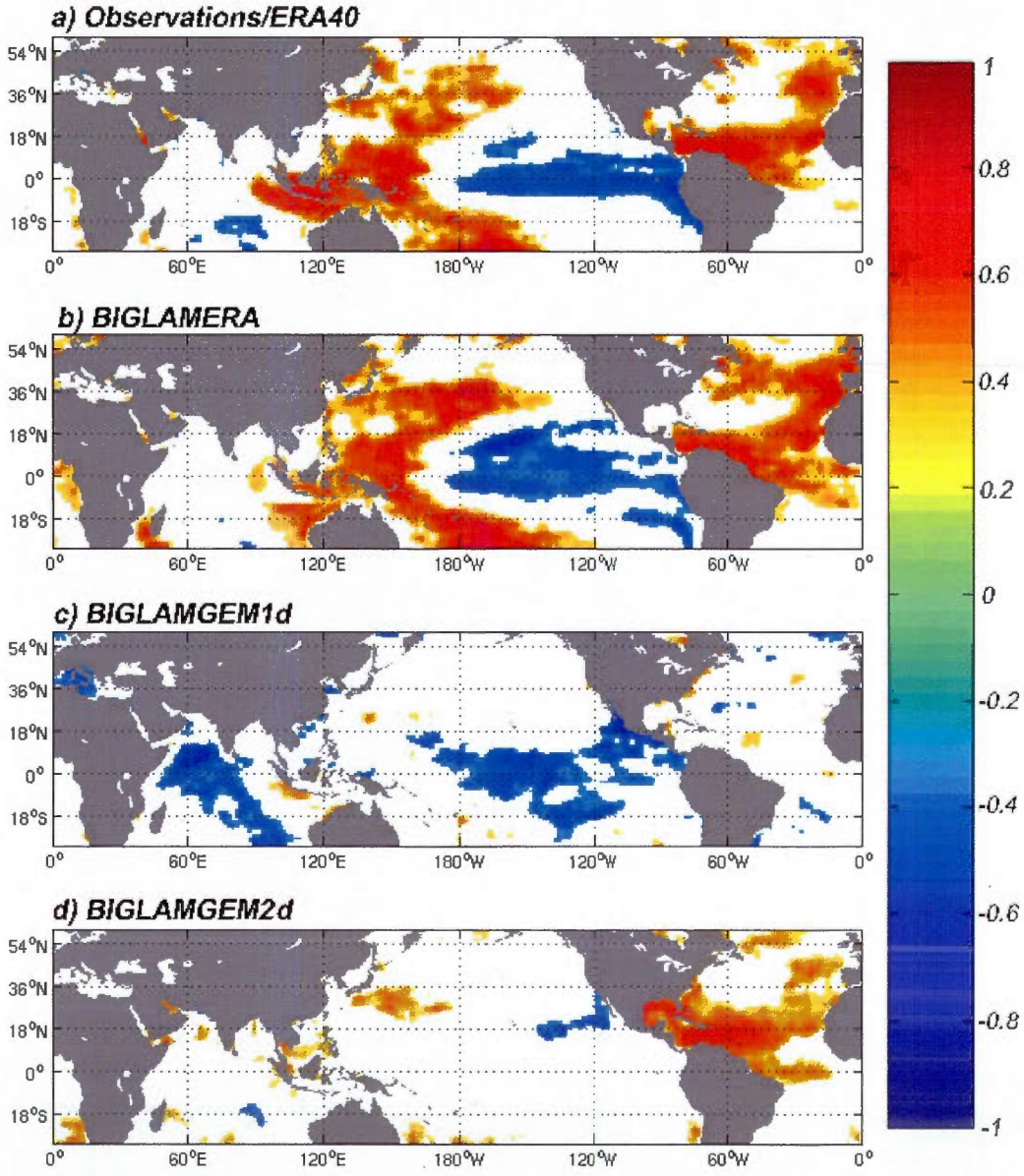

Figure 3.18 Correlation between JASO SSTs and yearly TCs forming over the MDR. Only correlations significant at the 90% level are shown.

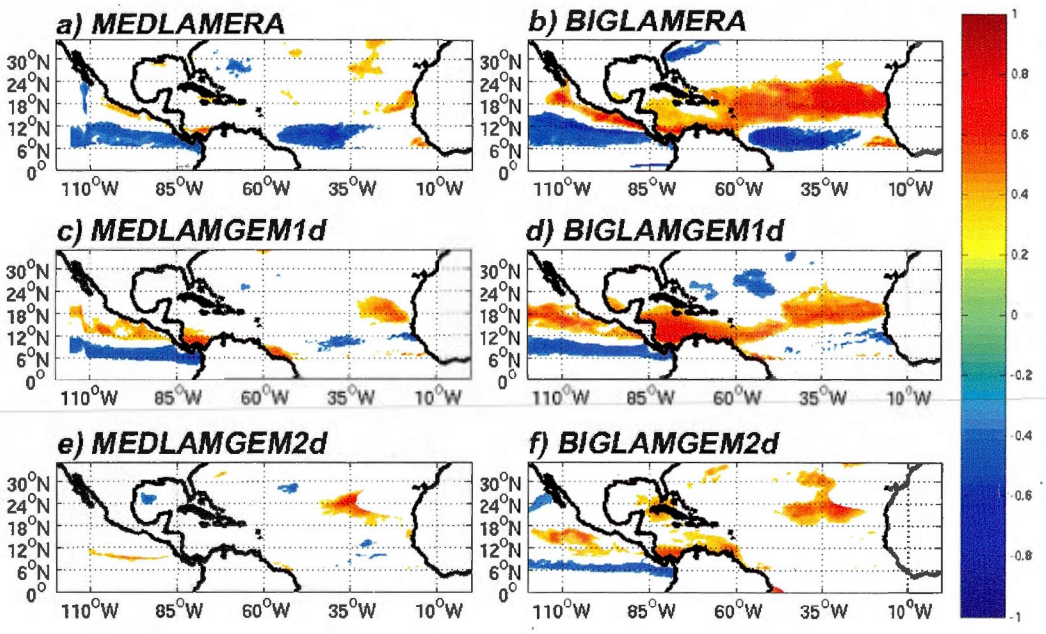

Figure 3.19 Correlation indices between mean variance of the JASO 2.5-6 day bandpass filtered meridional wind and GPI indices for 3 large grid and 3 intermediate size grid simulations. Only correlations significant at the 90% level over locations where the mean GPI value is greater than 0.5 are shown.

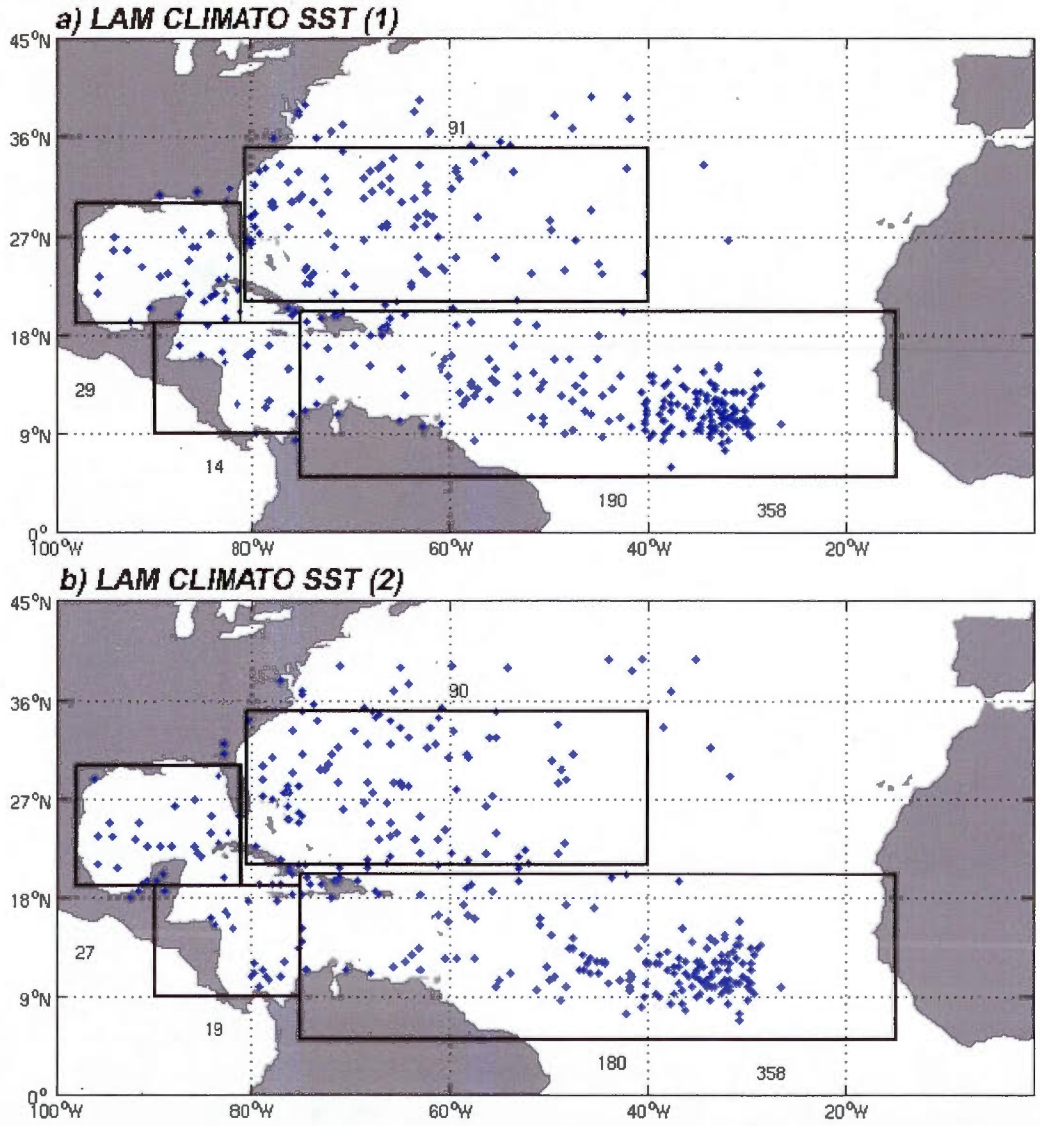

Figure 3.20 Cyclogenesis locations for two 28-year simulations integrated with climatological SSTs. The total number of storms is written at the bottom right, while the total number of storms included in each of the four rectangular boxes is written beside each one of them.

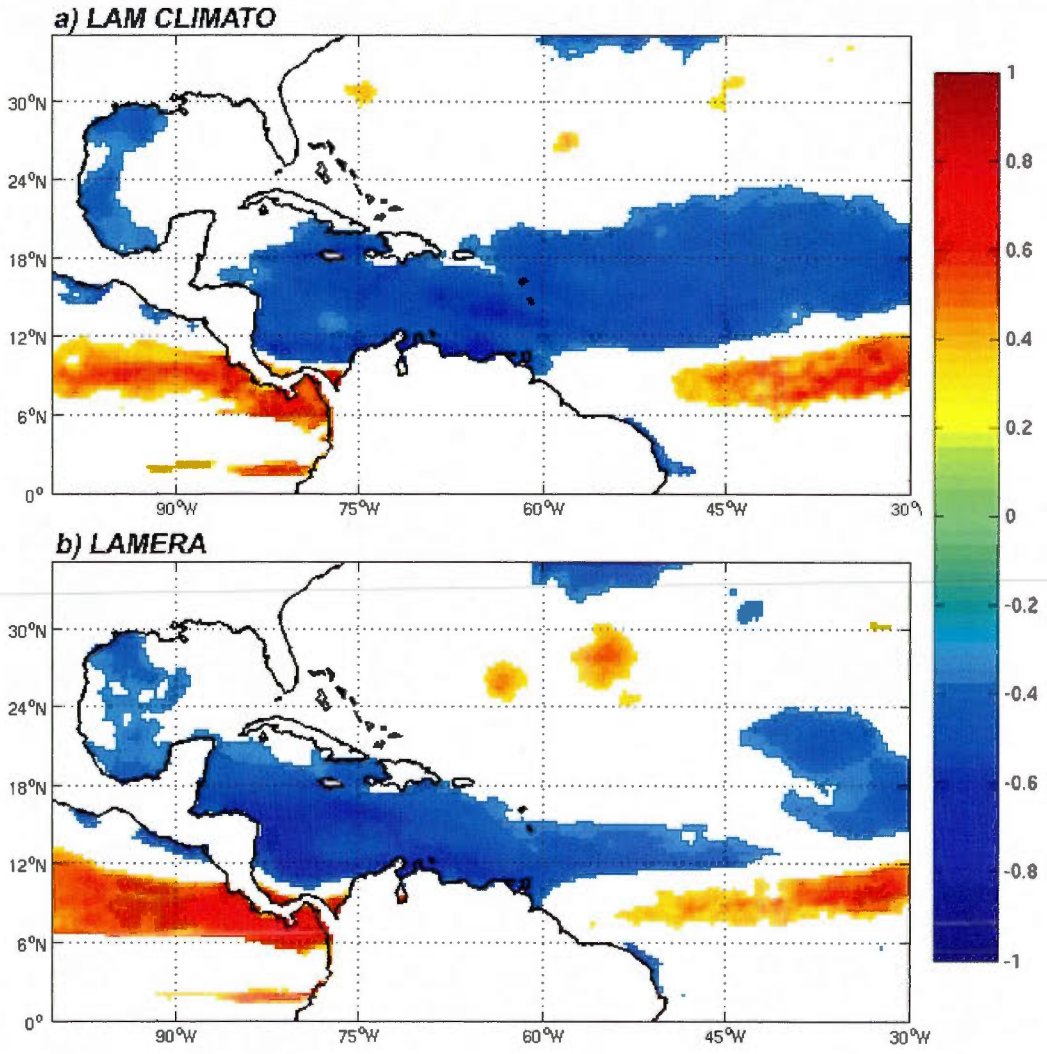

Figure 3.21 Correlations coefficients between mean annual SSTs during the JAS season over the Nino3.4 region and Atlantic GPI. Only values significant at the 90% level are shown.

Tableau 3.1 Mean maximum period in 850 hPa meridional wind power spectrum over the region limited by $8°N$, $12°N$, $17°W$ and $5°W$ for the period JJASO 1979-2006 (in days).

	Mean Period	St. Dev.
ERA40/ECMWF	4.0	0.8
Large LAM-ERA (1)	4.7	0.8
Large LAM-ERA (2)	4.7	0.6
Large LAM-GEM 2° (1)	4.5	1.0
Large LAM-GEM 2° (2)	4.3	0.5
Large LAM-GEM 1°	4.1	0.6
Intermediate LAM-ERA	4.7	0.7
Intermediate LAM-GEM 2°	4.4	1.2
Intermediate LAM-GEM 1°	4.0	0.8
GEM 2°	4.2	0.8
GEM 1°	4.3	0.5

Tableau 3.2 Total number of waves passing over $12°N$ and $16°W$ with filtered meridional wind speed greater than $0.5\ ms^{-1}$ for the period JJASO 1979-2006.

	Number of waves	Mean wave intensity ($m\ s^{-1}$)
ERA-40	1136	3.2
Large LAM-ERA	1085	4.5
Large LAM-GEM 2°	1124	3.5
Large LAM-GEM 1°	1147	4.0
Intermediate LAM-ERA	1086	4.3
Intermediate LAM-GEM 2°	1086	3.9
Intermediate LAM-GEM 1°	1142	3.1
GEM 2°	1083	2.5
GEM 1°	1129	3.5

Tableau 3.3 Correlation index between observed and simulated MDR TCs, hurricanes and PDI*.

	MDR TCs	HRs	PDI*
Small LAM-ERA	0.76	0.63	0.77
Small LAM-ERA *(Moon)*	0.58	0.54	0.68
Small LAM-ERA *(Moon-KFCP)*	0.68	0.73	0.67
Intermediate LAM-ERA	0.59	0.51	0.73
Large LAM-ERA (1)	0.59	0.66	0.67
Large LAM-ERA (2)	0.66	0.48	0.68
ERA40 driven Ensemble	**0.78**	**0.77**	**0.81**
Small LAM-GEM 2°	0.36	0.08	0.20
Intermediate LAM-GEM 2°	0.06	0.15	-0.02
Large LAM-GEM 2° (1)	0.33	0.44	0.43
Large LAM-GEM 2° (2)	0.44	0.45	0.54
GEM 2° driven Ensemble	**0.41**	**0.45**	**0.48**
Small LAM-GEM 1°	0.40	0.38	0.40
Intermediate LAM-GEM 1°	0.59	0.36	0.39
Large LAM-GEM 1°	0.44	0.35	0.48
GEM 1° driven Ensemble	**0.56**	**0.43**	**0.55**
Small LAM CLIMATO-SST (1)	0.43	0.16	0.32
Small LAM CLIMATO-SST (2)	0.45	0.39	0.57
CLIMATO-SST Ensemble	**0.48**	**0.28**	**0.48**

Tableau 3.4 Trends in observed and simulated MDR TCs, total hurricanes and PDI*. Units are *TCs/decade*, *HRs/decade*, $10^9 m^3 s^{-2}$/*decade*.

	MDR TCs	HRs	PDI*
Observations	**1.0**	**1.5**	**100.7**
Small LAM-ERA	1.6	1.4	81.6
Small LAM-ERA *(Moon)*	2.8	2.5	113.8
Small LAM-ERA *(Moon-KFCP)*	1.3	1.9	79.0
Intermediate LAM-ERA	2.2	2.0	100.6
Large LAM-ERA (1)	1.8	1.3	68.4
Large LAM-ERA (2)	2.6	1.5	73.6
ERA40 driven Ensemble	**2.1**	**1.8**	**86.2**
Small LAM-GEM 2°	0.3	0	6.5
Intermediate LAM-GEM 2°	0.3	0.9	8.9
Large LAM-GEM 2° (1)	1.0	0.5	13.8
Large LAM-GEM 2° (2)	0.5	0.2	13.8
GEM 2° driven Ensemble	**0.5**	**0.4**	**10.7**
Small LAM-GEM 1°	-0.1	-0.1	1.5
Intermediate LAM-GEM 1°	0.7	-0.8	-16.5
Large LAM-GEM 1°	0.2	-0.8	3.7
GEM 1° driven Ensemble	**0.3**	**-0.6**	**-3.8**
Small LAM CLIMATO-SST (1)	0.9	0.5	19.6
Small LAM CLIMATO-SST (2)	1.1	0.3	34.8
CLIMATO-SST Ensemble	**1.0**	**0.4**	**27.2**

Tableau 3.5 Correlation index between MDR TCs, hurricanes, PDI* and 1) bandpass filtered meridional wind variance and 2) JAS precipitation over the Sahel region. Values significant at the 95% level based on the student-t test are in bold.

	MDR TCs	HRs	PDI*
Observations	0.09 / 0.15	0.21 / 0.12	0.26 / 0.27
Small LAM-ERA	0.19 / 0.30	-0.09 / 0.11	-0.12 / 0.20
Small LAM-ERA *(Moon)*	-0.13 /0.14	-0.10 / 0.06	-0.11 / 0.15
Small LAM-ERA *(Moon-KFCP)*	-0.07 /0.06	-0.09 / 0.11	-0.01 / 0.33
Small LAM-GEM 1°	0.09 / -0.22	-0.02 / -0.12	0.02 / 0.14
Small LAM-GEM 2°	0.28 / 0.34	-0.22 / 0.35	-0.16 / 0.16
Intermediate LAM-ERA	0.17 / 0.06	0.19 / 0.02	0.18 / 0.02
Intermediate LAM-GEM 1°	0.02 /0.16	0.21 / 0.12	0.08 / 0.04
Intermediate LAM-GEM 2°	-0.06 / 0.10	0.13 / -0.05	0.01 / 0.14
Large LAM-ERA (1)	**0.52** / **0.38**	**0.46** / **0.43**	**0.60** / **0.44**
Large LAM-ERA (2)	**0.50** / **0.47**	**0.66** / **0.67**	**0.58** / **0.55**
Large LAM-GEM 1°	0.22 / -0.02	0.24 / 0.23	**0.47** / 0.12
Large LAM-GEM 2° (1)	0.23 / 0.14	0.37 / 0.09	0.33 / -0.06
Large LAM-GEM 2° (2)	0.25 / 0.25	0.16 / 0.07	0.11 / 0.06
Small LAM CLIMATO-SST (1)	0.23 / 0.36	0.10 / 0.01	0.08 / 0.15
Small LAM CLIMATO-SST (2)	0.12 / 0.29	**0.38** / 0.03	0.19 / 0.33

Tableau 3.6 Correlation between observed GPCP JAS precipitation and simulated precipitation over the Western Sahel region.

Large LAM-ERA (1)	0.33
Large LAM-ERA (2)	0.44
Large LAM-GEM 2° (1)	0.32
Large LAM-GEM 2° (2)	0.29
Large LAM-GEM 1°	0.18
Intermediate LAM-ERA	0.31
Intermediate LAM-GEM 2°	0.08
Intermediate LAM-GEM 1°	0.24
GEM 2°	-0.04
GEM 1°	0.31

CONCLUSION

En guise de conclusion, nous ferons un bref retour sur les résultats obtenus et ferons ensuite un travail de prospective en mettant l'emphase sur la suite à donner aux travaux présentés ici. D'abord, la première partie de la thèse a permis de contourner les limites imposées par la basse résolution des modèles de circulation générale (MCG) et d'étudier des phénomènes de petites échelles (comparativement à la résolution des MCG), les cyclones tropicaux, au travers des champs atmosphériques favorables à leur formation. Au travers de deux indices de cyclogénèse, nous avons pu établir une bonne correspondance entre ceux-ci et la distribution observée des cyclones, tant dans les réanalyses que dans un ensemble de simulations produites par des modèles couplés. Suite à une analyses du climat présent et du passé récent (XXe siècle), nous avons analysé la valeur des indices projetés par l'ensemble de MCG. Dans cet ensemble, l'indice que nous avons jugé le plus fiable, le CYGP, projète une légère augmentation dans le Pacifique Ouest, près du Japon et du continent asiatique. Ces résultats sont supportés par une analyse semblable effectuée par Vecchi et Soden (2007).

La deuxième partie a permis de mettre en évidence pourquoi nous avons eu recours aux indices de cyclogénèse dans la première partie et a servi à évaluer la capacité du modèle régional de climat canadien à simuler les cyclones tropicaux dans l'Atlantique ainsi qu'à évaluer l'impact d'un changement de résolution et de conditions aux frontières sur cette capacité. Outre Hernández-Díaz (2001) qui s'est penchée sur l'énergie des ondes africaines en utilisant la troisième version du MRCC (MRCC3), cette étude est la première à étudier les cyclones tropicaux simulés par le MRCC. Comme nous avons pu le constater, les simulations à plus basses résolutions (1°, 2°) démontrent des lacunes dans leur représentation des tempêtes cycloniques (d'où l'utilisation des indices de cyclogénèse pour les MCG de la partie précédente). Cependant, lorsque la résolution du modèle est augmentée à $\sim 30\ km$, l'activité cyclonique devient beaucoup plus réaliste, en particulier en terme du nombre total de tempêtes simulées et de leur distribution géographique. De même, la distribution saisonière, avec un maximum observé durant la période août-septembre-octobre, correspond bien à la saison des ouragans tel qu'observée dans l'Atlantique. Des déficiences en terme d'intensité ont été remarquées, le

modèle ne produisant pas de vents maximum d'intensité 2 à 5 sur l'échelle de Saffir-Simpson. Cette lacune a été associée à la résolution du modèle, qui est encore insuffisante pour bien simuler le coeur de la tempête où les vents maximum sont observés, et à un paramétrage inadéquat des échanges de quantité de mouvement entre l'ouragan et les océans.

En mode à aire limitée (LAM), le modèle piloté par des réanalyses présente une distribution géographique des cyclones tropicaux qui est relativelement fidèle à la réalité. De plus, le modèle arrive à bien reproduire la variabilité interannuelle observée durant les 28 ans à l'étude. En ce sens, les performances du MRCC5 se comparent (parfois avantageusement) aux quelques autres modèles utilisés pour étudier l'activité cyclonique dans l'Atlantique. Par exemple, l'indice de corrélation pour le nombre total de cyclones obtenu par un ensemble composé de deux membres du modèle atmosphérique du Geophysical Fluid Dynamics Laboratory (GFDL), couvrant la période 1980-2005, est de 0.74 (Knutson et al., 2007). Avec le MRCC5, l'indice obtenu avec un ensemble de cinq membres est de 0.78. Il est important de souligner que l'étude du GFDL incluait une forme de « nudging » spectral, ce qui n'était pas le cas avec le MRCC5. En ce sens, les champs atmosphériques sont davantage forcés par le pilote dans le domaine d'intégration comparativement aux champs du MRCC5, ce qui rend l'indice de corrélation de 0.78 du MRCC5 encore plus remarquable.

La capacité du modèle à reproduire la variabilité interannuelle vient, entre autres, de sa capacité à reproduire l'impact du « El Niño Southern Oscillation » (ENSO) sur les cyclones tropicaux. Comme nous l'avons discuté au chapitre 3, les changements de température dans le Pacifique forcent des changements dans les champs atmosphériques au-dessus de l'Atlantique, qui ont alors un impact sur la formation des cyclones tropicaux dans ce bassin. Les années El Niño (La Niña) sont généralement associées à des années plus tranquilles (actives). Le LAM piloté par ERA40 arrive à bien reproduire cet impact, de même que le MRCC5 en mode résolution variable (GVAR). À cause d'une mauvaise représentation de l'impact d'ENSO dans la simulation à basse résolution, les résultats avec le LAM piloté par GEM 2° et GEM 1° sont moins concluants. Bien que nous n'avons pas investigué cet aspect d'avantage, il est probable que cela soit une conséquence d'une dégradation de la circulation de Walker dans les simulations à plus basses résolutions.

La troisième partie de la thèse a démontré l'importance de simuler le climat dans la partie nord du continent african (région du Sahel) à haute résolution. Dans cette région se développent et se propagent les ondes d'Est africaines qui sont à l'origine d'une grande partie des ouragans qui se forment dans l'Atlantique. Des ondes de faible intensité dans les simulations à basses résolutions requièrent trop de temps pour s'intensifier au-dessus de l'Atlantique ou n'arrivent tout simplement pas à se développer. Cela amène un changement dans la distribution géographique de la cyclogénèse du bassin Atlantique simulée par le modèle, transférant ainsi un nombre important de tempêtes des tropiques aux sous-tropiques. Cet effet a aussi été détecté dans le modèle français ARPÈGE (Chauvin, 2011 ; communication personelle). Une telle configuration produit non-seulement une distribution erronée de la cyclogénèse, mais mènerait aussi toute tentative d'évaluation de l'impact des changements climatiques sur les ouragans à une conclusion toute aussi erronée.

Ce dernier résultat est particulièrement pertinent suite à la mise sur pied du projet international CORDEX (COordinated Regional climate Downscaling EXperiment) [6], dont le but est d'utiliser différentes techniques de « downscaling » dynamique et statistique afin d'évaluer l'impact des changements climatiques dans plusieurs régions du globe. L'un des objectif du projet est d'utliser la haute résolution afin d'évaluer l'impact des changements climatiques sur les cyclones de l'Atlantique. Cependant, en utilisant, comme ils entendent le faire, une grille qui ne couvre que l'Atlantique et l'Amérique Centrale (une grille semblable à notre plus petite grille), les résultats obtenus ici laissent présager que cette configuration sera inadéquate et que les intégrations qui en résulteront ne permettront pas d'éclaircir le lien entre changements climatiques et ouragans.

La faible intensité des ondes d'Est africaines dans certaines simulations a été liée, en partie à la faible résolution de certaines simulations, mais aussi à une mauvaise simulation du courant-jet d'Est africain. La mauvaise représentation de ce courant jet a aussi été liée à l'influence du pilote qui, à plus basse résolution, ne le simulait pas adéquatement. Cette lacune est surtout visible pour les ondes se propageant au sud du jet, ces instabilités utilisant le cisaillement horizontal du vent pour croître et se propager au-dessus du Sahel. Les ondes se propageant au nord du jet semblaient peu affectées, mais celles-ci ont un impact très limité sur la cyclogénèse de l'Atlantique.

---

6. Pour plus d'information : www.meteo.unican.es/en/projects/CORDEX

Finalement, dans cette troisième partie, nous avons aussi démontré l'importance des conditions aux frontières en montrant que le MRCC5 arrivait à reproduire l'augmentation observée au cours des 30 dernières années seulement lorsque celui-ci est piloté par les réanalyses de ERA40. Cette augmentation de l'activité est liée à l'augmentation du nombre de tempêtes dans les tropiques, près de la côte Ouest de l'Afrique de même qu'une augmentation de l'intensité des tempêtes les plus puissantes, conséquence probable d'une tendance à la baisse du cisaillement vertical au-dessus du bassin Atlantique. L'incapacité du modèle à simuler une baisse du cisaillement vertical au-dessus de l'Atlantique lorsque piloté par GEM à basse résolution l'empêche de reproduire le changement d'activité observé lors des $\sim$ 30 dernières années (et ce malgré l'augmentation de température de la surface de l'Atlantique). Ces derniers résultats montrent l'importance de bien représenter les changements qui s'opèrent à l'extérieur même du bassin Atlantique de même que les liens qui existent entre les différentes régions du globe et mettent en évidence un obstacle de plus à contourner afin de projeter les changements probables d'ouragans dans le bassin de l'Atlantique.

Avant de terminer, nous ferons maintenant un survol de différents projets qui pourraient découler de cette thèse, certains dans le cadre d'un projet de maîtrise, d'autres dans le cadre d'un projet doctoral.

Prospective

Les résultats encourageants obtenus en mode résolution variable devraient nous inciter à considérer la possibilité de tenter des prédictions saisonnières à l'aide du MRCC5. Les prédictions saisonnières d'ouragans ont d'abord été dérivées à partir des saisons passées, i.e. que le nombre de tempêtes prédites étaient dérivées à partir des statistiques des années précédentes qui présentaient des charactéristiques atmosphériques semblables à l'année en cours. Avec l'augmentation de la puissance de calcul, on a vu récemment apparaître des prédictions saisonières dynamiques où l'on produit, à l'aide d'un modèle de climat, un ensemble de simulations pour la saison en cours et où les statistiques (nombre de tempêtes tropicales, ouragans, PDI, ...) compilées à partir de cet ensemble servent de prédictions. Une telle entreprise demanderait une puissance de calcul au-delà des capacités actuelles de l'UQAM, mais que l'arrivée de COLOSSE (CLUMEQ) rend

sans doute possible. Cela permettrait au groupe MDCR de rentrer dans le club sélect des quelques centres de recherche à effectuer des prédictions saisonnières d'ouragans, prédictions qui bénificient souvent d'une grande visibilité.

Toutes les simulations produites pour de cette étude couvrent la période 1979-2006. La capacité du modèle à développer une climatologie réaliste de cyclogénèse pour le climat présent devrait aussi nous encourager à nous tourner vers l'avenir. Il est certain que l'impact du réchauffement climatique sur les ouragans est d'un intérêt certain, surtout pour les populations vulnérables amassées le long de la côte Est américaine, du Golfe du Mexique et des provinces maritimes. La montée prévue du niveau de la mer lors des prochaines décennies ne fera qu'exacerber l'impact anticipé d'une augmentation en intensité des cyclones sur ces populations. Si les données de conditions aux frontières deviennent disponibles (dans le cadre du 5e rapport du GIEC par exemple), il serait intéressant d'évaluer la réponse d'ensemble du MRCC5 lorsque celui-ci est piloté par une série de modèles pour une période future, par exemple 2080-2100. On pourrait alors comparer les statistiques annuelles (durée de la saison, intensité, nombre de tempêtes, distribution géographique) du climat présent et futur et ainsi estimer la réponse à une augmentation des GES.

Comme mentionné en introduction, près de 500 saisons d'ouragans ont été simulées pour cette étude. Les domaines de simulation couvraient la majeure partie de l'Atlantique, mais aussi une partie de l'océan Pacifique, i.e. une grande partie du Pacifique Nord-Est. En moyenne, cette région est la deuxième plus active après le Pacific Nord-Ouest en terme de cyclones tropicaux. Faire une évaluation de cette région était en dehors du cadre de cette étude et donc aucune analyse de cyclones n'aura été faite ici. Il serait très raisonable de penser que l'analyse de ces données s'inscrirait facilement dans un projet de maîtrise, compte tenu du fait que 1) les simulations ont déjà été effectuées et 2) le programme informatique pour détecter et suivre les cyclones est opérationel. Plusieurs questions pourraient être abordées. D'abord, de tous les bassins où les cyclones tropicaux sont observés, le Pacifique Est est le seul où l'activité cyclonique présente une tendance significative à la baisse au cours des $\sim$ 25 dernières années (Kossin et al., 2007). Est-ce que les diverses simulations du MRCC5 effectuées ici arrivent à reproduire cette baisse d'activité ? Si oui, est-ce que le l'on peut utiliser le MRCC5 pour tenter de comprendre pourquoi le Pacifique Est est le seul endroit où cela est observé ? Aussi, le nombre de cyclones dans le Pacific Est tend à anti-corréler avec celui de l'Atlantique (Wang ; 2010).

Est-ce que cette anti-correlation est présente dans les simulations du MRCC5 ? On pourrait aussi évaluer, comme nous l'avons fait pour l'Atlantique, l'impact d'un changement de résolution sur les cyclones tropicaux en comparant les simulations à haute résolution avec les simulations à plus basse résolution (1°et 2°) et ainsi vérifier si la résolution joue un rôle aussi important dans la simulation des cyclones dans le Pacifique Est que dans l'Atlantique. Puisque plusieurs cyclones du Pacifique Est doivent leur origine dans l'interaction entre les ondes africaines de l'Est et la cordillère américaine (Zehnder et al., 1998), il serait aussi intéressant d'étudier l'impact sur la cyclogénèse de simuler les ondes d'Est africaines à différentes résolutions et comparer l'effet à celui obtenu sur l'Atlantique. En fait, si les résultats préliminaires sont encourageants, on pourrait même pousser davantage l'étude de ces interactions à l'aide de quelques simulations additionnelles où l'on garderait le même domaine et la même résolution, mais où l'on varierait la hauteur des sommets dans la cordillère américaine. Ceci permettrait de mieux comprendre le rôle de la cordillère américaine dans la formation des cyclones tropicaux dans le Pacifique Est.

De même, plusieurs des simulations effectuées couvrent une grande partie de l'Afrique, soit la totalité de l'Afrique du Nord. Il serait intéressant de voir dans quelle mesure le MRCC5 arrive à reproduire les caractéristiques de la mousson africaine, telle que la quantité de précipitation, date de début et fin de la mousson, les régions affectées, limite nordique, location de la zone de convergence inter-tropicale... De plus, on pourrait évaluer la distribution intra-saisonnière des précipitations et sa relation avec les ondes africaines de l'Est ainsi que la variabilité interannuelle de ces précipitations et évaluer si le MRCC5 arrive à recréer l'impact d'ENSO sur cette variabilité. Finalement, nous avons abordé brièvement l'impact des conditions aux frontières, qui est très important, sur la précipitation simulée au-dessus de la région du Sahel, sans pour autant pousser plus avant l'analyse. Cette question pourrait être abordée ici.

Finalement, une autre suite logique à ce projet serait de développer davantage le programme servant à détecter et suivre les cyclones tropicaux de telle sorte qu'il puisse aussi détecter les tempêtes extra-tropicales. Lors du développement de ce programme, puisque nous nous intéressions seulement aux cyclones tropicaux, un effort particulier a été fait pour choisir des critères spécifiquement afin d'exclure les cyclones extra-tropicaux. Quelques modifications à ce programme permettraient aussi de suivre les cyclones extra-tropicaux. Ceci permettrait non-seulement d'étudier ces systèmes dans le MRCC5, mais

aussi d'étudier la transition entre la phase tropicale et extra-tropicale de la tempête. Ce type d'étude serait d'un intérêt particulier pour les provinces maritimes, qui subissent souvent les contre-coups de ces systèmes durant la saison des ouragans.

BIBLIOGRAPHIE

(1) Adler, R.F., G.J. Huffman, A. Chang, R. Ferraro, P. Xie, J. Janowiak, B. Rudolf, U. Schneider, S. Curtis, D. Bolvin, A. Gruber, J. Susskind, P. Arkin and E. Nelkin (2003) : The Version 2 Global Precipitation Climatology Project (GPCP) Monthly Precipitation Analysis (1979-Present). *J. Hydrometeor.*, 4,1147-1167.

(2) Adler, R.F., G.J. Huffman, D.T. Bolvin, S. Curtis and E.J. Nelkin (2000) : Tropical Rainfall Distributions Determined Using TRMM Combined with Other Satellite and Raingauge Information. *J. Appl. Meteor.* 39, 2007-2023.

(3) Aiyyer A. R. and C. Thorncroft (2006) : Climatology of vertical wind shear over the tropical Atlantic. *J. Clim.*, 19, 2969-2983.

(4) Andersson, E., P. Bauer, A. Beljaars, F. Chevallier, E. Hólm and coauthors (2005) : Assimilation and modeling of the atmospheric hydrological cycle in the ECMWF forecasting system. *Bull. Amer. Meteor. Soc.*, 86, 387-402.

(5) Ashok, K., S. K. Behera, S. A. Rao, H. Weng and T. Yamagata (2007) : El Niño Modoki and its possible teleconnection. *J. Geophys. Res.*, 112, C11007, doi :10.1029/2006JC003798.

(6) Avila L.A. and R.J. Pasch (1995) : Atlantic Tropical Systems of 1993. *Mon. Wea. Rev.*, 123, 887-896.

(7) Bélair, S., J. Mailhot, C. Girard and P. Vaillancourt (2005) : Boundary layer and shallow cumulus clouds in a medium-range forecast of a large-scale weather system. *Mon. Wea. Rev.*, 133, 1938-1959.

(8) Bélair, S., L.-P. Crevier, J. Mailhot, B. Bilodeau, and Y. Delage (2003) : Operational implementation of the ISBA land surface scheme in the Canadian regional weather forecast model. Part I : Warm season results. *J. Hydromet.*, 4, 352-370.

(9) Bélair, S., J. Mailhot, J. W. Strapp, and J. I. MacPherson (1999) : An examination of local versus nonlocal aspects of a TKE-based boundary layer scheme in clear convective conditions, *J. Appl. Meteor.*, 38, 1499-1518.

(10) Bender, M. A., I. Ginis, R. Tuleya, B. Thomas and T. Marchok (2007) : The operational GFDL coupled hurricane-ocean prediction system and a summary of its performance. *Mon. Wea. Rev.*, 135, 3965-3989.

(11) Bengtsson, L., K. I. Hodges, M. Esch, N. Keenlyside, L. Kornblueh, J. Luo and T. Ymagata (2007b) : How may Tropical Cyclones Change in a Warmer Climate ? *Tellus*, 59A, 539-561. doi : 10.1111/j.1600-0870.2007.00251.x.

(12) Bengtsson, L., K. I. Hodges and M. Esch (2007a) : Hurricane-type vorticies in a T159 resolution global model : Comparisons with observations and reanalyses, *Tellus*, 59A, 396-416. doi : 10.1111/j.1600-0870.2007.00236.x.

(13) Bengtsson, L., S. Hagemann and K. I. Hodges (2004) : Can Climate Trends be Calculated from reanalysis Data, *MPI Report 351.*

(14) Bengtsson L., M. Botzet, M. Esch (1996) : Will greenhouse gas-induced warming over the next 50 years lead to a higher frequency and greater intensity of hurricanes ? *Tellus*, 48A, 57-73.

(15) Bindoff, N.L., J. Willebrand, V. Artale, A. Cazenave, J. Gregory, S. Gulev, K. Hanawa, C. Le Quéré, S. Levitus, Y. Nojiri, C.K. Shum, L.D. Talley and A. Unnikrishnan (2007) : Observations : Oceanic Climate Change and Sea Level. In : Climate Change 2007 : The Physical Science Basis. Contribution of Working Group I to the Fourth Assessment Report of the Intergovernmental Panel on Climate Change [Solomon, S., D. Qin, M. Manning, Z. Chen, M. Marquis, K.B. Averyt, M. Tignor and H.L. Miller (eds.)].*Cambridge University Press*, Cambridge, United Kingdom and New York, NY, USA.

(16) Bister, M., and K. A. Emanuel (1998) : Dissipative heating and hurricane intensity. *Meteor. Atmos. Phys.*, 52, 233240.

(17) Blake, E.S., E.N. Rappaport, J.D. Jarrell, and C. W. Landsea (2005) : The Deadliest, Costliest, and Most Intense United States Tropical Cyclones from 1851 to 2004 (and Other Frequently Requested Hurricane Facts). NOAA Technical Memorandum NWS TPC-4.

(18) Bougeault, P. and P. Lacarrère (1989) : Parameterization of orography-induced turbulence in a mesobeta-scale model, *Mon. Wea. Rev.*, 117, 1872-1890.

(19) Camargo S. and S. Zebiak (2002) : Improving the detection and tracking of tropical cyclones in atmospheric general circulation models. *Weather Forecast*, 17, 1152-1162.

(20) Camargo, S. J., A. G. Barnston, and S. E. Zebiak (2005) : A statistical assessment of tropical cyclone activity in atmospheric general circulation models. *Tellus*, 57A, 589-604.

(21) Camargo, S. J., A. H. Sobel, A. G. Barnston, and K. A. Emanuel (2007a) : Tropical cyclone genesis potential index in climate models, *Tellus*, 59A, 428-443. doi :10.1111/j.1600-0870.2007.00238.x.

(22) Camargo, S. J., K. A. Emanuel, and A. H. Sobel (2007b) : Use of a genesis

potential index to diagnose ENSO effects on tropical cyclone genesis. *J. Clim.*, 20, 4819-4834.

(23) Camargo, S. J., M. C. Wheeler and A. H. Sobel (2009) : Diagnosis of the MJO modulation of tropical cyclogenesis using an empirical index. *J. Atmos. Sc.*, 66, 3061-3074, doi : 10.1175/2009JAS3101.1.

(24) Caron, L.-P., C.G. Jones and K. Winger (2010) : Impact of resolution and downscaling technique in simulating recent Atlantic tropical cyclone activity. *Clim. Dyn.*, DOI 10.1007/s00382-010-0846-7.

(25) Caron, L.-P., and C. G. Jones (2008) : Analysing present, past and future tropical cyclone activity as inferred from an ensemble of Coupled Global Climate Models. *Tellus*, 60A, 80-96.

(26) Casey, K. and P. Cornillon (2001) : Global and Regional Sea Surface Temperature Trends, *J. Clim.*, 14, 3801-3818.

(27) Chauvin, F., J.-F. Royer and M. Déqué (2006) : Response of hurricane-type vortices to global warming as simulated by ARPEGE-Climat at high resolution. *Clim. Dyn.*, 27, 377-399.

(28) Chauvin, F., J.F. Royer and H. Douville (2005) : Interannual variability and predictability of African easterly waves in a GCM. *Clim. Dyn.*, 24, 523-544.

(29) Christensen, J.H., B. Hewitson, A. Busuioc, A. Chen, X. Gao, I. Held, R. Jones, R.K. Kolli, W.-T. Kwon, R. Laprise, V. Magaa Rueda, L. Mearns, C.G. Menndez, J. Risnen, A. Rinke, A. Sarr and P. Whetton (2007) : Regional Climate Projections. In : Climate Change 2007 : The Physical Science Basis. Contribution of Working Group I to the Fourth Assessment Report of the Intergovernmental Panel on Climate Change [Solomon, S., D. Qin, M. Manning, Z. Chen, M. Marquis, K.B. Averyt, M. Tignor and H.L. Miller (eds.)]. *Cambridge University Press*, Cambridge, United Kingdom and New York, NY, USA.

(30) Côté J., S. Gravel, A. Methot, A. Patoine, M. Roch and A. Staniforth (1998) : The operational CMC/MRB Global Environmental Multiscale (GEM) model : Part I - Design considerations and formulation. *Mon. Wea. Rev.*, 126, 1373-1395.

(31) Courtier, P., and J.-F. Geleyn (1988) : A global numerical weather prediction model with variable resolution : Application to the shallow-water equations. *Quart. J. Roy. Meteor. Soc.*, 114, 1321-1346.

(32) Davies, H.C. (1976) : A lateral boundary formulation for multi-level prediction models. *Quart. J. Roy. Meteor. Soc.*, 93, 1-17.

(33) Delworth, T.L., A.J. Brocoli, A. Rosati, R.J. Stouffer, V. Balaji, J.A. Beesley, W.F. Cooke, K.W. Dixon, J. Dunne, K.A. Dunne, J.W. Durachta, K.L. Findell, P. Ginoux, A. Gnanadesikan, C.T. Gordon, S.M. Griffies, R. Gudgel, M.J.

Harrison, I.M. Held, R.S. Hemler, L.W. Horowitz, S.A. Klein, T.R. Knutson, P.J. Kushner, A.R. Langenhorst, H.C. Lee, S.J. Lin, J. Lu, S.L. Malyshev, P.C.D. Milly, V. Ramaswamy, J. Russel, M.D. Schwarzkopf, E. Shevliakova, J.J. Sirutis, M.J. Spelman, W.F. Stern, M. Winton, A.T. Wittenberg, B. Wyman, F. Zeng and R. Zhang (2006) : GFDL's CM2 global coupled climate models - Part 1 : Formulation and Simulation characteristics, *J. Clim.*, 9, 643-674.

(34) Diedhiou, A., S. Janicot, A. Viltard and P. de Felice (2002) : Energetics of easterly wave disturbances over West Africa and the tropical Atlantic : a climatology from the 1979-95 NCEP/NCAR reanalyses. *Clim. Dyn.*, 18, 487-500.

(35) Diedhiou, A., S. Janicot, A. Viltard, P. de Felice and H. Laurent (1999) : Easterly wave regimes and associated convection over West Africa and tropical Atlantic : results from the NCEP/NCAR and ECMWF reanalyses. *Clim. Dyn.*, 15, 795-822.

(36) Elsner, J. B., J. P. Kossin, and T. H. Jagger (2008) : The increasing intensity of the strongest tropical cyclones. *Nature*, 455, 92-95.

(37) Emanuel, K. A. (2005) : Increasing destructiveness of tropical cyclones over the past 30 years. *Nature*, 326, 686-688.

(38) Emanuel, K. A. and D. Nolan (2004) : Tropical Cyclone Activity and Global Climate, in 26th Conference on Hurricanes and Tropical Meteorology, pp.240-241, *Amer. Meteor. Soc.*, Miami, FL.

(39) Emanuel, K. A. (1995) : Sensitivity of tropical cyclones to surface exchange coefficients and a revised steady-state model incorporating eye dynamics. *J. Atmos. Sci.*, 52, 39693976.

(40) Evan, A. T., D. J. Vimont, A. K. Heiginger, J. P. Kossin, and R. Bennartz (2009) : The role of aerosols in the evolution of tropical North Atlantic Ocean temperature anomalies, *Science*, DOI : 10.1126/science.1167404.

(41) Fink, A.H., J.M. Schrage and S. Kotthaus (2010) : On the potential causes of the non-stationary correlations between West African precipitation and Atlantic hurricane activity. *J. Clim.*, 23, 54375456.

(42) Flato, G.M. (2005) : The thrid generationcoupled global climate model (CGCM3), www.cccma.ba.ca/modelscgcm2.shtml.

(43) French, J. R., W. M. Drennan, J. A. Zhang and P. G. Black (2007) : Turbulent fluxes in the hurricane boundary layer. Part I : momentum flux. *J. Atmos. Sci.*, 64, 1089-1102.

(44) Fox-Rabinovitz M. S., L. L. Takacs and R. C. Govindaraju and M. J. Suarez (2001) : A variable-resolution stretched-grid general circulation model : regional climate simulation, *Mon. Wea. Rev.*, 129, 453-469.

(45) Furevik, T., M. Bentsen, H. Drange, N. Kvamsto and A. Sorteberg (2003) : Description and evaluation of the Bergen climate model : ARPEGE coupled with MICOM. *Clim. Dyn.*, 21 27-51.

(46) Gleckler, P. (1996) : Atmospheric Model Intercomparison Project Newsletter. No. 8, PCMDI/LLNL. [Available online at http ://www-pcmdi.llnl.gov/projects/amip/NEWS].

(47) Goldenberg, S. B., C. W. Landsea, A. M. Mestas-Nuez and W. M. Gray (2001) : The recent increase in Atlantic hurricane activity : causes and implications. *Science*, 293, 474-479.

(48) Goldenberg, S.B., and L.J. Shapiro (1996) : Physical mechanism for the association of El Niño and West African rainfall with Atlantic major hurricane activity. *J. Clim.*, 9, 1169-1187.

(49) Gordon, H.B. Rotstayn, J.L. McGregor, M.R. Dix and E. A. Kowalczyk (2002) : The CSIRO mk3 climate system model. Tech. Rep. 60, CSIRO Atmospheric Research, Aspendale.

(50) Gray, W. (1994) : Early August updated forecast of Atlantic seasonal hurricane activity for 1994. 24 pp. [Available from Department of Atmospheric Science, Colorado State University, Fort Collins, CO 80523]

(51) Gray, W. M., C. W. Landsea, P. W. Mielke Jr., and K. J. Berry (1993) : Predicting Atlantic Basin Seasonal Tropical Cyclone Activity by 1 August. *Wea. Forecasting*, 8, 73-86.

(52) Gray, W. M. (1984) : Atlantic Seasonal Hurricane Frequency. Part I : El Niño and 30 mb quasi-biennal oscillation influences. *Mon. Wea. Rev.*, 112, 1649-1668.

(53) Gray, W. M. (1975) : Tropical Cyclone Genesis, Dept. of Atmospheric Science Paper, No. 234, Colorado State University, Fort Collins, CO, p.121.

(54) Gualdi, S., E. Scoccimarro, and A. Navarra (2008) : Changes in tropical cyclone activity due to global warming : results from a high-resolution coupled general circulation model. *J. Clim.*, 21, 5204-5228.

(55) Haarsma R. J., J. F. B. Mitchell and C. A. Senior (1993) : Tropical disturbances in a GCM. *Clim. Dyn.*, 8, 247-257.

(56) Hernández-Díaz, L. (2001) : Conversion dnergie dans une simulation des ondes africaines avec le MRCC. Mmoire de matrise en sciences de l'atmosphre. Dpartement des sciences de la terre et de latmosphre, UQAM. 64 pp.

(57) Holland, G. J. (1993) : Ready Reckoner - Chapter 9, Global Guide to Tropical Cyclone Forecasting, WMO/TC-No. 560, Report No. TCP-31, World Meteorological Organization, Geneva.

(58) Hsieh, J.S., and K.H. Cook (2005) : Generation of African Easterly Wave Disturbances : Relationship to the African Easterly Jet. *Mon Wea Rev.* 133, 1311-1327.

(59) Johns, T. C. Durman, H. Banks, M. Roberts, A. McLaren, J. Ridley, C. Senior, K. Williams, A. Jones, A. Keen, G. Rickard, S. Cusack, M. Joshi, M.Ringer, B. Dong, H. Spencer, R. Hill, J. Gregory, A. Pardaens, J. Lowe, A. Bodas-Salcedo, S. Stark and Y. Searl (2004) : HadGEM1 - model description and analysis of preliminary experiments for the IPCC Fourth Assesment Report, Tech. Rep. 55, U.K. Met Office, Exeter, U.K.

(60) Jungclaus, J. H., N. Keenlyside, M. Botzet, H. Haak, J.-J. Luo, M. Latif, J. Marotzke, U. Mikolajewicz and E. Roeckner (2006) : Ocean Circulation and Tropical Variability in the coupled model ECHAM5/MPI-OM, *J. Clim.*, 19, 3952-3972.

(61) K-1 model developers (2004) : K-1 couple model (MIROC) description Tech. Rep. 1, Center for Climate System Research, University of Tokyo.

(62) Kain, J. S., and J. M. Fritsch (1990) : A one-dimensional entraining/detraining plume model and application in convective parameterization. *J. Atmos. Sci.*, 47, 2784-2802.

(63) Kim, H.-M., P. J. Webster and J. A. Curry (2009) : Impact of shifting patterns of Pacific ocean warming on North Atlantic tropical cyclones. *Science*, 325, 77-80.

(64) Klotzbach, P. J. (2006) : Trends in global tropical cyclone activity over the past twenty years. *J. Geophys. Res.*, 33, L10805, doi :10.1029/2006GL025881.

(65) Kossin, J. (2008) : Is the North Atlantic hurricane season getting longer?. *Geophys. Res. Lett.*, 35, L23705, doi :10.1029/2008GL036012.

(66) Kossin, J.P., K. R. Knapp, D. J. Vimont, R. J. Murnane and B. A. Harper (2007) : A globally consistent reanalysis of hurricane variability and trends. *Geophys. Res. Lett.*, 34, L04815. doi :10.1029/2006GL028836.

(67) Knutson, T. R., J. J. Sirutis, S. T. Garner, I. M. Held and R. E. Tuleya (2007) : Simulation of the recent multidecadal increase of Atlantic hurricane activity using an 18-km-grid regional model. *Bull. Am. Meteor. Soc.*, 88, 1549-1565.

(68) Kuo, H. L. (1965) : On formation and intensification of tropical cyclones through latent heat release by cumulus convection. *J. Atmos. Sci.*, 22, 40-63.

(69) Landman, W. A., A. Seth, and S. J. Camargo (2005) : The effect of regional climate model domain choice on the simulation of tropical cyclone-like vortices in the Southwestern Indian ocean. *J. Clim.*, 18, 1263-1274.

(70) Landsea, C.W. (2000) : El Niño-Southern Oscillation and the seasonal

predictability of tropical cyclones. In press in El Niño : Impacts of Multiscale Variability on Natural Ecosystems and Society, edited by H.F. Diaz and V. Markgraf.

(71) Landsea, G., D. Bell, W. M. Gray, and S. B. Goldenberg (1998) : The extremely active 1995 Atlantic hurricane season : Environmental, conditions and verification of seasonal forecasts. *Mon. Wea. Rev.*, 126, 1174 1193.

(72) Landsea, C.W. (1993) : A climatology of intense (or major) Atlantic hurricanes. *Mon. Wea. Rev.*, 121, 1703-1713.

(73) Landsea, C.W. and W.M. Gray (1992) : The strong association between western Sahel monsoon rainfall and intense Atlantic hurricanes. *J. Clim.*, 5, 435 :453.

(74) Landsea, C.W., W.M. Gray, P.W. Mielke and K.J. Berry (1992) : Long-term variations of Western Sahelian monsoon rainfall and intense U.S. landfalling hurricanes. *J. Clim.*, 5, 1528-1534.

(75) Laprise, R. (2008) : Regional climate modelling. *J. Comp. Phys.* (upon invitation), Special issue on « Predicting weather, climate and extreme events », 227, 3641-3666.

(76) Larow, T. E., Y.-K. Lim, D. W. Shin, E. P. Chassignet and S. Cocke (2008) : Atlantic Basin Seasonal Hurricane Simulations. *J. Clim.*, 21, 3191-3206.

(77) Li, J. and H. W. Barker (2005) : A radiation algorithm with correlated-k distribution. Part I : local thermal equilibrium. *J. Atmos. Sci.*, 62, 286-309.

(78) Maloney, E. D. and D. L. Hartmann (2000) : Modulation of hurricane activity in the Gulf of Mexico by the Madden-Julian oscillation. *Science*, 287, 2002-2004.

(79) Manabe, S., J. L. Holloway Jr. and H. M. Stone (1970) : Tropical circulation in a time-integration of a global model of the atmosphere. *J. Atmos. Sci.*, 27, 580-613.

(80) Mann, M., and K. Emanuel (2006) : Atlantic hurricane trends linked to climate change. *EOS*, 87, 233-244.

(81) Marti, O., P. Braconnot, J. Bellier, R. Benshila, S. Bony, P. Brockmann, P. Cadulle, A. Caubel, S. Denvil, J.L. Dufresne, L. Fairhead, M.-A. Filiberti, T. Fichefet, P. Friedlingstein, J.-Y. Grandpeix, F. Hourdin, G. Krinner, C. Lvy, I. Musat and C. Talandier (2005) : The new IPSL Climate System Model : IPSL-CM4 Tech. rep., Institut Pierre Simon Laplace des Sciences de l'Environnement Global, IPSL, Case 101, 4 place Jussieu, Paris, France.

(82) McAdie, C. J. and E. N. Rappaport (1991) : Diagnostic Report of the National Hurricane Center, Vol. 4, No. 1, NOAA, National Hurricane Center, Coral Gables, FL, 45 pp.

(83) McDonald, R. E., D. G. Bleaken, D. R. Cresswell, V. D. Pope, and C. A. Senior (2005) : Tropical storms : Representation and diagnosis in climate models and the impacts of climate change. *Clim. Dyn.*, 25, 19-36.

(84) McFarlane, N. A. (1987) : The effect of orographically excited gravity-wave drag on the circulation of the lower stratosphere and troposphere. *J. Atmos. Sci.*, 44, 1175-1800.

(85) McTaggart-Cowan, R., L. F. Bosart, C. A. Davis, E. H. Atallah, J. R. Gyakum and K. A. Emanuel (2006) : Analysis of Hurricane Catarina (2004). *Mon. Wea. Rev.*, 134, 11, 3029-53.

(86) Meelh, G.A., T.F. Stocker, W.D. Collins, P. Friedlingstein, A.T. Gaye, J.M. Gregory, A. Kitoh, R. Knutti, J.M. Murphy, A. Noda, S.C.B. Raper, I.G. Watterson, A.J. Weaver and Z.-C. Zhao (2007) : Global Climate Projections. In : Climate Change 2007 : The Physical Science Basis. Contribution of Working Group I to the Fourth Assessment Report of the Intergovernmental Panel on Climate Change [Solomon, S., D. Qin, M. Manning, Z. Chen, M. Marquis, K.B. Averyt, M. Tignor and H.L. Miller (eds.)]. *Cambridge University Press*, Cambridge, United Kingdom and New York, NY, USA.

(87) Moon, I.-J., I. Ginis, T. Hara and B. Thomas (2007) : A physic-based parameterization of air-sea momentum flux at high wind speeds and its impact on hurricane intensity predictions. *Mon. Wea. Rev.*, 135, 2869-2878.

(88) Moustaoui, M., J.F. Royer and F. Chauvin (2002) : African easterly wave activity in a variable resolution GCM. *Clim. Dyn.*, 19, 289-301.

(89) Munich Re (2006) : Annual Reviews : Natural catastrophes 2005. Knowledge Series, Topics Geo. (Available online at www.munichre.com).

(90) Murakami, H., and B. Wang (2010) : Future change of North Atlantic tropical cyclone tracks : Projection by a 20-km-mesh global atmospheric model. *J. Clim.*, 23, 2699-2721.

(91) Nakićenović, N., and R. Swart (eds.) (2000) : Special Report on Emissions Scenarios. A Special Report of Working Group III of the Intergovermental Panel on Climate Change. *Cambridge University Press*, Cambridge, United Kingdom and New York, NY, USA, 599 pp.

(92) Norquist, D.C., E.E. Recker and R.J. Reed (1977) : The energetics of African wave disturbances as observed during phase III of GATE. *Mon. Wea. Rev.*, 105, 334-342.

(93) Oouchi, K., J. Yoshimura, H. Yoshimura, R. Mizuta, S. Kusunoki and A. Noda (2006) : Tropical Cyclone Climatology in a Global-Warming Climate as Simulated in a 20 km-Mesh Global Atmospheric Model : Frequency and Wind

Intensity Analyses. *J. Meteorol. Soc. Japan*, 84, 259-276.

(94) Powell, M. D., P. J. Vickery, and T. A. Reinhold (2003) : Reduced drag coefficient for high wind speeds in tropical cyclones. *Nature*, 422, 279-283.

(95) Reed, R.J. (1978) : The structure and behaviour of easterly waves over West Africa and the Atlantic. In Shaw, D.B. , editor, Meteorology over the tropical oceans, *Bracknell : Royal Meteorological Society*, 57-71.

(96) Reed, R. J., D. C. Norquist, and E. E. Recker (1977) : The structure and properties of African easterly wave disturbances as observed during Phase III of GATE. *Mon. Wea. Rev.*, 105, 317-333.

(97) Ross R.S. and T.N. Krisnamurti (2007) : Low-level African easterly wave activity and its relationship to Atlantic tropical cyclogenesis in 2001. *Mon. Wea. Rev.*, 135, 3950-3964.

(98) Royer J.-F., F. Chauvin, B. Timbal, P. Araspin, and D. Grimal (1998) : A GCM study of the impact of greenhouse gas increase on the frequency of occurrence of tropical cyclones. *Clim. Change*, 38, 307-343.

(99) Ryan, B.F., I. G. Watterson and J. L. Evans (1992) : Tropical cyclone frequencies inferred from Gray's Yearly Genesis Parameter : Validation of GCM tropical climates. *Geophys. Res. Lett.*, 19, 1831-1834.

(100) Saunders, M.A., and A.S. Lea (2008) : Large contribution of sea surface warming to recent increase in Atlantic hurricane activity. *Nature*, 451, 557-560.

(101) Schmidt, G. A., R. Ruedy, J.E. Hansen, I. Aleinov, N. Bell, M. Bauer, S. Bauer, B. Cairns, V. Canuto, Y. Cheng, A. Del Genio, G. Faluvegi, A. D. Friend, T. M. Hall, Y. Hu, M. Kelley, N. Y. Kiang, D. Koch, A. A. Lacis, J. Lerner, K. K. Lo, R. L. Miller, L. Nazarenko, V. Oinas, J. Perlwitz, D. Rind, A. Romanou, G. L. Russell, M. Sato, D. T. Shindell, P. H. Stone, S. Sun, N. Tausnev, D. Thresher and M.-S. Yao (2006) : Present Day Atmospheric Simulations using GISS ModelE : Comparison to in-situ, satellite and reanalysis data, *J. Clim.*, 19, 153-192.

(102) Simmons, A. J., and D. M. Burridge (1981) : An energy and angular-momentum conserving finite-difference scheme and hybrid vertical coordinates. *Mon. Wea. Rev.*, 109, 758-766.

(103) Stowasser, M., Y. Wang, and K. Hamilton (2007) : Tropical cyclone changes in the western north Pacific in global warming scenario. *J. Clim.*, 20, 2378-2396.

(104) Sugi, M., A. Noda, and N. Sato (2002) : Influence of global warming on tropical cyclone climatology : an experiment with the JMA global model. *J. Meteorol. Soc. Japan*, 80, 249-272.

(105) Sundqvist, H., E. Berge and J. E. Kristjansson (1989) : Condensation and Cloud Parameterization Studies with a Mesoscale Numerical Weather Prediction Model. *Mon. Wea. Rev.*, 117, 1641-1657.

(106) Thorncroft, C., and K. Hodges (2001) : African Easterly Wave Variability and Its Relationship to Atlantic Tropical Cyclone Activity. *J. Clim.*, 14, 1166-1179.

(107) Trenberth, K.E., and D.J. Shea (2006) : Atlantic hurricanes and natural variability in 2005. *Geophys. Res. Lett.*, 33, L12704, doi :10.1029/2006GL026894.

(108) Trenberth, K.E. (1984) : Signal versus Noise in the Southern Oscillation. *Mon. Wea. Rev.*, 112, 326-332.

(109) Uppala, S. M., P. W. Ilberg, A. J. Simmons, U. Andrae, V. Da Costa Bechtold, and Coauthors (2005) : The ERA-40 reanalysis. *Quart. J. Roy. Meteor. Soc.*, 131, 2961-3012.

(110) van Ulden, A.P., and G.J. van Oldenborgh (2006) : Large-scale Atmospheric Circulation Biases and Changes in Global Climate Model Simulations and their Importance for Climate Change in Central Europe, *Atmos. Chem. Phys.*, 6, 863-881.

(111) Vecchi, G.A., and B. J. Soden (2007) : Increased Tropical Atlantic Wind Shear in Model Projections of Global Warming. *Geophys. Res. Lett.*, 34, L08702, doi :10.1029/2006GL028905.

(112) Walsh, K. J. E., P. Sandery, G. B. Brassington, M. Entel, C. Siegenthaler-LeDrian, J. Kepert, and R. Darbyshire (2009) : Constraints on exchange coefficients in tropical cyclones at extreme wind speeds. *J. Geophys Res. (Oceans)*, 115, C09007. doi :10.1029/2009JC005876.

(113) Walsh, K. J. E., M. Fiorino, C. W. Landsea, and K. L. McInnes (2007) : Objectively Determined Resolution-Dependent Threshold Criteria for the Detection of Tropical Cyclones in Climate Models and Reanalysis. *J. Clim.*, 20, 2307-2314.

(114) Walsh, K. J. E., K.-C. Nguyen and J. L. McGregor (2004) : Fine-resolution regional climate model simulations of the impact of climate change on tropical cyclones near Australia. *Clim. Dyn.*, 22, 47-56.

(115) Walsh K. and I. G. Watterson (1997) : Tropical Cyclone-like Vortices in a Limited Area Model : Comparison with Observed Climatology. *J. Clim.*, 10, 2240-2259.

(116) Wang, C. (2010) : Is Hurricane Activity in One Basin Tied to Another? *EOS*, 91, 93-95.

(117) Washington, W. M., J. W. Weatherly, G. A. Meehl, A. J. Jr. Semtner, T. W.

Bettge, A. P. Craig, W. G. Jr. Strand, J. Arblaster, V. B. Wayland, R. James and Y. Zhand (2004) : Parallel Climate Model (PCM) Control and Transient Simulations. *Clim. Dyn.*, 16, 755-774.

(118) Webster, P. J. (2008) : Myanmar's deadly daffodil. *Nature Geoscience.* doi : 10.1038/ngeo257.

(119) Webster, P. J., G. J. Holland, J. A. Curry, and H.-R. Chang (2005) : Changes in tropical cyclone number and intensity in a warming environment. *Science*, 309, 1844-1846.

(120) Wilson, N.C. (1994) : Surge of Hurricanes and Floods Perturbs Insurance Industry. *J. Meteorol. U.K.*, 19, 3-9.

(121) Wu, M.C., K. H. Yeung and W. L. Chang (2006) : Trends in Western North Pacific Tropical Cyclone Intensity. *EOS*, 87, 537-548.

(122) Yoshimura, J., M. Sugi and A. Noda (2006) : Influence of Greenhouse Warming on Tropical Cyclone Frequency. *J. Meteor. Soc. Japan*, 84, 405-428.

(123) Yukimoto, S. and A. Noda (2002) : Improvements of the Meteorological Research Institute Global Ocean-atmosphere Coupled GCM (MRI-CGCM2) and its climate sensitivity, Tech. Rep. 10, NIES, Japan.

(124) Zadra, A., D. Caya, J. Côté, B. Dugas, C. Jones, R. Laprise, K. Winger and L.-P. Caron (2008) : The next Canadian Regional Climate Model. *Physics in Canada*, 64, 75-83.

(125) Zadra, A., M. Roch, S. Laroche, and M. Charron (2003) : The subgrid scale orographic blocking parameterization of the GEM model. *Atmos.-Ocean*, 41, 155-170.

(126) Zehnder, J. A., D. M. Powell and D. L. Ropp (1998) : The Interaction of Easterly Waves, Orography and the Intertropical Convergence Zone in the Genesis of Eastern Pacific Tropical Cyclones, *Mon. Wea. Rev.*, 127, 1566-1585.

(127) Zhao, M., I. M. Held, S.-J. Lin, and G. A. Vecchi (2009) : Simulations of global hurricane climatology, interannual variability and response to global warming using a 50km resolution GCM. *J. Clim.*, 33, 6653-6678.